Array Signal Processing for Beamforming and Blind Source Separation

by

Iman Moazzen

M.S., Isfahan University of Technology, Isfahan, Iran, 2009

B.S., Science and Research Branch, Islamic Azad University, Tehran, Iran, 2006

A Dissertation Submitted in Partial Fulfillment

of the Requirements for the Degree of

DOCTOR OF PHILOSOPHY

in the Department of Electrical and Computer Engineering

Array Signal Processing for Beamforming and Blind Source Separation

by

Iman Moazzen
M.S., Isfahan University of Technology, Isfahan, Iran, 2009
B.S., Science and Research Branch, Islamic Azad University, Tehran, Iran, 2006

Supervisory Committee

Dr. Panjotis Agathoklis, Supervisor
(Department of Electrical & Computer Engineering)

Dr. Daler Rakhmatov, Member
(Department of Electrical & Computer Engineering)

Dr. Afzal Suleman, Outside Member
(Department of Mechanical Engineering)

Supervisory Committee

Dr. Panjotis Agathoklis, Supervisor
(Department of Electrical & Computer Engineering)

Dr. Daler Rakhmatov, Member
(Department of Electrical & Computer Engineering)

Dr. Afzal Suleman, Outside Member
(Department of Mechanical Engineering)

ABSTRACT

A new broadband beamformer composed of nested arrays (NAs), multi-dimensional (MD) filters, and multirate techniques is proposed for both linear and planar arrays. It is shown that this combination results in frequency-invariant response. For a given number of sensors, the advantage of using NAs is that the effective aperture for low temporal frequencies is larger than in the case of using uniform arrays. This leads to high spatial selectivity for low frequencies. For a given aperture size, the proposed beamformer can be implemented with significantly fewer sensors and less computation than uniform arrays with a slight deterioration in performance. Taking advantage of the Noble identity and polyphase structures, the proposed method can be efficiently implemented. Simulation results demonstrate the good performance of the proposed beamformer in terms of frequency-invariant response and computational requirements.

The broadband beamformer requires a filter bank with a non-compatible set of sampling rates which is challenging to be designed. To address this issue, a filter bank design approach is presented. The approach is based on formulating the design problem as an optimization problem with a performance index which consists of a term depending on perfect reconstruction (PR) and a term depending on the magnitude specifications of the analysis filters. The design objectives are to achieve almost perfect reconstruction (PR) and have the analysis filters satisfying some prescribed frequency specifications. Several design examples are considered to show the satisfactory performance of the proposed method.

A new blind multi-stage space-time equalizer (STE) is proposed which can separate narrowband sources from a mixed signal. Neither the direction of arrival (DOA) nor a training sequence is assumed to be available for the receiver. The beamformer and equalizer are jointly updated to combat both co-channel interference (CCI) and inter-symbol interference (ISI) effectively. Using subarray beamformers, the DOA, possibly time-varying, of the captured signal is estimated and tracked. The estimated DOA is used by the beamformer to provide strong CCI cancellation. In order to alleviate inter-stage error propagation significantly, a mean-square-error sorting algorithm is used which assigns detected sources to different stages according to the reconstruction error at different stages. Further, to speed up the convergence, a simple-yet-efficient DOA estimation algorithm is proposed which can provide good initial DOAs for the multi-stage STE. Simulation results illustrate the good performance of the proposed STE and show that it can effectively deal with changing DOAs and time variant channels.

TABLE OF CONTENTS

LIST OF TABLES

LIST OF FIGURES

LIST OF ABBREVIATIONS

1D	One Dimensional
2D	Two Dimensional
3D	Three Dimensional
AGSC	Adaptive Generalized Sidelobe Canceller
BSS	Blind Source Separation
CC	Computational Complexity
CCI	Co-Channel Interference
CMA	Constant Modulus Property
DFE	Decision Feedback Equalizer
DOA	Direction of Arrival
ESPRIT	Estimation of Signal Parameters via Rotational Invariance Technique
FIR	Finite-duration Impulse Response
FT	Fourier Transform
GSC	Generalized Sidelobe Canceller
ISI	Inter-Symbol Interference
LMS	Least Mean Square
M-D	Multi-Dimensional
MMA	Multi-Modulus Algorithm
MP	Matrix Pencil
MRAF	Magnitude Response of the Analysis Filters
MSE	Mean Square Error
MUSIC	Multiple Signal Classification
NA	Nested Array
PR	Perfect Reconstruction
PW	Plane Wave
ROS	Region of Support
SNR	Signal-to-Noise Ration
STE	Space-Time Equalizer
SVD	singular value decomposition
TF	Trapezoidal Filter
ULA	Uniform Linear Array

ACKNOWLEDGEMENTS

Through my PhD studies at the University of Victoria, I had the greatest privilege to work with kind and outstanding people without whom it would not be possible to finish this thesis.

From the bottom of my heart, I would like to thank my supervisor Prof. Pan Agathoklis for all his technical advice, encouragement, and financial support. I sincerely admire his professional ethics because of his ability to connect with his students on a professional and personal level simultaneously. His office door has been always open for me long and late hours, and sometimes even the weekends. I believe my research style has been strongly influenced by the way that he approaches the problems. Rather than jumping to the solution, he had a remarkable ability to break down a complicated problem into simpler steps which follow a logical line so that I could understand not only how to deal with the problem, but why it was solved that way.

I would like to thank Prof. Peter Wild and Dr. LillAnne Jackson who believed in my teaching and research abilities. Indeed, working for the design office gave me a chance to get an insight into the engineering design and grasp its different aspects. Also, it was such a great pleasure to work as a lab TA along with Mr. Sean McConkey for the design courses.

I am deeply indebted to my students for their constructive feedback which has significantly helped me to improve my teaching style. Undoubtedly, working as a teaching assistant at UVic was an excellent opportunity for me to practice teaching at the university level and increase my genuine desire to become a faculty member.

I would like to express my deepest gratitude to my family for their love and support. Special thanks to my parents who have never deprived me of a chance to be a better person and greatly inspired my motivation for PhD studies. Also, I would like to extend my sincerest thanks and appreciation to my lovely wife Zahra for her unconditional support and patience through my PhD journey.

When it is time to thank good friends, many faces come to my mind. I would like to cordially thank all new and old friends for being very supportive and loyal to me. Million thanks to a very special friend who I considered as a brother, Ali, my office mate for his true friendship.

Last but not least, I am very grateful to UVic staff Mr. Dan Mai, Ms. Janice Closson, Ms. Moneca Bracken, Mr. Kevin Jones, and Mr. Brent Sirna for their kind assistance. Also, funding from Natural Sciences and Engineering Research Council of Canada (NSERC) and University of Victoria is highly appreciated.

Dedicated to my beloved parents and wife

for their unconditional love and support

CHAPTER 1

INTRODUCTION

Electromagnetic and acoustic energy which are constantly received by our eyes and ears give us a lot of information about the events happening around us. Mankind has always been fascinated by approaches to extend its sensory capabilities to listen or see events which are very far. Radar, sonar, and seismic processing are some examples of sensory extension by means of antenna arrays in the modern time [2].

There are two general types of antenna arrays, active and passive. The former means the antenna is used to both transmit the energy and receive its reflection, while the latter is employed just to listen or see the incoming energy. One of the earlier applications of antenna arrays was in radar. Most common radar systems are active such as fire control radars for navy ships, high-resolution navigation, bombing radars, height-finding radars, and air traffic control radars [1]. Another application of antenna arrays is sonar. Active sonar transmits acoustic energy into the water and processes the received echoes. Active sonar and radar are theoretically very similar. The major difference is that the propagation characteristics of acoustic energy in the ocean are more complicated than that of electromagnetic energy through the atmosphere. Besides active sonar, passive one is used to listen to incoming acoustic energy. One of the main applications of such a system is to detect and track submarines [1]. Also, array processing plays an important role in seismology. In this field, some of the interesting areas are the detection and location of underground nuclear explosions, and underground resource exploration. One of the medical applications of antenna array is tomography which forms a cross-sectional image of body by

illuminating it from many different directions and collecting data by a receiving antenna. Moreover, antenna arrays have been used in many communication systems such as satellites and wireless cellular systems. Antenna arrays are also widely used in radio astronomy area. A radio astronomy system is a passive system used to detect the celestial objects and their characteristics. Due to the wideband characteristics of astronomy signals, the radio astronomy systems have very long baselines [1]. One such system, the square kilometer array (SKA[1]) is a recent global project to build the next-generation radio telescope that will have significantly better sensitivity and survey speed than any existing instrument. SKA is aimed to provide answers to fundamental questions about the origin and evolution of the universe.

Processing of the received signal by an antenna array is called array signal processing. Depending on the application, different array geometries can be used in array signal processing as follows:

- Linear or one dimensional (1D) array in which all sensors are aligned on a line
- Planar or two dimensional (2D) array in which all sensors are in one plane.
- Volumetric or three (3D) dimensional array

One of the main research areas of array signal processing, which plays a key role throughout this dissertation, is beamforming which is the reception of energy propagating in a particular direction while rejecting energy propagating in other directions. Our research is mainly focused on beamforming for broadband signals and performing array signal processing for blind source separation. Broadband beamforming is needed when the desired signal is wideband either in

[1] - http://www.skatelescope.org/

nature (such as celestial electromagnetic signals in astronomy systems and audio signals) or the carrier frequency compared to the signal bandwidth is not large (e.g. ultra-wideband technology). On the other hand, blind source separation is applicable to many well-known technologies in wireless communication systems (such as CDMA and TDMA). In the following sections, the related existing work is reviewed.

1.1 Beamforming

In general, beamformer is a spatial-temporal filter which is designed to pass energy from a special direction at some desired frequencies [2]. Taking advantage of antenna array, the received signal can be spatially sampled and processed. Then, a delay line connected to each sensor can be used to perform temporal processing. Depending on the environment or some other possible restrictions, beamforming techniques can be mainly categorized into two classes: adaptive and fixed [3]. Adaptive beamformers are common when the environment is changing fast, and the beamformer needs to be updated from time to time to adapt to the current situation. On the other hand, when the environment is not time-varying or changes very slowly, there is no need to update weights frequently. In such a case, fixed beamformers can be employed.

For narrowband signals, since no temporal filtering is involved, beamformer can be interpreted as a spatial filter. In this case, beamforming can be achieved by an instantaneous linear combination of the received array signals as shown in Figure 1.1. Delay-and-sum is one of the simplest approaches for narrowband beamforming [1]. In order to provide a trade-off between good selectivity (the ability to resolve two signals coming from different directions) and strong interference cancellation (eliminating undesired signals), different weighting approaches

such as cosine, raised cosine, Han, Blackman, Hamming, and Prolate have been proposed [1]. Linearly constrained minimum variance (LCMV) beamformer [4] and its efficient implementation known as generalized sidelobe canceller (GSC) [6] are other two well-known beamforming approaches which are applicable to both narrowband and wideband signals and are explained in Section 1.1.1. A comprehensive review of narrowband beamforming techniques can be found in [1].

A straightforward approach that enables us to use narrowband techniques in wideband beamforming is called discrete Fourier transform beamformers [1]. In order to implement such a beamformer, first each sensor needs to be sampled in time. Then FFT needs to be performed to obtain separate frequency bins. Next, the same frequency bins can be fed into a narrowband beamformer to be processed. Finally, by applying inverse Fourier transform the output can be obtained. This method involves a pre-processing step, FFT, and also inverse FFT after beamforming. Besides that, the performance critically depends on the number of frequency bins used (i.e. resolution). More bins result in a better performance at the cost of more computations. Thus, this method is not very efficient when the signal is very wideband.

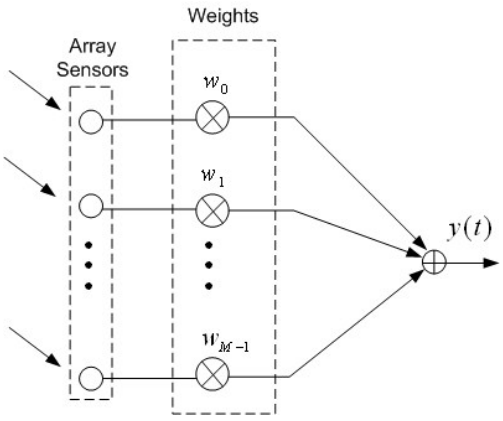

Figure 1.1. A narrowband beamformer

In general, when the involved signals are wideband, an additional temporal processing for the effective operation has to be employed [3], i.e. each individual weight in Fig.1 must be replaced by a delay line. For this case, both adaptive and fixed beamformers can be more classified into fullband and subband [3]. The term 'fullband' indicates that the whole frequency spectrum of the received signal by the antenna is processed by one beamformer. On the contrary, subband beamforming is referred to an approach in which the full spectrum is decomposed into several subbands, and then each subband is processed separately. These broadband beamforming classes are briefly reviewed hereunder.

1.1.1 Fullband Adaptive Broadband Beamformers

It is essential to adjust the beamformer's weights for each new set of signal samples, when the environment is changing fast. Two commonly used adaptive beamformers are the reference signal based beamformer and the LCMV beamformer [4].

In the reference signal based adaptive beamformer, the goal is to adjust coefficients so that the error between the output and the reference signal is minimized. In fact, the problem is a standard adaptive filtering one [5] and can be solved by the well-known techniques such as least mean square (LMS) or recursive least squares (RLS).

In many applications, most likely the reference signal is not available. In this case, if we know the DOA of the signal of interest and their bandwidth, LCMV can be used to minimize the power of the output subject to the constraints imposed to ensure that the beamformer has the required response to the signals arriving from the specified angles and at given frequencies. A

solution to LCMV which is a constrained optimization problem can be provided by the Lagrange multipliers [5]. However, the solution is based on the second order statistics of the array data which may not be available or may change over time. Frost replaced the true second order statistics of data with its simple approximation [4]. An efficient implementation of Frost algorithm is called GSC [6] in which a constrained minimization problem is replaced with an unconstrained one. The imposed constraints can vary from one application to another. Among them, the minimum variance distortionless response (MVDR) beamformer was proposed by Capon [7] in which the constraint is that for a given desired direction, the response of the array is maintained constant.

In the LCMV and its derivations, it was assumed that the desired plane wave (PW) comes from the broadside. Thus, if this assumption is not true, the array needs to be steered either mechanically or electronically by considering the appropriate time delays [3]. Another beamforming approach when the desired signal propagates from the non-broadside direction is to reformulate the constraint matrix by sampling the frequency band of interest of the signal and constrain the response of the beamformer in order to preserve the desired signals at those frequency points [8]. An efficient version of this method is called eigenvector constraint approach [9] which uses singular value decomposition operation to obtain a low rank representation of the constraint matrix. Also, in the classical LCMV-based beamformer, the array response to the desired signals and directions is restricted by the constraints, and final solution must meet them. Although these constraints result in preserving the desired signals, they reduce the degree of freedom to attenuate the interferences. In fact, if some error in the desired output is allowed, the interferences can be rejected more effectively. This approach is called soft

constrained minimum variance beamformer [10] in which the interferences can be suppressed further at the cost of allowing deterioration in the desired output.

LCMV-based techniques can work very effectively when the exact DOA is given. In practice, DOA needs to be estimated in advance. If the estimated DOA deviates a little bit from the actual DOA, their performance will be degraded significantly. In order to make a beamformer robust in this case, several methods have been proposed [11] - [15]. One of the most well-known approaches is spatially extended constraints. The idea is that instead of having constraints for just one angle, we can extend constraints spatially to cover an angle range in which the actual DOA most likely would fall.

1.1.2 Fullband Fixed Broadband Beamformers

Fixed beamformers can be employed when the DOAs of all PWs are not changing, and there is no need to update weights frequently. Several fixed broadband beamformers have been proposed. When the desired beampattern is given, the weights can be found using any well-known iterative optimization method such as a weighted Chebyshev approximation problem, or a minmax problem [16]. However, in a case that there are a very large number of coefficients, iterative optimization methods become less efficient and cannot provide a closed form solution to the problem. In this case, analytical approaches like the least squares approach [17] and the eigenfilter approach [18]- [19] can be used. The advantage about the latter is that no matrix inversion is involved which results in less computations.

Another interesting approach to design a fixed wideband beamformer is based on multidimensional filters. The region of support (ROS) of Fourier transform of the far-filed PW is located on the line which can be found using the DOA and desired frequency range [20]. It means when the DOA is given, the location of the line can be obtained. So, the whole idea is to design a filter to pass the desired PW and suppress the interferences. In fact, the filter's passband encloses the ROS of the desired PW as close as possible and ROS of interferences fall inside the stopband area. Based on the array geometry, different filters need to be designed. For instance, when the signal is received by a linear array, the Fourier transform of the spatially and temporally sampled PW is two dimensional (one for the spatial frequency and the other one for the temporal frequency). In this case, a 2D filter such as trapezoidal filter [20] or fan filter [21] can be used. If the linear array is replaced by a planar array, the Fourier transform of the received PW is three dimensional (two for the spatial frequencies and one for the temporal frequency). Thus, a 3D filter such as cone filter [22]- [23] can be used.

Two advantages of using multidimensional filter are as follows: First, it may achieve arbitrary attenuation to suppress interferences which may not be feasible or very complicated by other beamformers. Second, the output does not significantly get distorted due to a small deviation between actual DOA and the estimated one [20]. In fact, the multidimensional filter is not designed just to pass θ_s (desired direction) but a range $[\theta_s - \varepsilon, \theta_s + \varepsilon]$. The parameter ε can be used to control the selectivity.

The problem with the fullband beamformers is that its ability to resolve, i.e. to separate PWs coming from different directions, is decreasing at low frequencies. This means that the

selectivity at low frequencies is not as good as high ones. This problem occurs due to the small aperture, and can be alleviated by increasing the aperture size at the cost of more computations and implementation cost.

To achieve a response which is independent of the frequency, another class of beamformers was proposed which is called frequency-invariant beamformers. Using inverse multidimensional Fourier transform, an approach that is applicable to 1D, 2D, and 3D was proposed by [24] - [26] which is conceptually similar to the filtering method [20] - [23]. It is assumed that the invariant frequency response of the array is given as a function of DOA (not frequency). First, the desired array response needs to be formed with respect to the temporal and spatial frequencies, and then the desired response of antenna, i.e. appropriate weights, can be obtained using inverse Fourier transform. However the array response is almost frequency invariant at high frequencies, it is not behaving well at low frequencies. In fact, when the inverse Fourier transform is applied, if a small number of points in low-frequency is used the resolution around this area would be really poor [3].

One of the interesting approaches for the frequency-invariant class was proposed by Chou [27] which is based on the nested arrays (NAs) and filter-and-sum beamforming. To avoid aliasing in broadband beamforming, the distance between elements (d) must be less than or equal to $\lambda_u / 2$ where λ_u is the wavelength associated with the maximum frequency [1]. Further, the aperture size on the other hand depends on the ratio of the highest to the lowest frequency [1]. For broadband beamforming with a large bandwidth this may lead to a large aperture with a large number of sensors. To achieve the same aperture size and significantly reduce the number

of elements, a potential option is to employ non-uniform arrays such as NAs which are composed of several uniform linear arrays (ULAs) with different apertures and distances between array elements arranged so that some array elements are superimposed. This arrangement corresponds to subsampling in the spatial domain and has been used for wideband beamforming [28]- [32]. Given the number of sensors, an advantage of NAs is that it can achieve longer aperture compared to uniform arrays which results in better performance. Also, when the aperture is given, NAs can be implemented with much less sensors.

1.1.3 Subband Broadband Beamformers

The convergence speed of fullband adaptive beamformers is very slow and the computational complexity is too expensive in a case where a large number of parameters must be updated. For instance, when the received signal is very wideband, a large number of sensors, and accordingly a large number of parameters, should be employed to perform beamforming [1]. In such a case, another group of beamformers called subband adaptive beamformers [33]- [35] can be used in which the received signal would be decomposed into a number of subbands using filter banks. Since the frequency bandwidth of each subband is smaller than that of the original signal, the number of parameters for each subarray would be noticeably reduced which leads to a faster convergence.

The configuration of subband adaptive beamformers is shown in Figure 1.2. First, the signal received at each sensor is split into a number of subbands using analysis filters of the filter bank and then each subband is downsampled. Next, the same subbands of different sensors are fed

into a subband adaptive beamformer. Finally, the beamformers' outputs are upsampled (to recover the original sampling rate) and filtered by synthesis filters of the filter bank to form the final output. For the subband adaptive beamformer part, for example a reference signal adaptive beamformer [36] or GSC [37] can be used.

The concept of subband beamforming can be used in the fixed broadband beamformers. For instance, the frequency invariant approach using inverse multidimensional Fourier transform [24] - [26] mentioned in section 1.1.2 can be easily applied in which the subband adaptive beamformers in Figure 1.2 are replaced by fixed ones [38] and [39].

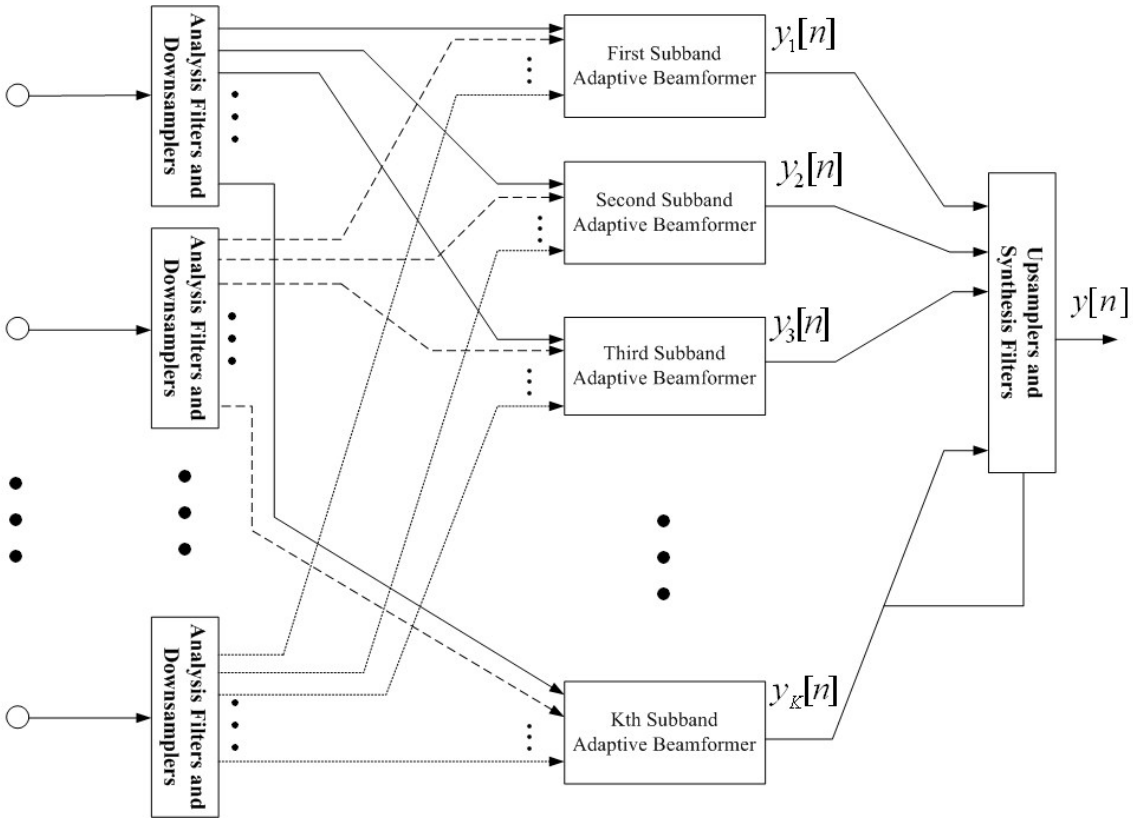

Figure 1.2. A subband adaptive beamformer

1.1.4 Combination of Subband Beamformers and Nested Arrays

In this approach, a special attention will be given to the combination of subsampling in space by NAs and subsampling in time using the filter banks. In [28], a subband adaptive beamformer technique was proposed which uses NAs. This leads to a system which combines subsampling in space and time and uses a GSC as a beamformer. The adaptive beamformer (GSC) was replaced by a fixed beamformer realized using a trapezoidal filter in [31] and [40]. This approach was extended to nested planar arrays [32] in which the incoming PW is sampled by nested rectangular arrays and a frustum filter is used as the beamformer.

One of the important issues in the development of subband beamformers proposed in [28], [31], and [32] is the design of appropriate filter banks. Due to the fact that the associated sampling rates do not form a compatible set, the filter bank design is challenging. To address this issue, a general approach for the filter bank design is presented in Chapter 3. In the next section, a brief review on filter bank design is provided.

1.2 Filter Bank Design

Filter banks, as shown in Figure 1.3, have several applications in communication [41], speech processing [42], image processing and compression [43]- [45], broadband beamforming [3], etc. [46] - [47]. A general picture of filter banks is splitting a fullband signal into many subbands and processing each one individually. In details, the systematic approach is to use analysis filters to decompose the signal into subbands with smaller bandwidth. As a result, the sampling rate can be decreased (downsampling). After processing the subbands (processing stage

is not present in Figure 1.3), in order to reconstruct the output, the original sampling rate must be regenerated (upsampling). Finally, synthesis filters are used to eliminate all replicas of the signal spectrum which appeared due to upsampling. One of the main requirements in filter bank design is perfect reconstruction (PR) which intuitively means that the signal doesn't get corrupted by the filter bank and the output is a delayed version of the input. Generally, filter banks can be categorized into two main groups: uniform filter bank in which all sampling rates, i.e. $\{n_1, n_2, ..., n_K\}$, are equal and non-uniform filter bank in which at least one sampling rate is different from the others.

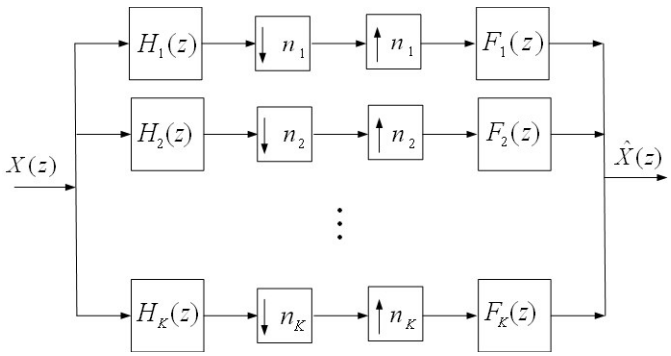

Figure 1.3. A filter bank structure

Many methods have been proposed to design uniform filter banks [48] - [54]. These techniques can be divided into two main groups. In the first group, a prototype is designed and then all filters can be generated from it. An interesting approach in this group is the one proposed by Nguyen in [48] where a prototype filter is designed using constrained optimization. The constraints are derived so that all the significant aliasing terms are cancelled. The analysis and synthesis filters are then obtained as cosine-modulated versions of the prototype filter. The approach in the second group is based on designing all filters at the same time. A powerful method for this was presented by Nayebi et al. [54] where a closed-form relation between the input and output of the filter bank is derived in the time domain. Based on the PR condition, the

necessary and sufficient conditions are derived in the time-domain. Then, to design the filter bank an optimization problem was defined in which the cost function is composed of two terms: the first one is related to the PR conditions and the second one is to achieve the required frequency specifications for the filters. The synthesis and analysis filters are obtained from the results of the optimization.

The theory of non-uniform multirate filter banks was discussed in [55]. It was shown that if the sampling rates satisfy some conditions, the set of sampling rates is called compatible and in this case PR can be achieved. A simple explanation of PR for the compatible set is that all the aliasing components can be paired up and thus can be canceled. If the sampling rates do not form a compatible set, aliasing cannot be totally cancelled at finite cost [55] and thus perfect reconstruction cannot be achieved. Methods to design non-uniform filter banks with compatible sampling sets, can again be divided in two main groups, the prototype-based designs [56] - [57] and the one where all filters are designed concurrently [58]- [59]. One of the methods in the second group was proposed by Nayebi et al. [58] which is an extension to their previous work in [54]. In order to find a closed-form relation between the input and output in the time domain, they introduced sampling operators in the matrix form which mathematically represent downsampling and upsampling blocks. Using these operators, the input-output relation can be derived which can be used to formulate the PR condition. Then, similarly to [54], optimization was used to design the filter bank. Another method was proposed by Ho et al. [59] in which the objective is to minimize the sum of the ripple energy for all the individual filters, subject to the specifications on PR error (distortion and aliasing) and filters' frequency specifications. The design problem was formulated as a quadratic semi-infinite programming problem, and

minimized by a dual parameterization algorithm. Since the problem is convex, the solution (if it exists) is unique and a global minimum. As was discussed in [59], a unique solution exists if the sampling set is compatible and the length of all filters is sufficiently long. Taking advantage of constraint optimization techniques, Ho et al. proposed an efficient algorithm for solving this semi-infinite programming which makes the design much faster [60].

The design of filter banks with non-compatible sampling sets is complicated by the fact that PR cannot be achieved. A possible objective is to achieve almost PR while the analysis and synthesis filter specifications are satisfied. To deal with filter banks with non-compatible sampling sets, Nayebi et al. extended the method of [58] (which does not give satisfactory results in this case) by replacing each filter by several filters in [61]. This provides more degrees of freedom to achieve almost PR. Another approach for achieving almost PR for non-compatible sampling sets was proposed by Chen et al. [62] using linear dual rate systems. In [63], linear dual rate systems were implemented using LTI filters, conventional samplers, and block samplers. In both [62] and [63], the filter banks were assumed to be maximally decimated.

1.3 Blind Source Separation

Source signal separation is one the fundamental issues in communication systems in which a set of source signals have been mixed together and the objective is to recover the original signals using array signal processing. This mixture mainly happens due to either co-channel interference (CCI) or inter-symbol interference (ISI). CCI is caused by simultaneously serving several users which transmit data at the same frequency, and ISI is caused either by the inherent frequency-selective characteristic of the communication channels or multipath propagation [64]. The first

type of ISI is known as temporal ISI resulting in successive symbols to blur together, and the second is called spatial ISI in which several delayed versions of the same data are received by the antenna with different direction of arrivals (DOAs) as a result of reflections from different objects. In order to separate all users from a set of mixed signals received by the antenna and recover the data transmitted by each user, CCI and ISI have to be cancelled.

One of the techniques to combat CCI is using antenna arrays and beamforming [1]. As mentioned in Section 1.1, if a pilot signal is available, the beamformer's weights can be adjusted so that the error between the output and the reference signal is minimized. Another approach for combating CCI using antenna arrays consists of two main stages: separating different users based on their locations using DOA estimation techniques, and then designing a beamformer to pass the desired signal propagating from the user of interest while rejecting signals from all others with different DOAs. Some of the best-known techniques for DOA estimation are multiple signal classification (MUSIC) [65] and estimation of signal parameters via rotational invariance technique (ESPRIT) [66] and their many variations. These subspace methods entail high computational complexity. In contrast, DOA estimation techniques using matrix pencil (MP) [67] are fast, but the DOA estimation capacity (maximum number of users which can be detected) is less than that of MUSIC and ESPIRIT. The aforementioned methods estimate DOAs without employing training sequences (pilot data). If pilot data is available, it can be used to obtain DOAs for example using the phase difference between subarray beamformers as done in [68]. The performance of this method is very good in terms of accuracy, capacity, and computational complexity at the cost of decreasing the bit rate due to transmitting a training sequence.

After CCI reduction and capturing the desired signal by the beamformer, the last stage in recovering the transmitted data is equalization which reduces ISI. In general, equalizers are trying to track the channel inverse. Linear and decision-feedback equalizers (DFEs) are two common approaches. The former is very simple but not very effective when fading is very deep or the channel is non-minimum phase [64]. In such a case, the latter shows better performance, but it may suffer from error propagation due to feedback of the wrong decision resulting in performance degradation.

Separate CCI and ISI cancellation may not result in satisfactory performance, as was articulated in [69]. Instead a beamformer and an equalizer can be combined into one device called space-time equalizer (STE) to jointly combat CCI and ISI. The optimum STE is the multi-user maximum likelihood sequence estimator (MLSE) [70] which requires the channel information of all users and entails high computational complexity. Several suboptimal hybrid STEs have been proposed in the literature [69], [71] - [73] which function properly provided that either a training sequence [71]-[73] is available or the DOA is known [69].

Blind source separation (BSS) refers to a case where the transmitted signals are recovered without using any information, such as training sequences or DOAs. One of the well-known and the simplest BSS approach is the multi-stage constant modulus algorithm (CMA) [74]- [78]. The constant modulus property [79], which is true for many modulation schemes such as QAM, PSK and FSK, is instrumental in CMA. Thanks to the multi-stage structure, this approach is able to capture multiple cochannel sources and provide estimates of their DOAs. Each stage consists of a weight-and-sum CMA-based adaptive beamformer which tries to capture (lock on) one of the

sources, and an adaptive signal canceller which removes the captured source from the array input before processing it by the next stage. The canceller weights can be used to estimate the DOA of the captured source. A blind STE has been recently proposed [80] which functions in two operating modes as proposed in [81] and is based on the multi-modulus algorithm (MMA) [82], an advanced version of CMA. In [80], the DOA is estimated using subarray beamformers [68] which is then used to compute the input for the next stage. As a result of feeding each stage by the previous stage, the inherent problem of multi-stage algorithms, as stated in [83], is inter-stage error propagation leading to performance degradation. Further, in order to achieve strong CCI cancellation it would be beneficial to have deep nulls at the DOAs of the interferers which may not be achieved with an adaptive weight-and-sum beamformer (one set of weights) [1].

1.4 Scope and Contributions of the Dissertation

This dissertation consists of five chapters. Using nested arrays, multidimensional filters, and multirate techniques, an efficient broadband beamformer is presented in Chapter 2. This beamformer needs a special filter bank with a non-compatible sampling set which is challenging to be designed. To address this problem, a general approach for the filter bank design is presented in Chapter 3 which is applicable to both uniform and non-uniform filter banks. In Chapter 4, a multi-stage STE (joint beamforming and equalization) for blind source separation is proposed. Chapter 5 provides concluding remarks and suggestions for the future work.

The major concern of Chapter 2 is to develop an efficient fixed broadband beamformer with (almost) frequency-invariant behavior. In this chapter, first the basic idea of combining nested arrays, multidimensional filters, and multirate techniques is comprehensively explained for a linear array [31]. Then, an extended version of the broadband beamformer proposed in [32] is presented which combines nested hexagonal arrays, hexagonal frustum filters, and multirate techniques. The nested hexagonal arrays used here consist of several hexagonal arrays of increasing size in the x-y plane (each one called subarray) where the distance between elements in each subarray is two times larger than in the previous one. The proposed beamformer consists of subarray beamformers, each one using the signals obtained from one of the nested hexagonal arrays as the input. These signals are filtered and downsampled so that the ROS of the resulting 3D signals in the 3D frequency domain are the same for all subbands. The same hexagonal frustum filter design can therefore be used for all subarray beamformers to pass the desired signal and eliminate interferences. The use of nested arrays leads to larger effective aperture at low temporal frequencies and thus, better selectivity for low frequencies. Further, hexagonal arrays are known to require a lower sensor density for alias free sampling than rectangular arrays. Also, an efficient implementation of this beamformer is presented using Nobel identity [84]. Examples illustrate the good performance of the proposed beamformer with respect to beampattern and computational complexity.

In Chapter 3, a method to design filter banks using optimization is presented. The approach is based on formulating the design problem as an optimization problem with a performance index which consists of a term depending on perfect reconstruction and a term depending on the magnitude specifications for the analysis filters. Perfect reconstruction conditions for finite-

duration impulse response (FIR) analysis and synthesis filters are formulated as a set of linear equations using z-domain analysis. The design objectives are to minimize the perfect reconstruction error and have the analysis filters satisfying some prescribed frequency specifications. The proposed method is applicable to uniform (including critically sampled and over sampled) and non-uniform filter banks (for sampling rates forming a compatible set as well as non-compatible set). Design examples illustrate the performance of the proposed method.

In Chapter 4, a new multi-stage STE has been proposed for BSS. Each stage is equipped with a beamformer, DOA estimator, and an equalizer. An adaptive version of GSC, called adaptive GSC (AGSC) is presented which can adaptively track a user and strongly attenuate other users with different DOAs. The beamformer and equalizer are jointly being updated (STE concept) to combat both CCI and ISI effectively. Using subarray beamformers [68], the DOA, possibly time-varying, of the captured signal is estimated and tracked. The estimated DOA is being used by the AGSC to provide strong CCI cancellation, Further, the estimated DOAs will be used to form the input to the next stages. In order to significantly alleviate inter-stage error propagation, a mean-square-error sorting algorithm is used which assigns detected sources to different stages according to the reconstruction error at different stages. Further, to speed up the convergence, a simple-yet-efficient DOA estimation algorithm is proposed which can provide good initial DOAs for the multi-stage STE. Simulation results illustrate the good performance of the proposed STE and show that it can effectively deal with changing DOAs and time variant channels.

CHAPTER 2

BROADBAND BEAMFORMING USING MULTI-DIMENSIONAL FILERS, NESTED ARRAYS, AND MULTI-RATE TECHNIQUES

2.1 Introduction

Multi-dimensional (M-D) filters can be employed as the beamformers when the DOAs of the desired broadband PWs are known. The approach is based on designing M-D filters whose passband encloses the region of support (ROS) of the desired broadband PW in the frequency domain. All other PWs received by the antenna from a DOA different than that of the desired PW are attenuated. A common property of wideband beamformers is that the ability to resolve two separate PWs coming from different directions (selectivity) is decreasing as the frequency decreases. This is due to the finite aperture, and this drawback can be alleviated by increasing the aperture size. Another approach to tackle this is using nested arrays and multi-rate techniques which is discussed in this chapter.

The chapter is organized as follows: first, in Section 2.2, a broadband signal is defined. Then, in Section 2.3 the mathematical expression for the spectrum of continuous and discrete PWs is reviewed. Also, the concept of ROS is explained which forms the basis of using M-D filters as the beamformers. In Section 2.4, a broadband beamforming approach based on trapezoidal filter (TF) and uniform linear array (ULA) is presented and the effect of finite aperture is illustrated. To alleviate this problem, a broadband beamformer consisting of nested

ULAs, TF, and multirate techniques is proposed in Section 2.5. Examples provided in Section 2.6 demonstrate the good performance of the proposed method in terms of frequency-invariant beampattern and acceptable computational complexity. In Section 2.7, linear antennas are replaced by planar arrays and it is shown that hexagonal arrays can provide more efficient sampling pattern than rectangular arrays. A broadband beamformer based on a hexagonal array and hexagonal FIR frustum filers is presented in Section 2.8 and the effect of finite aperture is reemphasized. The idea presented in Section 2.5 is extended and a new broadband beamformer based on nested hexagonal arrays is proposed in Section 2.9. Finally, the good performance of this beamformer is shown through illustrative examples in Section 2.10.

2.2 Broadband Signals

The relative spread of the temporal bandwidth of a signal is characterized by the bandwidth spread factor signal S_f defined as [20] (See Figure 2.1):

$$S_f = \frac{\mathrm{BW}}{2f_{\max}} \tag{2.1}$$

According to [20], the signal is called broadband if S_f is higher than 0.025.

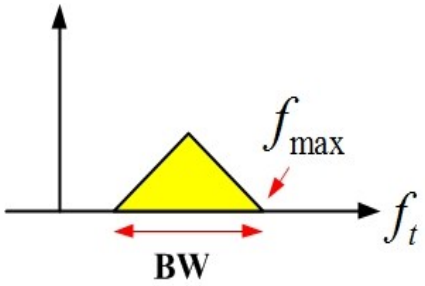

Figure 2.1. Signal representation in the frequency domain

2.3 Spectra of Plane Waves

Energy propagating from a far-filed source can be approximated as a PW over a finite area. Throughout this thesis, the PW approximation for the received signal is adopted. The continuous PW would be spatially and temporally sampled by the array leading to a discrete signal. The mathematical expression for the spectrum of continuous and discrete PWs is provided in the following section.

2.3.1 Continuous Plane Waves

Assume that the received signal is a PW propagating from the direction of $\mathbf{a}$ given by (the minus is because of the direction of $\mathbf{a}$):

$$\mathbf{a} = [-\sin\theta\cos\phi \quad -\sin\theta\sin\phi \quad -\cos\theta]^T \tag{2.2}$$

where θ and ϕ are zenith and azimuth angles in the spherical coordinate system (Figure 2.2). If $f(t)$, the broadband temporal intensity function, is the signal that would be received at the origin of the coordinate system, then the PW received at the position of $\mathbf{p} = [x, y, z]$ is a delayed version of $f(t)$, namely $f(t-\tau_P)$ where $\tau_P = \mathbf{a}^T\mathbf{p}/c$, and c is the velocity of propagation in the medium [1]. From Eq.(2.2), we can get:

$$f(t-\tau_p) = f(t + c^{-1}(\sin\theta\cos\varphi\, x + \sin\theta\sin\varphi\, y + \cos\theta\, z)) \tag{2.3}$$

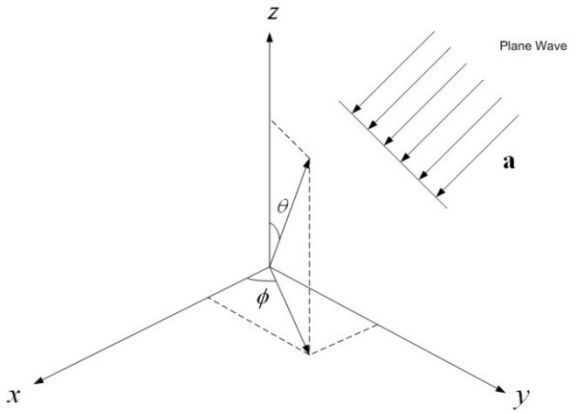

Figure 2.2. The plane wave propagating from a special direction

Let's assume the continuous PW will be received by 1D 'continuous' aperture located on the z-axis. Since $x = y = 0$, from Eq.(2.3):

$$f(t-\tau_p) = f(t + c^{-1}\cos\theta\, z) \tag{2.4}$$

The 2D continuous-domain Fourier transform of this signal is [20]:

$$\begin{aligned}\mathbf{F}(f_z, f_{ct}) &= \int_{ct=-\infty}^{\infty}\int_{z=-\infty}^{\infty} f(t + c^{-1}\cos(\theta)z)e^{-j2\pi f_z z}\, e^{-j2\pi f_{ct}(ct)}\, dz\, d(ct) \\ &= c\delta(f_z - \cos(\theta)f_{ct})F(cf_{ct})\end{aligned} \tag{2.5}$$

where δ is a 1D unit impulse function, f_{ct} is equal to $c^{-1}f_t$ (f_t and f_z represent the temporal and spatial frequency, respectively), and $F(cf_{ct})$ is 1D continuous-domain Fourier transform of $f(t)$. From Eq.(2.5), it can be seen that the ROS of $\mathbf{F}(f_z, f_{ct})$ is on the line $f_x - \cos(\theta)f_{ct} = 0$

which passes through the origin and makes an angle equal to $\Phi = \tan^{-1}(\cos\theta)$ with the f_{ct} axis as shown in Figure 2.3. Since $0^o \le \theta \le 180^o$, Φ can be from -45^o to 45^o.

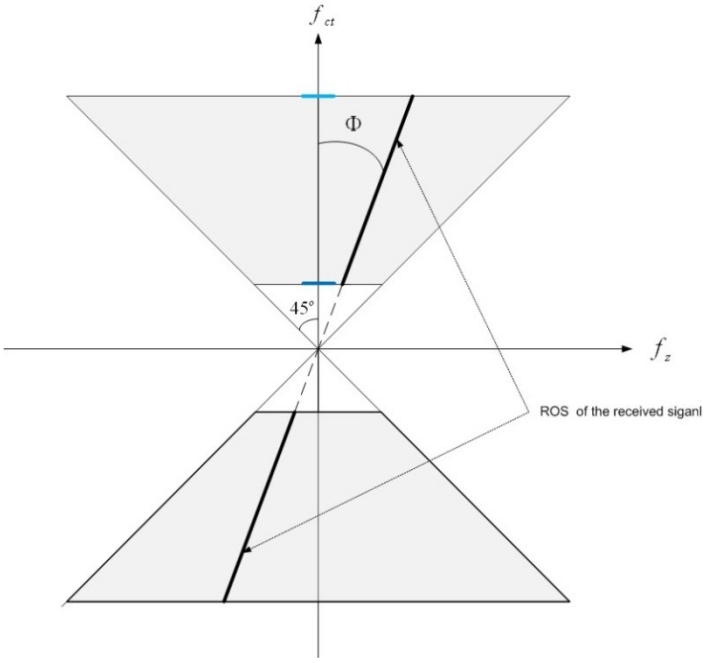

Figure 2.3. The region of support of the PW

2.3.2 Spatially and Temporally Sampled Plane Waves

Consider the continuous aperture is replaced by a ULA as shown in Figure 2.4. A continuous PW, in which $F(f_t)$ is non-zero within the frequency range of $[f_l, f_u]$, is being sampled by this infinite ULA. The spatially sampled signal is further temporally sampled at the rate of $f_s = 1/T_s$. This spatially-temporally sampled signal represented by $f_D(n_t T_s + c^{-1}\cos(\theta) n_z d)$ is a discrete version of $f(t + c^{-1}\cos(\theta) z)$, and its 2D Fourier transform consists of periodically repeated copies of $\mathbf{F}(f_z, f_{ct})$ which is given by:

$$\mathbf{F}_D(e^{j\omega_z}, e^{j\omega_t}) = \sum_{m_t=-\infty}^{\infty} \sum_{m_z=-\infty}^{\infty} \frac{\mathbf{F}(\frac{\omega_z - 2\pi m_z}{2\pi d}, \frac{\omega_t - 2\pi m_t}{2\pi c T_s})}{d(cT_s)} \tag{2.6}$$

where $\omega_z = 2\pi d f_z$ and $\omega_t = 2\pi T_s f_t$ are the normalized frequencies. Inside the Nyquist box, i.e. $|\omega_z| \le \pi$ and $|\omega_t| \le \pi$, $\mathbf{F}_D(e^{j\omega_z}, e^{j\omega_t})$ is equal to the 2D continuous Fourier transform of the PW (scaled by $1/d(cT_s)$) provided no aliasing has happened. In order to avoid aliasing d, distance between elements (Figure 2.4), must be less than $\lambda_u/2$ ($\lambda_u = c/f_u$) [1] and $T_s \le \alpha/2f_{\max}$ ($0 < \alpha \le 1$).

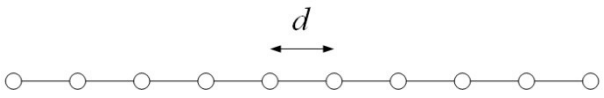

Figure 2.4. Uniform Linear Array

Discussion about Finite Aperture Effect:

In the above analysis it was assumed that the number of sensors on the ULA is infinite which is not realistic. The effect of the finite aperture is that the ROS is no longer a line but a line convolved with a sinc function. Here, the length of ULA is assumed to be $2N_z + 1$. Sampling the PW by such an array can be modeled as multiplying the signal by a finite impulse train which is depicted in Figure 2.5 (left). In the frequency domain, the 2D Fourier transform (FT of the continuous signal would be convolved with the FT of the finite impulse train shown in Figure 2.5 (right). As can be seen, the width of mainlobe shrinks as the array length increases. Although this issue is also present in the time domain due to finite duration of temporal sampling, it is almost

negligible because the number of temporal samples is usually much greater than number of sensors. The finite aperture effect is illustrated in Figure 2.6 where the ULA length is changing from 9 to 65, $\theta = 75^0$ $(\Phi \approx 15^o)$, $f_l = 200$, $f_u = 3200$, $f_s = 8000(\alpha = 0.8)$, and sampling time duration is $512\,T_s$ One can see as the length is increasing the width around the ROS of the incoming PW is decreasing.

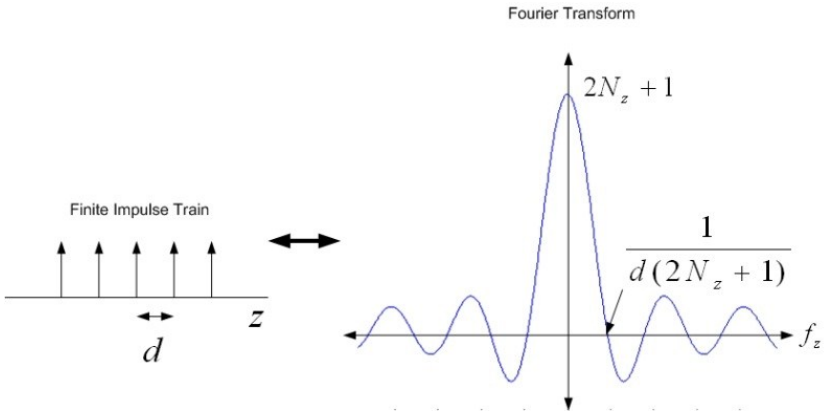

Figure 2.5. Finite Aperture Effect

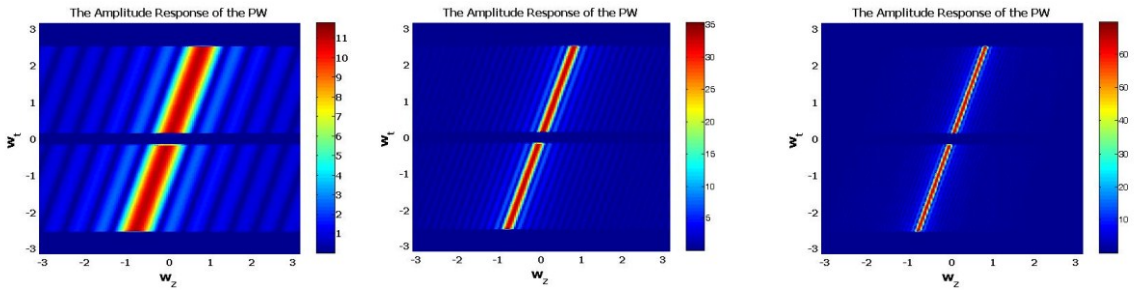

(a) (b) (c)

Figure 2.6. The finite aperture effect when the ULA length is (a) 9, (b) 33, (c) 65

2.4 Wideband Beamforming using Trapezoidal Filters and Uniform Linear Array

As was explained, the ROS of 2D Fourier transform of the PW received by a ULA is located on a line (Figure 2.3). To do beamforming, i.e. passing a PW propagating from a desired direction and reject the others, one can use a 2D FIR TF [20] which is shown in Figure 2.7. In the next section, the TF design is explained, and then the performance of this method is evaluated through an example.

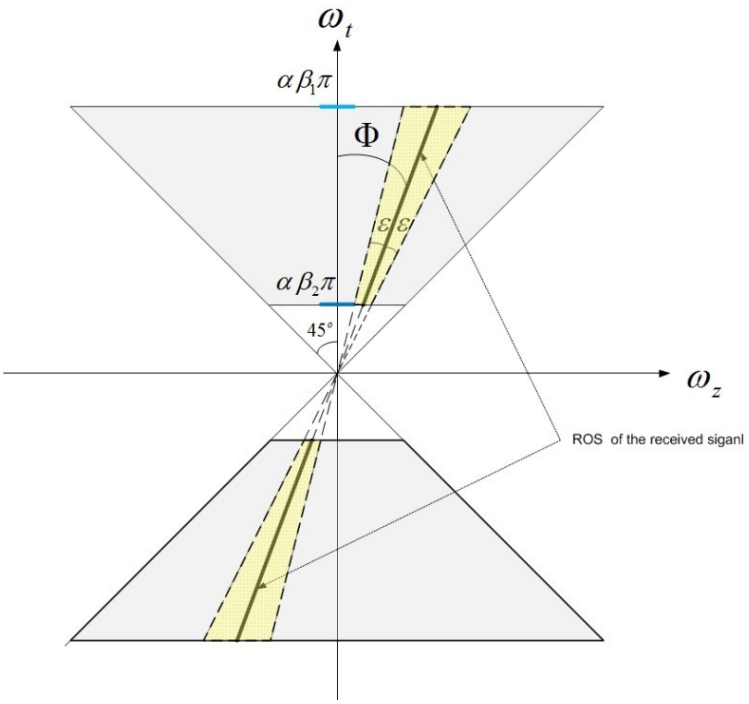

Figure 2.7. The passband area of TF which encloses the ROS of the desired PW as close as possible

2.4.1 Trapezoidal Filter Design

The ideal filter has a gain of unity within the passband area and zero outside. The passband can be defined using the following four parameters; Φ, ε, β_1 and β_2. The first parameter is obtained from the DOA of the desired signal, i.e. $\Phi = \tan^{-1}(\cos\theta)$, and ε controls the selectivity around the DOA. Two coefficients β_1 and β_2, are used to control the upper and lower bounds along ω_t-axis. The passband area in the (ω_z, ω_t) plane can be given by:

$$\begin{aligned} &\omega_z - \alpha^{-1}\tan(\Phi-\varepsilon)\omega_t \geq 0,\ \omega_z - \alpha^{-1}\tan(\Phi+\varepsilon)\omega_t \leq 0 \\ &\omega_t \leq \alpha\beta_1\pi,\ \omega_t \geq -\alpha\beta_1\pi,\ \omega_t \geq \alpha\beta_2\pi,\ \omega_t \leq -\alpha\beta_2\pi \end{aligned} \tag{2.7}$$

Using the inverse Fourier transform, the space-time impulse response of the TF can be obtained. The closed form solution is provided at the Appendix A. Then, the following 2D rectangular window is used to truncate the impulse response:

$$\text{2D window } (n_z, n_t) = \begin{cases} 1 & |n_z| \leq N_z \quad and \quad |n_t| \leq N_{TF} \\ 0 & otherwise \end{cases} \tag{2.8}$$

Example 1 - Design of Trapezoidal Filter

Let's assume the following parameters for the frequency specifications of the TF: $\Phi = 15^o$, $\varepsilon = 5^o$, $\alpha = 0.8$ $\beta_1 = 1, \beta_2 = 0.25$ and $N_z = N_{TF} = 64$ (i.e. the length is 129). The amplitude response of such a TF designed using the described method versus ω_z and ω_t is shown in Figure 2.8 from the top and isometric views.

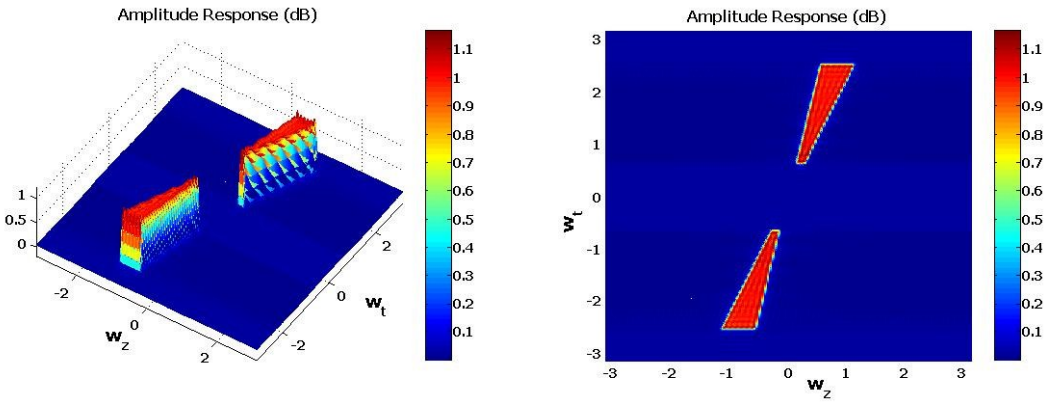

(a) (b)

Figure 2.8. The designed TF from (a) isometric view, (b) top view, $\Phi = 15^o$, $\varepsilon = 5^o$, $\alpha = 0.8$ $\beta_1 = 1, \beta_2 = 0.25$ and $N_z = N_{TF} = 64$

Example 2 - Performance evaluation of beamforming using TF and ULA

Consider an array with 51 sensors which are uniformly spread from $-25d$ to $25d$, and d is equal to $\lambda_u / 2$. Five PWs coming from five different directions were considered. For the sake of graphical illustration, it was assumed that they would be received with different time delays. Their parameters are summarized in Table 2.1. The intensity function for all of them is a sinc whose frequency spectrum is one from 200 to 3200 Hz. The temporal sampling frequency is 6400. The fourth PW was assumed as the desired one, and the rest as the interferences. The amplitude of the 2D Fourier transform of the received signal versus ω_z and ω_t is shown in Figure 2.9. The TF was designed to pass the fourth PW and reject the others. For TF, $N_z = N_{TF} = 25$, $\Phi = 29.83^o$, $\varepsilon = 5^o$, and $\beta_1 = 1, \beta_2 = 1/16$. The amplitude response of TF versus ω_z and ω_t is shown in Figure 2.10 (a-b). The center sensor of TF output is selected as the final output [20] shown in Figure 2.11 (a). Ideally, the output should be a delayed version of the intensity function. The amount of delay is 125 ($N_{TF} = 25$ and the delay for the fourth signal is

100). As can be seen from Figure 2.11 (a), the second and third PWs, which are closer to the desired PW, are attenuated less by TF compared to the first and fifth PW. The reason is that the aperture size of array is not large enough, and accordingly the filter selectivity, i.e. the ability to distinguish two PWs coming from different directions, for low frequency is not as good as for high ones. This drawback is shown in Figure 2.10 (a). In order to tackle this problem, one can increase the length of array and accordingly the spatial order of TF which result in higher cost. Another possible way to alleviate the problem is to decrease ε. However with the given spatial order, as we are decreasing ε the filter quality[1] becomes worse. To illustrate this problem, ε was set to 1^o. The amplitude response of TF and the output are depicted in Figure 2.10 (c-d) and Figure 2.11 (b). In this case, the second and third PWs were attenuated stronger but the desired signal got distorted more because the TF quality is not as good as $\varepsilon = 5^o$ (compare Figure 2.10 (a-b) with Figure 2.10 (c-d)). Thus, it seems that the only way to improve the performance without degrading the desired signal is to increase the aperture size of ULA.

Table 2.1. Five different PWs

	θ	Φ	delay
First PW	120^o	-26.56^o	300
Second PW	45^o	35.26	200
Third PW	65^o	22.90	400
Fourth PW	55^o	29.83	100
Fifth PW	170^o	-44.56	500

[1] - The quality index is defined as the difference between the ideal and obtained filters.

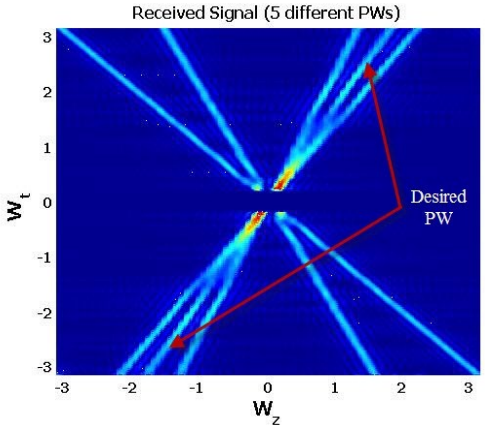

Figure 2.9. The amplitude of the 2D Fourier transform of the signal received by ULA

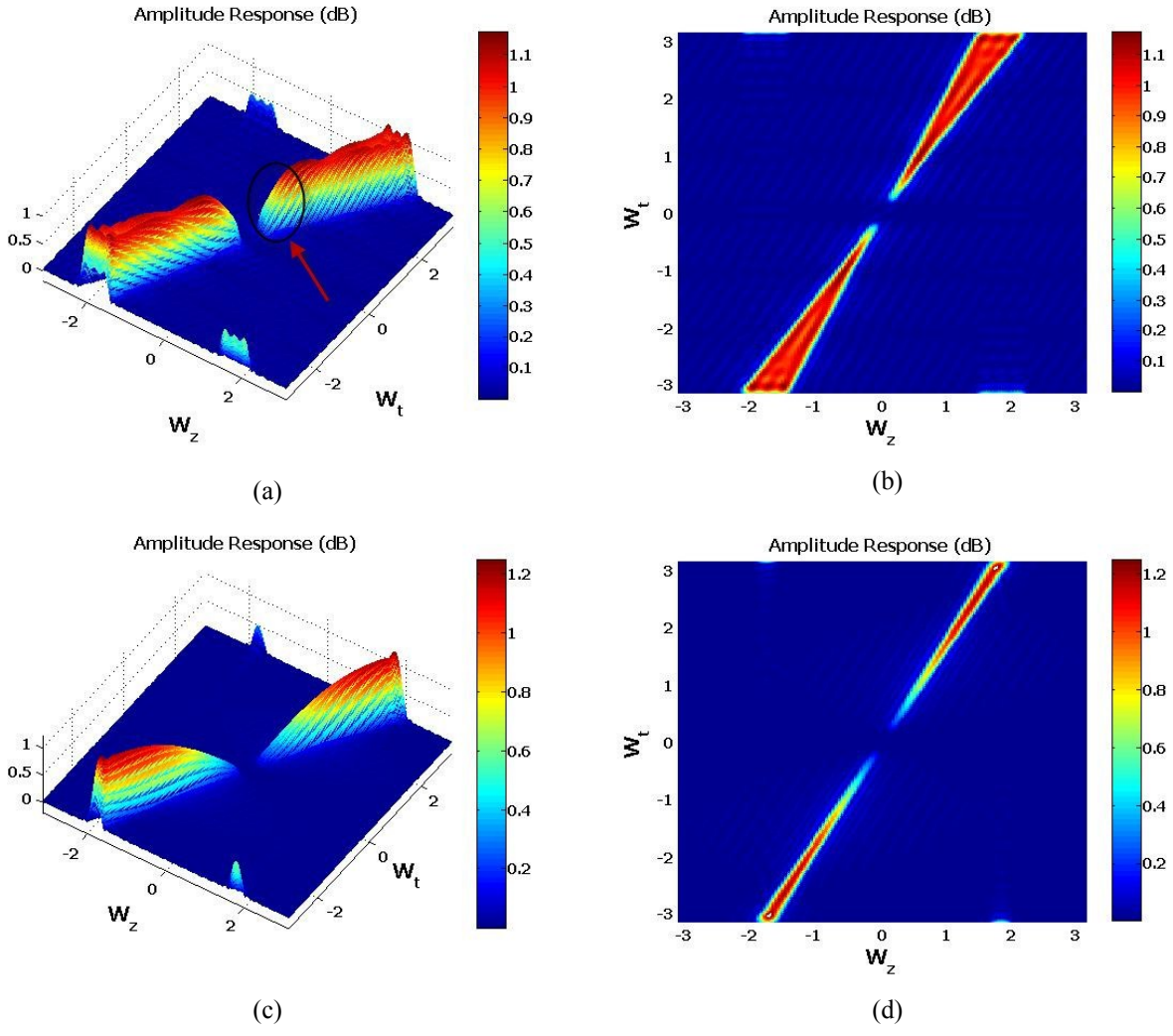

Figure 2.10. The amplitude response of TF (a) $\varepsilon = 5^o$, isometric view, (b) $\varepsilon = 5^o$, top view, (c) $\varepsilon = 1^o$, isometric view, (d) $\varepsilon = 1^o$, top view

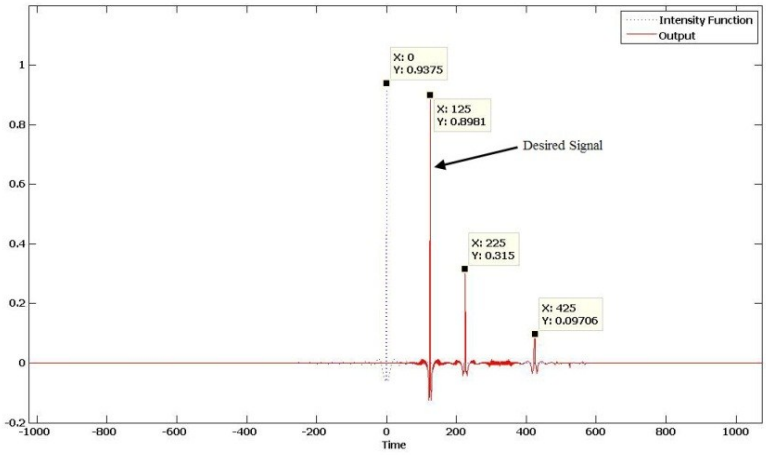

(a)

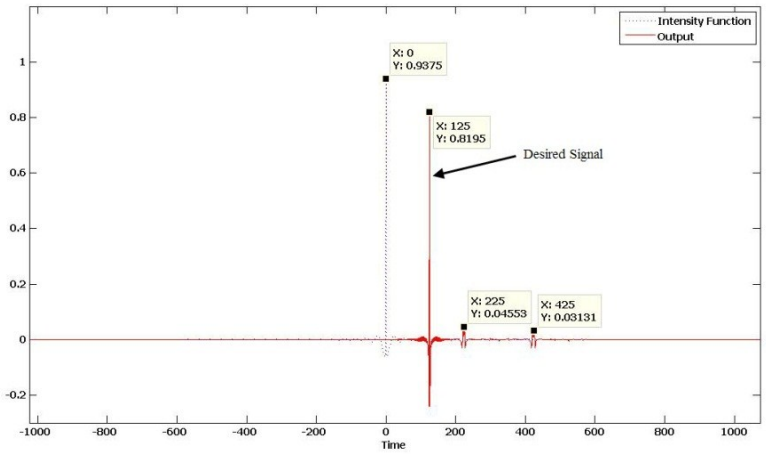

(b)

Figure 2.11. Final output of the beamformer: (a) $\varepsilon = 5^o$, (b) $\varepsilon = 1^o$

In [1], it was shown that to do beamforming properly, the length of antenna should be proportional to the band ratio (f_u / f_l). If the signal is extremely wideband, the required number of sensors for ULA may be prohibitive. To alleviate this problem, ULA can be replaced by NAs. The combination of NAs and subband beamforming using a non-uniform filter bank results in some interesting properties to be described in the next section.

2.5 Broadband Beamforming using 2D Trapezoidal Filters and Nested Uniform Linear Arrays

Consider a broadband PW with temporal bandwidth $[f_l, f_u]$ satisfying the condition that $f_u / f_l = 2^L$. The temporal intensity function $f(t)$ can be recovered using a beamformer consisting of L different subbands as shown in Figure 2.12. The ℓ^{th} subband ($\ell = 1,2,...,L$) consists of a ULA in which the distance between the sensors is equal to $2^{\ell-1}d$. The same number of sensors is used in all subbands. These L nested ULAs have the effect of subsampling the incoming PW in space. The received signal at each array element is temporally sampled by the rate of $f_s = 1/T_s = 2f_u/\alpha$ where $0 < \alpha \le 1$, and then is filtered by an FIR analysis filter $H_\ell(z)$ with the passband within $[f_u/2^\ell, f_u/2^{\ell-1}]$ and a constant group delay N_H for all ℓ. After temporal subsampling, by a factor $2^{\ell-1}$ for the ℓ^{th} subband, the resulting signal is the input to the TF. The following lemma can now be formulated:

Lemma 2.1: The 2D Fourier transform (2D FT) of the input to each TF for $\ell = 1,2,..L$ is given by (See Appendix B):

$$\overline{\mathbf{F}}_D^{\ell}(e^{j\omega_z}, e^{j\omega_t}) = \frac{1}{2^{\ell-1} dT_s}\delta\left(\frac{\omega_z}{2\pi d} - \cos(\theta)\frac{\omega_t}{2\pi c T_s}\right) F\left(\frac{\omega_t}{2\pi T_s 2^{\ell-1}}\right) e^{-\frac{\omega_t}{2^{\ell-1}}N_H} \prod(\omega_t) \tag{2.9}$$

where $\prod(\omega_t)$ is 1 for $\alpha\pi/2 \le |\omega_t| \le \alpha\pi$, and zero elsewhere.

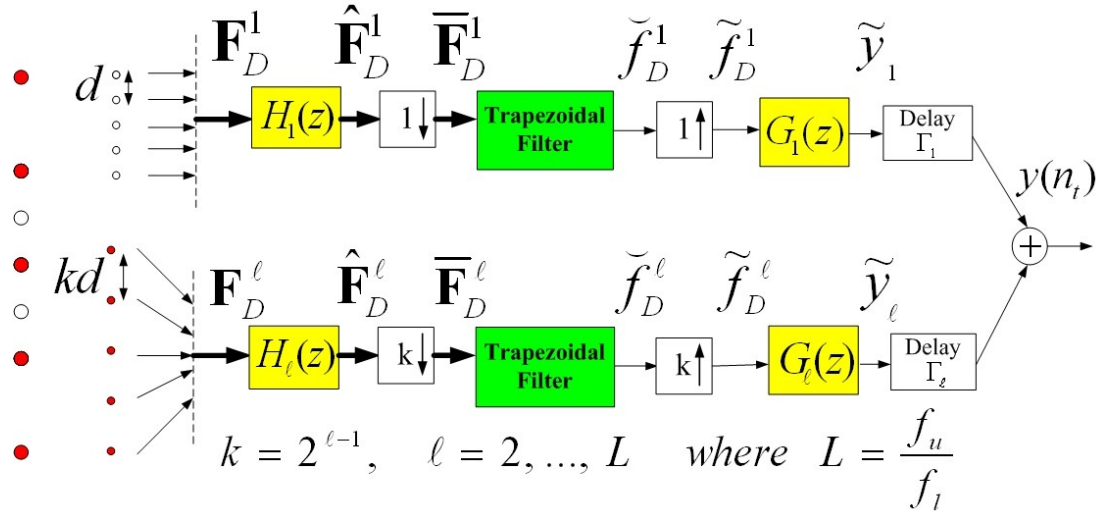

Figure 2.12. Structure of the L -subband beamformer

Lemma 2.1 implies that the ROS of $\overline{\mathbf{F}}_D^\ell$ is located on the line $(\omega_z / 2\pi d) - \cos(\theta)(\omega_t / 2\pi c T_s) = 0$. Clearly, the ROS for all subbands, i.e. $\ell = 1,...,L$ is the same. Thus, the same TF can be used for all subbands. Another interpretation of Lemma 2.1 is that downsampling in space and time with the same rate for each subband results in mapping the L octaves of the original signal $f(t)$ into the top octave. A graphical illustration of this will be presented in the following example.

Example 3 – An illustration for Lemma 2.1

Two broadband PWs are considered; one as the desired PW (DOA=55^o) and the other one as an interference (DOA=120^o). For both cases the spectrum of the signal is equal to 1 within $\omega_t = [\pi / 20 \;\; 4\pi / 5]$. Since $(4\pi / 5)/(\pi / 20) = 2^4$, a four-octave beamformer is needed. The performance of the subband beamformer is illustrated in the frequency domain in Figure 2.13. The ROS of the 2D FT of the signals received by the ℓ^{th} subarray ($\mathbf{F}_D^\ell$, $\ell = 1,...,4$ see Figure 2.12) are shown in Figure 2.13 (a)-(d). The horizontal and vertical axes are ω_z and ω_t,

respectively. The ROS of the desired and interference spectrums are shown by different colors. In Figure 2.13 (b)-(d), aliasing can be observed due to spatial subsampling. Using $H_\ell(z)$ to extract the related octave of the signal spectrum, aliasing is eliminated as it can be seen from the ROS of the 2D FT of the filter output $\hat{\mathbf{F}}_D^\ell$, in Figure 2.13 (e)-(h). Then, $\hat{\mathbf{F}}_D^\ell$ is downsampled by $2^{\ell-1}$. The ROS of the 2D FT of the resulting $\overline{\mathbf{F}}_D^\ell$ is shown in Figure 2.13 (i)-(l). Clearly, the ROS of $\overline{\mathbf{F}}_D^\ell$ for all subbands are the same (As expected from Lemma 2.1) and thus the same TF can be used in all subbands as shown in Figure 2.13 (m).

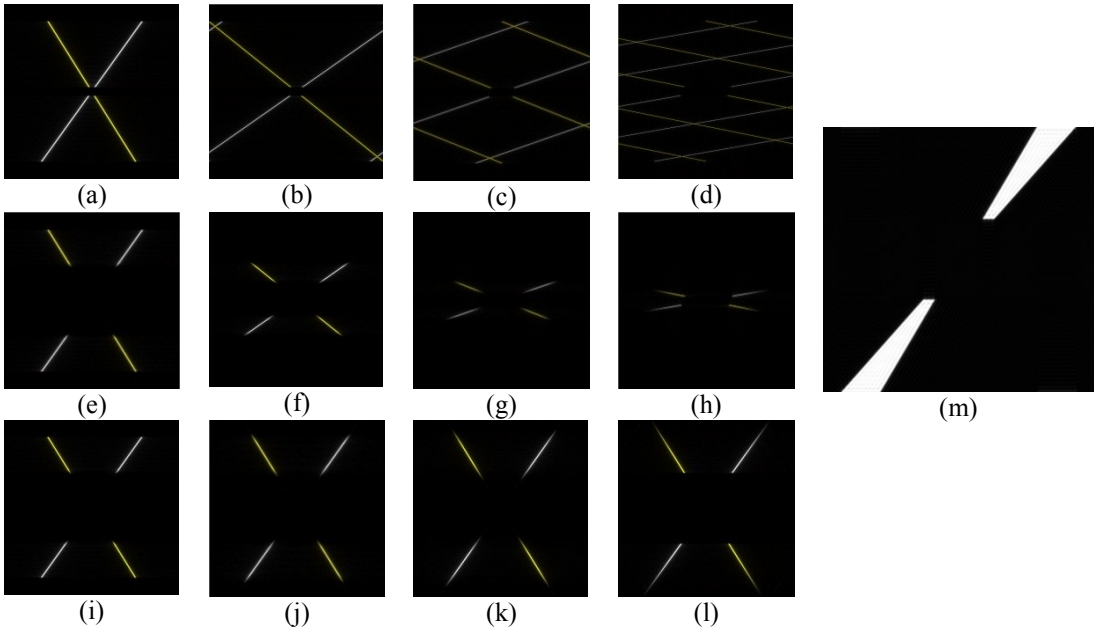

Figure 2.13. ROS of 2D Fourier Transforms of (see Figure 2.12) (a) $\mathbf{F}_D^1$, (b) $\mathbf{F}_D^2$, (c) $\mathbf{F}_D^3$, (d) $\mathbf{F}_D^4$, (e) $\hat{\mathbf{F}}_D^1$, (f) $\hat{\mathbf{F}}_D^2$, (g) $\hat{\mathbf{F}}_D^3$, (h) $\hat{\mathbf{F}}_D^4$, (i) $\overline{\mathbf{F}}_D^1$, (j) $\overline{\mathbf{F}}_D^2$, (k) $\overline{\mathbf{F}}_D^3$, (l) $\overline{\mathbf{F}}_D^4$, (m) magnitude response of the trapezoidal filter

It should be pointed out that Lemma 2.1 was derived based on the assumption that the length of subarrays is infinite. The effect of the finite aperture is discussed in the following paragraph.

Discussion about Finite Aperture Effect for Different Subarrays:

In Section 2.3.2, the finite aperture effect versus the number of sensors was discussed for ULA. In NAs, different subarrays have the same number of sensors but dissimilar finite aperture effect due to the different distance between elements. Sampling the PW by ℓ^{th} subarray can be modeled as multiplying the signal by a finite impulse train which is depicted in Figure 2.14 (left). In the frequency domain, the 2D FT of the continuous signal would be convolved with the FT of the finite impulse train shown in Figure 2.14 (right). For different subarrays the height will remain the same (due to the same number of sensors in each subarray) but the width of mainlobe shrinks as ℓ increases ($\ell = 1,2,...,L$). This effect is illustrated in Figure 2.15 where $N_z = 5$ (11 sensors), $\theta = 45^0$, $f_l = 200$, $f_u = 3200$, and $f_s = 6400$. One can see as ℓ is increasing the width around the ROS of the incoming PW is decreasing. Also as expected from Eq.(B.1) in Appendix B, Figure 2.15 indicates that the ROS of the 2D FT of the received signal by ℓ^{th} subarray is located on the line $(\omega_z / 2\pi d) - 2^{\ell-1}\cos(\theta)(\omega_t / 2\pi c T_s) = 0$.

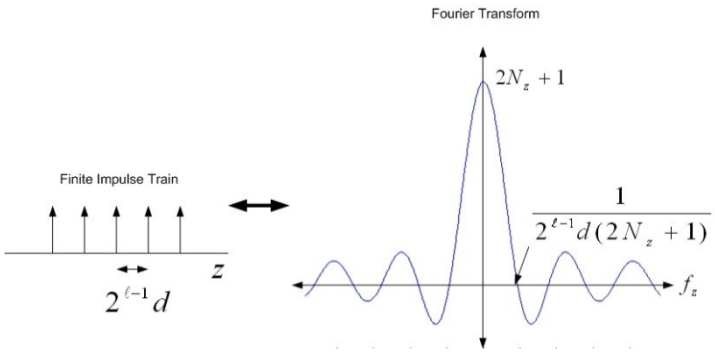

Figure 2.14. Finite Aperture Effect

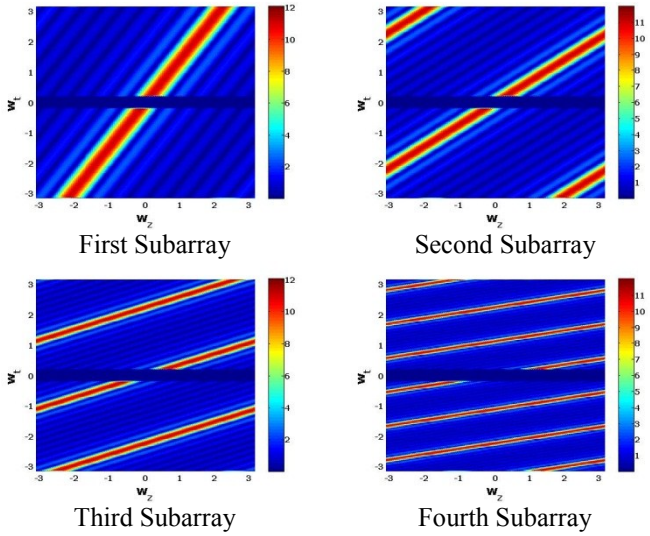

Figure 2.15. 2D FT of the received signals by different subarrays

Lemma 2.1 further implies that the 2D FIR TFs in Figure 2.12 can be designed such that they have the passband containing the ROS of $\overline{\mathbf{F}}_D^{\ell}$ as shown in Figure 2.16 (the yellow trapezoidal areas show the passband) and group delay of N_{TF} [31]. The center sensor is selected as the output of the TF in the ℓ^{th} subband. This signal is upsampled by $2^{\ell-1}$, passed through a synthesis filter $G_\ell(z)$ with group delay of N_G. Ideally, $G_\ell(z)$ and $H_\ell(z)$ have the same frequency specifications for passband and stopband areas. In order to compensate the amplitude attenuation by $1/2^{\ell-1}$ due to downsampling, the amplitude of $G_\ell(z)$ within passband is set to $2^{\ell-1}$. For the resulting signal $\widetilde{y}_\ell(n_t)$ the following lemma can be formulated:

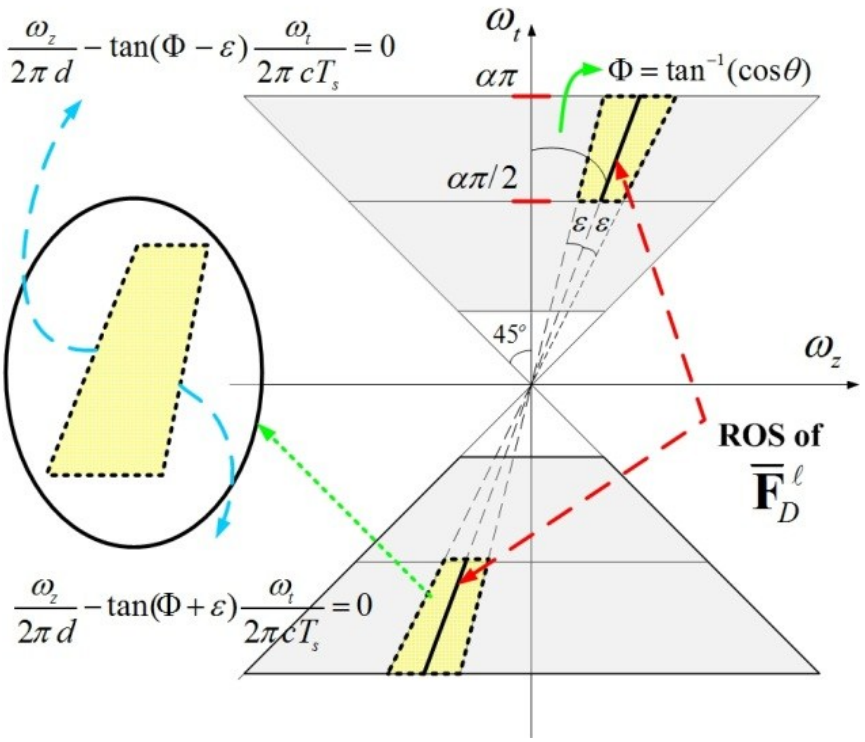

Figure 2.16. ROS of $\overline{\mathbf{F}}_D^{\ell}(f_z, f_{ct})$, and the passband area of the 2D TF

Lemma 2.2: The output of each subband beamformer, $\widetilde{y}_\ell(n_t)$ (see Figure 2.12), is a shifted version of the part of $f(t)$, which is included in the ℓ^{th} octave. The shift value is equal to $2^{\ell-1}N_{TF} + N_H + N_G$ (See Appendix C).

Finally, as shown in Figure 2.12, $\widetilde{y}_\ell(n_t)$ is delayed by Γ_ℓ to align all subband outputs. Γ_ℓ is given by:

$$\Gamma_\ell = (2^{L-1} - 2^{\ell-1})N_{TF}, \quad for \ \ \ell = 1, 2, ..., L \tag{2.10}$$

so that the total delay for all subbands is the same, given by $\Delta = 2^{L-1}N_{TF} + N_H + N_G$. The outputs from each subband are summed together to give the original sampled signal $f(n_t T_s)$ delayed by Δ.

Example 4 - An Illustration for Lemma 2.2

To illustrate the relationship between the output signals of the various subbands consider an example where $N_{TF}=10$, $N_H=33$, $N_G=33$, and $L=4$. In Figure 2.17 (b), the top subplot is $f(t)$ which is decomposed into its four octaves in Figure 2.17 (a). The second subplot in Figure 2.17 (b) is $\widetilde{y}_1(n_t)$. Clearly, it is the shifted version of the first octave in which the time shift is equal to 76 ($\ell=1$). The middle subplot $\widetilde{y}_2(n_t)$ is the shifted version of the second octave in which the time shift is equal to 86 ($\ell=2$). The time-shift for the third and fourth subbands is equal to 106 and 146, and they entail information of the third and fourth octaves of $f(t)$ respectively, as expected from the Lemma 2.2.

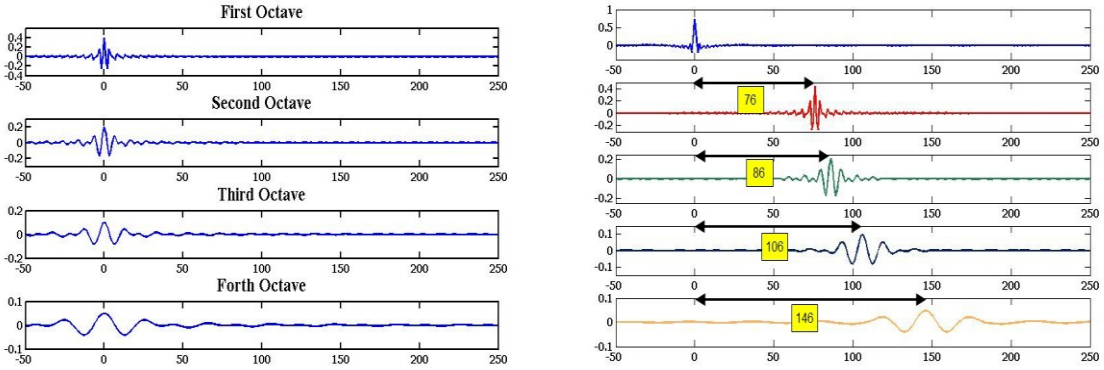

(a) (b)

Figure 2.17. (a) Different octaves of $f(t)$ in time domain, (b) $f(t)$ and $\widetilde{y}_\ell(n_t)$ for $\ell=1,2,3,4$

During the above analysis, it was deemed that the analysis and synthesis filters are ideal. In practice, the PR condition must be taken into consideration; otherwise there is some distortion at the output specifically where different octaves meet. The filter bank design approach will be

discussed in Chapter 3 in details. To illustrate the good performance of the method proposed in Section 2.5, it is compared with the method discussed in Section 2.4 in terms of beampattern and computational complexity in the next section.

2.6 Nested Uniform Linear Arrays vs. Uniform Linear Array

The performance of the method proposed in Section 2.5 (denoted as TF-NA here) is evaluated and compared with the method presented in Section 2.4 [20] (denoted as TF-ULA here) in terms of beampattern and computational complexity. The proposed method employs nested arrays and TF. The other approach (TF-ULA) is composed of a ULA and TF. Because of the two types of antenna (nested and uniform), the following two scenarios are considered:

i. the same number of sensors (which results in different aperture size)
ii. the same aperture size (which results in different number of sensors)

The goal here is to design a beamformer that receives PWs propagating from $\theta = 80^o$. The normalized temporal bandwidth of the desired PW is one within $[0.0606\pi, 0.9697\pi]$ and zero elsewhere ($\alpha = 0.9697$). Since $0.9697\pi / 0.0606\pi = 2^4$, a four-octave beamformer ($L = 4$) is needed for the TF-NA. Let's assume NAs structure has 21 sensors in each individual subarray which results in 51 total sensors (many elements are superimposed) and a maximal aperture size of $160\,d$. For the comparison with TF-ULA, the ULA needs to have 51 and 161 sensors for scenarios 1 and 2, respectively.

To perform beamforming, for both methods TF is designed with $\Phi = 9.851 \text{r}^{o}\,(\tan^{-1}(\cos 80^{o}))$ and $\varepsilon = 5^{o}$. The passband area of TF in TF-ULA must enclose the whole ROS of the PW (i.e. $\beta_1 = 1$ and $\beta_2 = 0.0625$ in Eq.(2.7)). According to Lemma 2.1 and Eq.(2.9), the passband area of TF for TF-NA just needs to include the top octave (ideally $\beta_1 = 1$ and $\beta_2 = 0.5$ in Eq.(2.7) as shown in Figure 2.16), but in order to achieve (almost) PR by the filter bank (it will be discussed in Chapter 3), it is required that the signal in the transition band of the analysis and synthesis filters is available at the output of TF. For this reason the passband area of TF for TF-NA was considered larger than the ideal case ($\beta_1 = 1$ and $\beta_2 = 0.3125$).

For the first scenario, N_z in Eq.(2.8) is set to 10 and 25 for TF-NA and TF-ULA respectively, and N_{TF} is set to 40 for both methods. In this case, the 3D beampattern for both methods is shown in Figure 2.18 (a)-(d) from isometric and top views. Also for a better look, the beampattern versus DOA is shown in Figure 2.19 (a) and (b) within $[0.0606\pi, 0.9697\pi]$. It can be concluded that as the frequency decreases the selectivity (ability to resolve two different PWs coming from different directions) of TF-ULA is decreasing, but for TF-NA the beampattern is almost frequency invariant. The advantage of using NAs is that the effective aperture for low frequencies ($160\,d$) is much larger than the aperture of the ULA ($50\,d$) which leads to the higher selectivity at low frequencies.

For the second scenario (same aperture size of $160\,d$), N_z and N_{TF} in Eq.(2.8) for TF-ULA were set to 80 and 40, respectively. Therefore, the size of TF is 161×81 (versus 21×81 for TF-NA). In this case, the 3D beampattern of TF-ULA is shown in Figure 2.18 (e)-(f) from isometric

and top views. Also, the beampattern versus DOA is shown in Figure 2.19 (c) within $[0.0606\pi, 0.9697\pi]$. It can be inferred that the spatial selectivity of TF-ULA at lower frequencies is significantly improved due to the larger aperture. This, however, comes at the cost of having almost 3 times the number of sensors used for the TF-NA.

The computational complexity (CC) of TF-NA and TF-ULA are compared in terms of the number of arithmetic operations required to compute N_s samples of the output as given in Table 2.2. As can be seen, the CC of TF-NA mainly depends on the order of analysis and synthesis filters (N_A). Setting L to 4 and considering three different values for N_A , the CC of the TF-NA is compared with TF-ULA for the same number of sensors (the first scenario) changing from 9 to 251. The comparison is depicted in Figure 2.20 (a) which implies that when N_A is pretty large the number of operations needed by the TF-NA is higher than that of TF-ULA. However, since the different subbands can be implemented in parallel, TF-NA can still be faster than TF-ULA. For the case of the same aperture size (the second scenario, for the aperture size from $17d$ to $801d$), the CC of TF-NA is compared with that of TF-ULA in Figure 2.20 (b). Again, L was set to 4 and three different values for N_A were considered. It can be seen that for the same aperture size, the TF-NA entails less computations. Besides, for the same aperture size, the implementation of the NAs is more economical than ULA in terms of number of sensors.

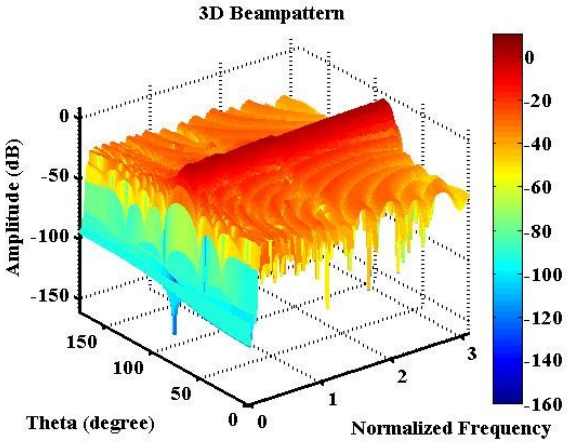

(a) TF-NA (isometric view)

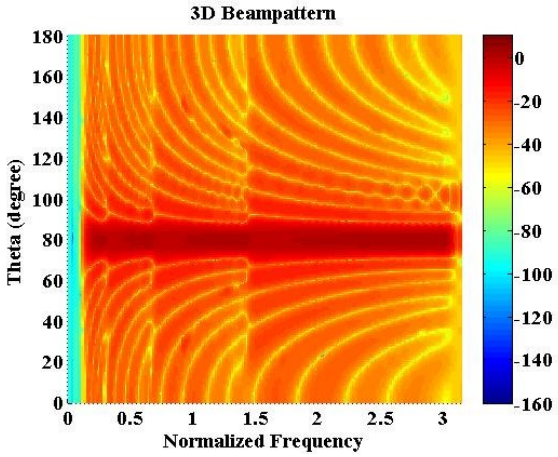

(b) TF-NA (top view)

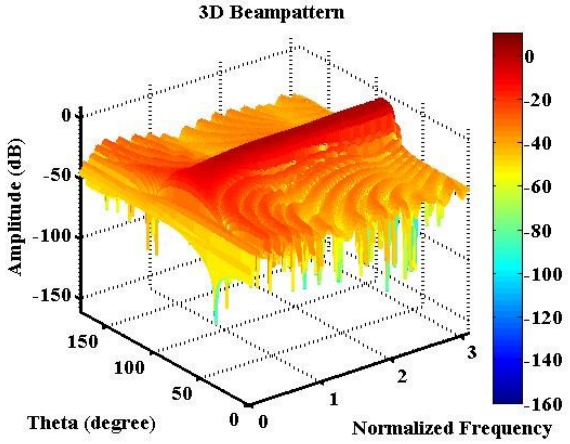

(c) TF-ULA for the first scenario (isometric view)

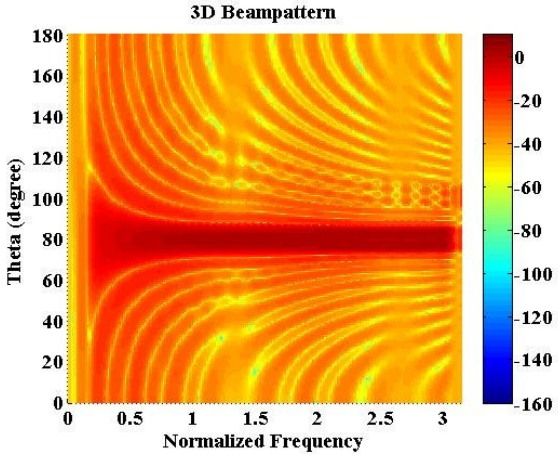

(d) TF-ULA for the first scenario (top view)

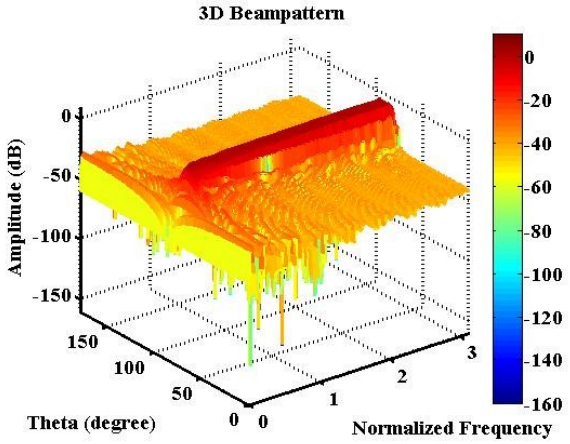

(e) TF-ULA for the second scenario (isometric view)

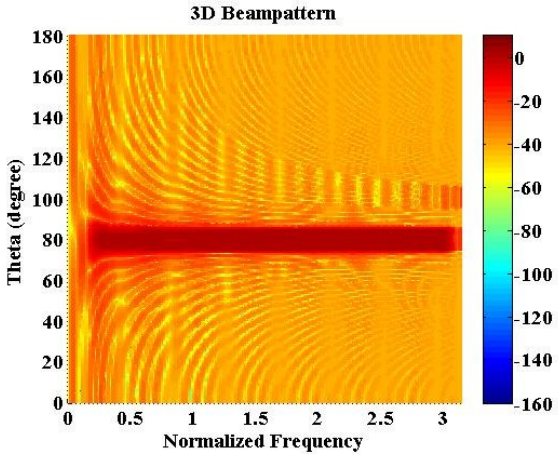

(f) TF-ULA for the second scenario (top view)

Figure 2.18. 3D beampattern of the proposed method and TF-ULA

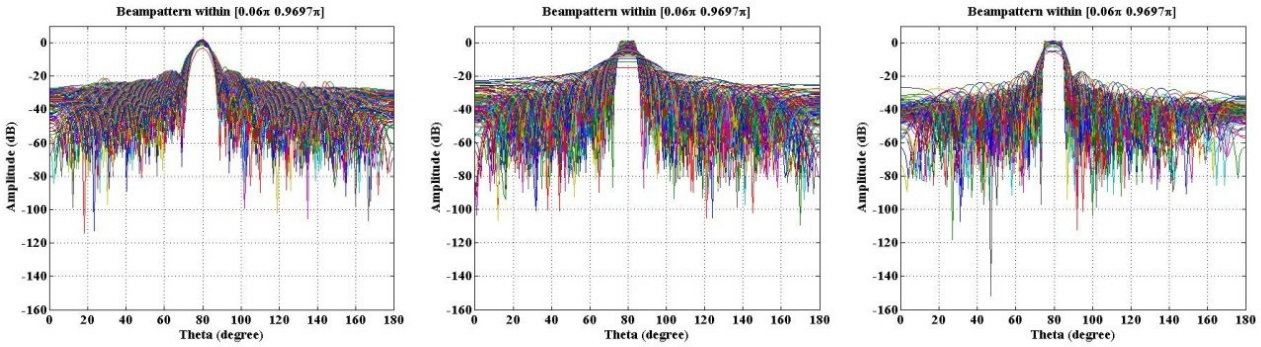

(a) TF-NA (b) TF-ULA, first scenario (c) TF-ULA, second scenario

Figure 2.19. Beampattern of the proposed method and TF-ULA within $[0.0606\pi, 0.9697\pi]$

Table 2.2. The computational complexity of the different methods

	Number of arithmetic operations
TF-NA	$\left[(2\mathrm{O}_z\mathrm{O}_{\mathrm{TF}}-1)\times\sum_{i=0}^{L-1}(0.5)^i+(\mathrm{O}_z+1)(2N_A-1)L\right]\times N_s$
TF-ULA	$(2\hat{\mathrm{O}}_z\mathrm{O}_{\mathrm{TF}}-1)\times N_s$

N_s : output length, N_A : order of analysis (synthesis) filters, O_{TF} : temporal order of TF

O_z : spatial order of TF in TF-NA (equal to number of sensors in each subband)

$\hat{\mathrm{O}}_z$: spatial order of TF in TF-ULA (equal to total number of sensors)

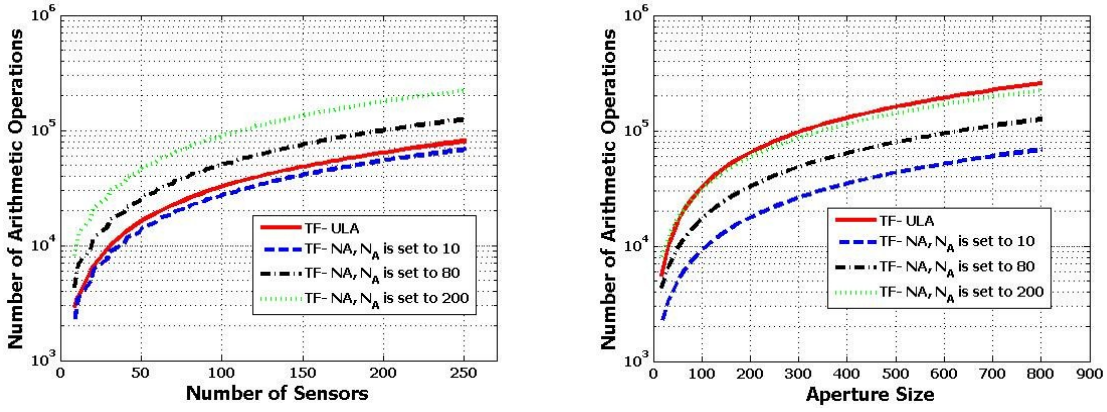

(a) (b)

Figure 2.20. Cost of Computations of TF-ULA and TF-NA (a) the same number of sensors, (b) the same aperture size

2.7 Wideband Beamforming Using Planar Array

Both methods presented in the Section 2.4 and 2.5 use linear arrays, and accordingly they are just able to separate PWs with distinct zenith angles (Figure 2.2, Eq. (2.4), and Eq. (2.5)). In order to jointly cover zenith and azimuth angles, 2D arrays need to be deployed. Consider the PW is being received by a planar array on the x-y plane (z is zero). From Eq. (2.3), we get:

$$f(t-\tau_p) = f(t + c^{-1}(\sin\theta\cos\varphi\, x + \sin\theta\sin\varphi\, y)) \tag{2.11}$$

The 3D Fourier transform (3D FT) of this PW is given by [22]- [23]:

$$\begin{aligned}&\mathbf{F}(f_x, f_y, f_{ct}) = \\ &c\delta(f_x - \sin\theta\cos\varphi\, f_{ct})\delta(f_y - \sin\theta\sin\varphi\, f_{ct})F(cf_{ct})\end{aligned} \tag{2.12}$$

From Eq.(2.12), it is clear that the ROS of the 3D FT of the PW is a line with an angle of $\tan^{-1}(\sin(\theta))$ with the f_{ct} axis as shown in Figure 2.21 (a) [23]. Considering all possible DOAs, i.e. $\theta = [-90^o\ 90^o]$ and $\varphi = [0^o\ 360^o]$, one can conclude that the ROS is always confined within a 45^0 cone, which is usually referred to as the light cone [85], as shown in Figure 2.21 (b).

2.7.1 Review of Hexagonal and Rectangular Sampling Patterns

The received continuous signal can be spatially sampled using a rectangular or hexagonal 2D array, shown in Figure 2.22, and uniformly sampled in time. The corresponding space/time sampling matrices for the rectangular and the hexagonal arrays can be given using the following generating matrices for the corresponding 3D lattices [86]:

$$V_r = \begin{bmatrix} d & 0 & 0 \\ 0 & d & 0 \\ 0 & 0 & T_s \end{bmatrix}, \quad V_h = \begin{bmatrix} 2d/\sqrt{3} & -d/\sqrt{3} & 0 \\ 0 & d & 0 \\ 0 & 0 & T_s \end{bmatrix} \tag{2.13}$$

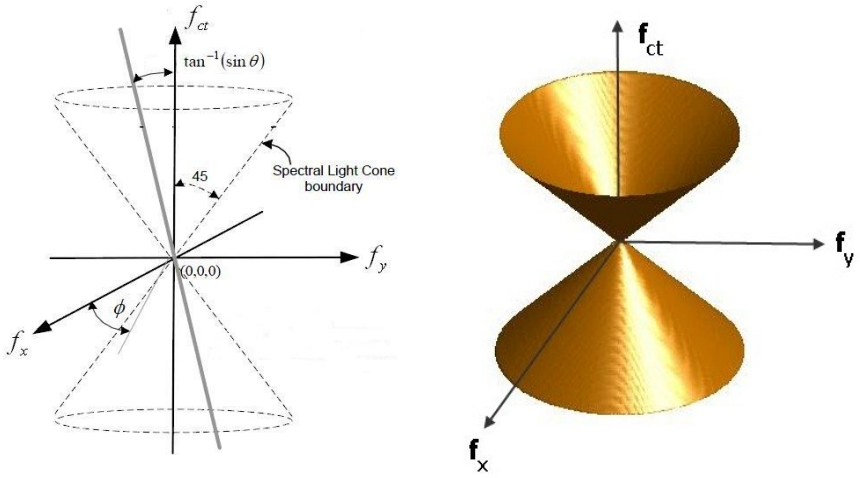

(a) (b)

Figure 2.21. ROS of the 3D FT of PW

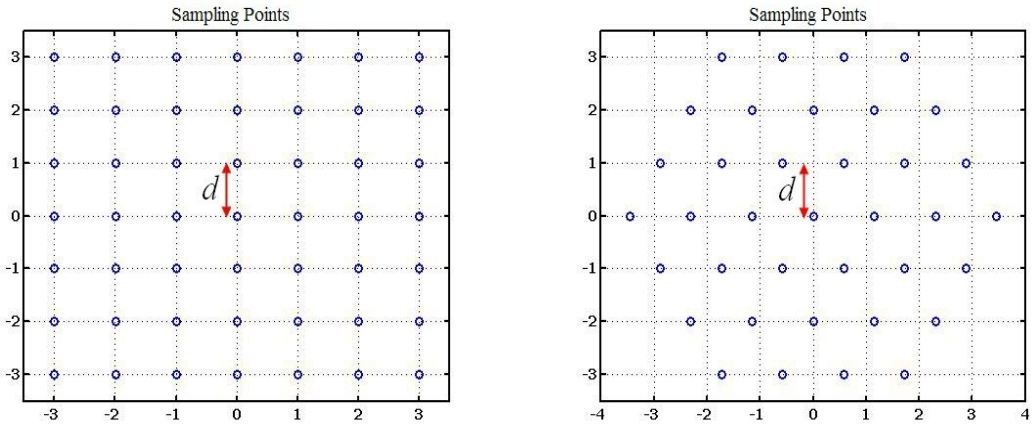

(a) Rectangular 2D Array (b) Hexagonal 2D Array

Figure 2.22. Rectangular and hexagonal sampling pattern (unit length is d)

The Fourier transform of the sampled signal is a periodic version of the continuous one with the periodicity matrix being the generating matrix of the reciprocal lattice [86]. They can be obtained using:

$$V_i^T U_i = I \quad \text{for} \quad i = r, h \tag{2.14}$$

leading to:

$$U_r = \begin{bmatrix} 1/d & 0 & 0 \\ 0 & 1/d & 0 \\ 0 & 0 & 1/T_s \end{bmatrix}, U_h = \begin{bmatrix} \sqrt{3}/2d & 0 & 0 \\ 1/2d & 1/d & 0 \\ 0 & 0 & 1/T_s \end{bmatrix} \tag{2.15}$$

The Voronoi cell of the reciprocal lattice [86] for rectangular sampling is a rectangular parallelepiped which when using normalized frequencies is equivalent to the Nyquist cube. In the case of hexagonal sampling, the Voronoi cell of the reciprocal lattice is a hexagonal prism with a regular hexagon for the spatial frequencies. Figure 2.23 graphically illustrates the difference between the ROS of the Fourier transforms of the sampled signals (for all DOAs) resulting from rectangular and hexagonal sampling. The periodicity (described by U_r and U_h) in the direction of the spatial frequencies is different while the periodicity in the temporal frequency direction is the same for both cases (not shown in Figure 2.23). For PWs bandlimited with $f_{\max}$ from all DOAs, aliasing can be avoided if the periodically repeated light cones do not overlap as shown in Figure 2.23. This implies that the temporal sampling period T_s must be less then $1/2f_{\max}$. Further, using $|f_{ct}| \le c^{-1} f_{\max}$, follows that $|f_x| \le c^{-1} f_{\max}$ and $|f_y| \le c^{-1} f_{\max}$. Thus to avoid aliasing due to spatial sampling, d must be less than $c/2f_{\max}$. Setting T_s and d to these values, the sampling density [86] ($1/|\det(V)|$) for rectangular and hexagonal sampling patterns is $8f_{\max}^3/c^2$

and $4\sqrt{3}f_{\max}^3/c^2$, respectively. This means that for a given aperture area and maximal temporal frequency, a hexagonal arrangement of spatial sensors will lead to 13.4% fewer sensors than a rectangular arrangement [87]- [88].

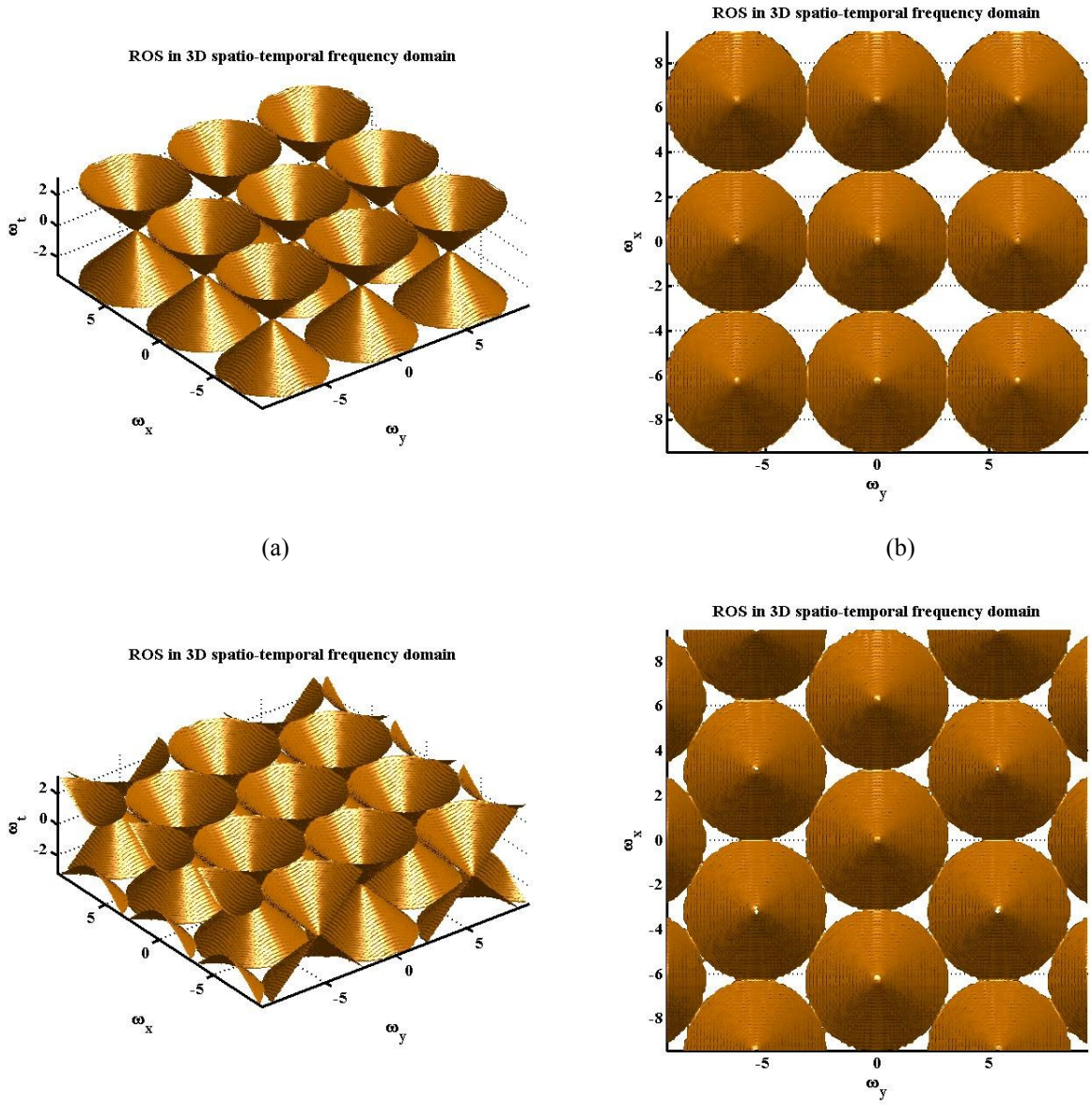

Figure 2.23. The repetition of light cone in the frequency domain using rectangular sampling: (a) from the isometric view, (b) from the top view, and using hexagonal sampling: (c) from the isometric view, (d) from the top view.

2.8 Broadband Beamforming Using a Hexagonal Array and a Hexagonal FIR Frustum Filter

The objective is to recover $f(t)$, the temporal intensity function of the broadband PW received from the desired DOA and reject interference signals with different DOAs. Eq.(2.12) indicates that the ROS of the 3D FT of the PW is located on a line whose direction depends on the DOA. Disturbances with different DOAs will have ROS in 3D frequency domain on lines with different directions. Therefore the broadband PW from a desired direction $[\theta_s, \varphi_s]$ can be passed while disturbances are attenuated using a frustum filter [23] with specifications given by:

$$H(\omega_x, \omega_y, \omega_t) = \begin{cases} 1 & \sqrt{(\omega_x - \kappa_1\omega_t)^2 + (\omega_y - \kappa_2\omega_t)^2} \le \tan(\alpha)\omega_t, \quad \omega_t \in [\omega_{\min}, \omega_{\max}] \\ 0 & otherwise \end{cases} \tag{2.16}$$

where ω_x, ω_y and ω_t are the normalized spatial and temporal frequencies, $\kappa_1 = \sin(\theta_s)\cos(\varphi_s)$, and $\kappa_2 = \sin(\theta_s)\sin(\varphi_s)$. The selectivity of the filter can be controlled using the parameter α. The impulse response $h(n_x, n_y, n_t)$ of the corresponding spatial-temporal domain 3D FIR filter can be obtained using the hexagonal Fourier transform pairs defined in Eq.(2.17) and Eq.(2.18) from [87]. Using Eq.(2.18), $h(n_x, n_y, n_t)$ is obtained in Eq.(2.19) where J_1 is the first order Bessel function. The integral in Eq.(2.19) can be numerically calculated using Simpson method [89].

$$X(\omega_x,\omega_y,\omega_t)=\sum_{n_x=-\infty}^{\infty}\sum_{n_y=-\infty}^{\infty}\sum_{n_t=-\infty}^{\infty}x(n_x,n_y,n_t)\exp\left[-j\left(\frac{2n_x-n_y}{\sqrt{3}}\omega_x+n_y\omega_y+n_t\omega_t\right)\right] \quad (2.17)$$

$$x(n_x,n_y,n_t)=\frac{1}{8\pi^3\sqrt{3}}\int_{-\pi}^{\pi}\int_{-\pi}^{\pi}\int_{-\pi\sqrt{3}}^{\pi\sqrt{3}}X(\omega_x,\omega_y,\omega_t)\exp\left[j\left(\frac{2n_x-n_y}{\sqrt{3}}\omega_x+n_y\omega_y+n_t\omega_t\right)\right]d\omega_x d\omega_y d\omega_t \quad (2.18)$$

$$h(0,0,0)=\frac{\tan^2\alpha}{12\pi^2}[\omega_{\max}^3-\omega_{\min}^3]$$

$$h(0,0,n_t\neq 0)=\frac{\tan^2\alpha}{4\pi^2}\left[\left(\frac{\omega_{\max}^2\sin(\omega_{\max}n_t)-\omega_{\min}^2\sin(\omega_{\min}n_t)}{n_t}\right)+2\left(\frac{\omega_{\max}\cos(\omega_{\max}n_t)-\omega_{\min}\cos(\omega_{\min}n_t)}{n_t^2}\right)\right.$$
$$\left.-2\left(\frac{\sin(\omega_{\max}n_t)-\sin(\omega_{\min}n_t)}{n_t^3}\right)\right] \quad (2.19)$$

Otherwise:

$$h(n_x,n_y,n_t)=\frac{\tan\alpha}{2\pi^2\sqrt{\left(\frac{2n_x-n_y}{\sqrt{3}}\right)^2+n_y^2}}\times$$
$$\int_{\omega_{\min}}^{\omega_{\max}}\omega_t\,J_1\left(\omega_t\tan\alpha\sqrt{\left(\frac{2n_x-n_y}{\sqrt{3}}\right)^2+n_y^2}\right)\cos\left(\omega_t\left[n_t+\kappa_1\left(\frac{2n_x-n_y}{\sqrt{3}}\right)+\kappa_2\,n_y\right]\right)d\omega_t$$

In order to truncate the impulse response, a hexagonal window (with a similar geometry as the one shown in Figure 2.22 (b)) is employed. It has N_H (odd number) elements in the horizontal row through the origin and the total number of elements is $1+0.75(N_H^2-1)$ [1]. The spatial-temporal window is defined as:

$$window\ (n_x, n_y, n_t) = \begin{cases} 1 & \text{within the hexagonal grid and } |n_t| \le N_t \\ 0 & \text{otherwise} \end{cases} \tag{2.20}$$

Finally, the hexagonal FIR frustum filter can be obtained as ($\circ$ is Hadamard or element-wise product):

$$h_{\text{frustum}}(n_x, n_y, n_t) = h(n_x, n_y, n_t) \circ window\ (n_x, n_y, n_t) \tag{2.21}$$

Example: Hexagonal FIR Frustum Filter Design

Using Eq. (2.19), Eq. (2.20), and Eq. (2.21), a frustum filter was designed with $N_H = 35$, $N_t = 40, \omega_{\min} = 0.2, \omega_{\max} = 3$ (normalized temporal frequencies) $\theta_s = 20^o$, $\varphi_s = 45^o$, and $\alpha \approx 7.5^o$. Figure 2.24 (a-b) shows the -3 dB surface of the amplitude response of the obtained filter. It should be noted here that the amplitude response shown in Figure 2.24 has been obtained using the hexagonal Fourier transform implementation as in [90] and is repeated hexagonally using U_h . Further, the amplitude response at two constant temporal frequencies, $\pi/10$ and $3\pi/4$, is shown in Figure 2.24 (c) and (d) respectively. It is interesting to note that the amplitude response within the passband area at high frequencies is almost 0 dB, and for low frequencies is almost -12 dB which degrades the performance. As was mentioned earlier, this amplitude attenuation at

low frequencies is due to the fact that the ratio of aperture to wavelength at low frequencies is much smaller than at high frequencies [3]. To tackle this drawback the aperture size can be increased at the cost of having more sensors and more computations. Another solution is using nested arrays which will be discussed in the next section.

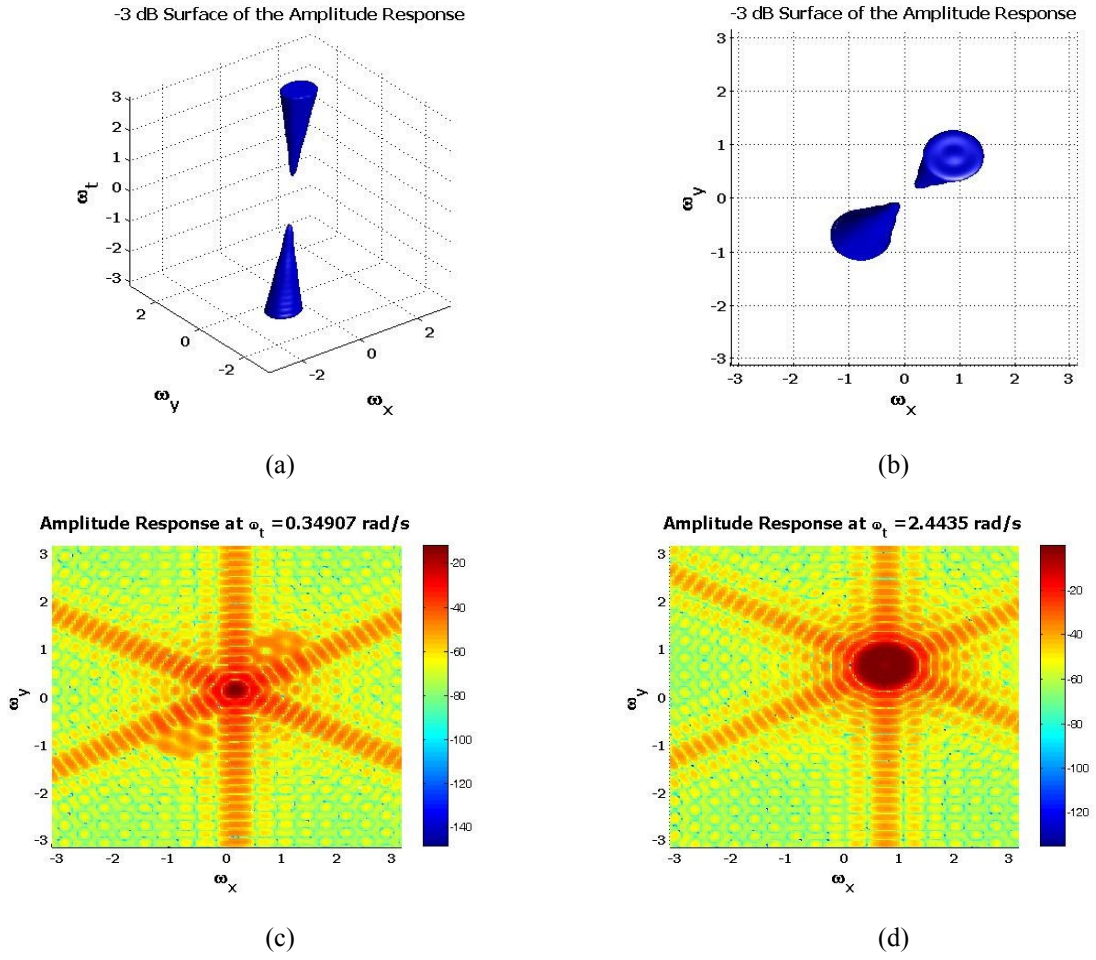

Figure 2.24. -3 dB surface of the obtained hexagonal FIR frustum filter: (a) isometric view, (b) top view, The amplitude response of the obtained hexagonal FIR frustum filter at temporal frequency (c) $\pi/10$, (d) $3\pi/4$

2.9 Wideband Beamforming using Nested Hexagonal Arrays, Frustum Filters, and Multirate Techniques

In this section, a broadband beamformer will be presented which is based on nested hexagonal arrays, frustum filters and multirate filtering techniques. A nested hexagonal array (NHA) consists of several hexagonal arrays in the x-y plane (each one called subarray) where in the ℓ^{th} subarray ($\ell = 1,2,...,L$), the distance between elements is $2^{\ell-1}$ times larger than the first subarray. An example of such an antenna with 4 subarrays and 37 elements ($N_H = 7$) per subarray is shown in Figure 2.25. Clearly, many elements (21) of the different subarrays are superimposed.

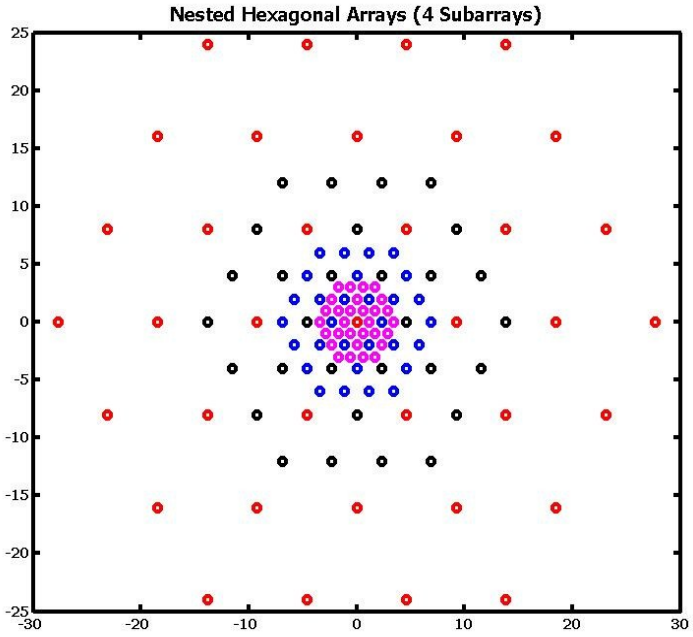

Figure 2.25. The structure of NHA (different colors represent different subarrays)

2.9.1 Proposed Beamformer

The structure of the proposed beamformer is shown in Figure 2.26. This beamformer is an extension of the broadband beamformer presented in [32] using rectangular arrays. Consider a PW with a temporal bandwidth given by $[\omega_{\min}\ \omega_{\max}]$ and $\omega_{\max}/\omega_{\min}=2^{L}$. This implies that the proposed beamformer will consist of L different subarrays. The impinging PW is received by NHA and the received signal at each array element is temporally sampled with the rate of f_s. The ℓ^{th} subarray ($\ell=1,2,...,L$) is processing the ℓ^{th} octave, namely $\omega_{\max}/2^{\ell}\le\omega_t\le\omega_{\max}/2^{\ell-1}$. Analysis filters, $H_\ell(z)$ with appropriate passbands, i.e. $[\omega_{\max}/2^{\ell}\ \ \omega_{\max}/2^{\ell-1}]$, are used to extract the corresponding octave for each subarray. As a result of downsampling in space and time, the ROS of the 3D FT of all signals $\bar{\mathbf{f}}_{D_\ell}$ (see Figure 2.26), become the same. Ideally, the ROS of all $\bar{\mathbf{f}}_{D_\ell}$ is non-zero within $\omega_{\max}/2\le\omega_t\le\omega_{\max}$ [32]. Thus a hexagonal frustum filter whose passband encloses only the top half of ROS of the desired PW, i.e. $\omega_{\max}/2\le\omega_t\le\omega_{\max}$ can be used as the beamformer. This filter can be designed as discussed in the Section 2.8 (Eq. (2.19)). The output of the beamformer is upsampled to the original sampling rate, i.e. f_s and all replicas of the signal spectrum generated by upsampling except for the baseband copy are eliminated using a synthesis filter $G_\ell(z)$. The outputs of the different subarrays are aligned using appropriate delays and added. The sum is the output of the beamformer. This beamformer will be referred to as NHA-FF. A graphical example will be provided in Section 2.10 to illustrate how the proposed beamformer works. Also, the filter bank design approach will be discussed in Chapter 3 in details. At the rest of this section, an efficient implementation for the proposed beamformer shown in Figure 2.26 will be presented.

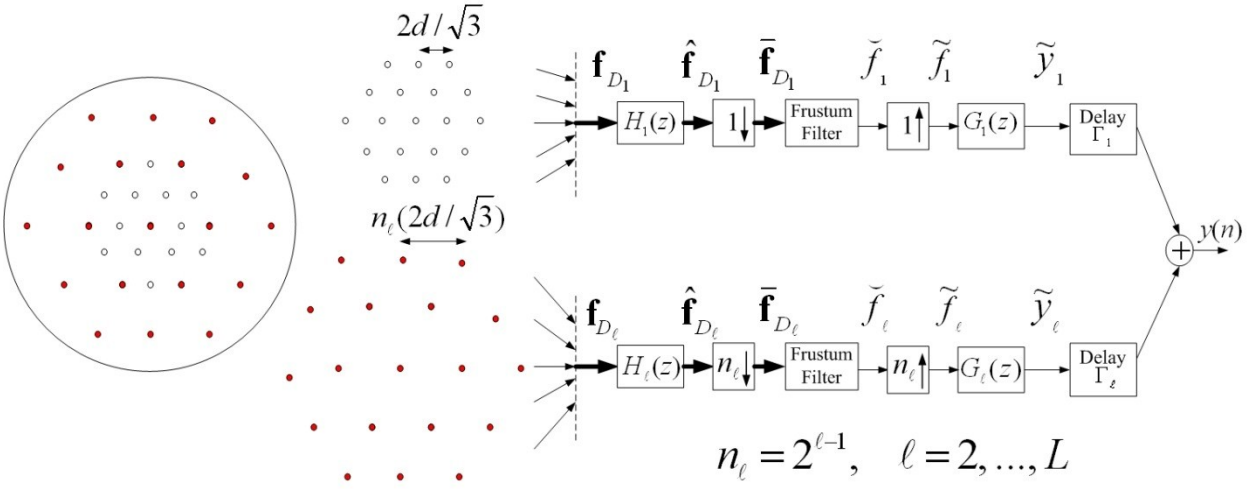

Figure 2.26. The structure of the proposed beamformer

2.9.2 Efficient Implementation

The computational efficiency of the proposed beamformer can be improved using the Nobel identity and polyphase structures [84] for the analysis and synthesis filters. To avoid computing unnecessary output samples which will be discarded by downsampling, the order of analysis filters and downsamplers can be changed. The ℓ^{th} analysis filter given by:

$$H_\ell(z) = \sum_{k=0}^{N-1} h_{\ell,k}\ z^{-k} \tag{2.22}$$

can be replaced by its polyphase structure using:

$$H_{\ell,i}(z^{n_\ell}) = \sum_{k=0}^{(N/n_\ell)-1} h_{\ell,\,i+kn_\ell} z^{-kn_\ell}, \quad i = 0,1,...,n_\ell - 1 \tag{2.23}$$

as shown in Figure 2.27 (a). N is the length of analysis/synthesis filters. Then, by pulling the downsampling operation to the right side of summation in Figure 2.27 (a) and applying the Nobel identity, the final structure, shown in Figure 2.27 (b), can be obtained. A commuter can be employed to eliminate the downsamplers and deliver successive samples to successive branches

[84]. Note that the coefficients of $H_{\ell,i}(z)$ are obtained by downsampling the coefficients of $H_\ell(z)$ by the rate $n_\ell = 2^{\ell-1}$ starting from $h_{\ell,i}$. The same procedure can be applied to the upsampling operation followed by synthesis filtering to avoid redundant computations. The final structure for this part is shown in Figure 2.27 (c). The major difference between the downsampling and upsampling configuration is the place that the commuter would start. The resulting beamformer is referred to as the modified NHA-FF.

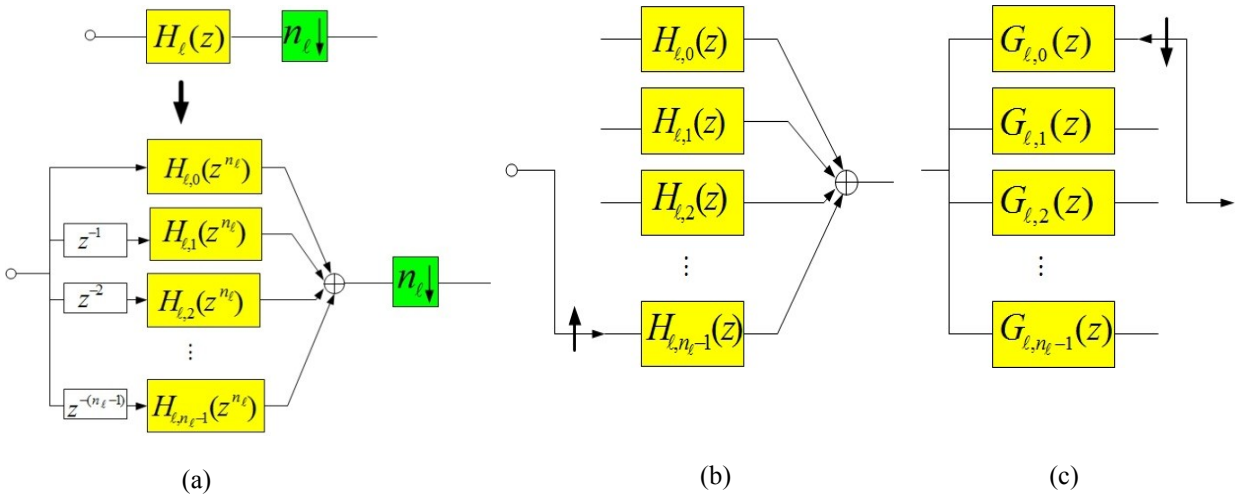

Figure 2.27. (a) Replacing an analysis filter by its polyphase structure, (b) Final structure for downsampling part, and (c) Final structure for upsampling part

2.10 Illustrative Examples

In this section, two examples will be provided to illustrate the functioning and evaluate the performance of the method proposed in Section 2.9. The first example graphically illustrates how the proposed beamformer works and in the second example the performance of the proposed beamformer and the hexagonal frustum filter (Section 2.8) are evaluated and compared in terms of beampattern and computational complexity.

2.10.1 Illustration of how the method works

Consider 5 broadband PWs propagating from the directions given in Table 2.3. The temporal Fourier transforms of the intensity functions $f_i(t),\ i=1,2,...,5$ are equal to one from 0.1904 ($\omega_{\min}$) to 3.0464 ($\omega_{\max}$) and zero elsewhere. Since $\omega_{\max}/\omega_{\min}=2^4$, the beamformer will have four subbands. The ROS of the signals in 3D frequency domain (obtained in Matlab as the area where the most energy of the signal is concentrated), calculated using the hexagonal Fourier transform implementation of [90], will be used to illustrate the function of the beamformer. The ROS of the signals received by different subbands ($\mathbf{f}_{D_\ell}$, $\ell=1,2,3,4$, (see Figure 2.26) are shown in Figure 2.28 (a-d). For the first subband, d in Eq. (2.13) is set to $c/2f_{\max}$ (aliasing-free condition [1]). For the ℓ^{th} subarray ($\ell=2,3,4$), the distance between elements is $2^{\ell-1}$ times larger than that of the first subarray (Figure 2.26), resulting in aliasing as seen in Figure 2.28 (b-d). The ℓ^{th} subarray ($\ell=1,...,4$) is processing the ℓ^{th} octave, i.e. $[\omega_{\max}/2^{\ell}\ \ \omega_{\max}/2^{\ell-1}]$ and $H_\ell(z)$ has the effect of extracting the desired octave. The ROS of the analysis filters' outputs for different subbands ($\hat{\mathbf{f}}_{D_\ell}$, $\ell=1,2,3,4$, see Figure 2.26) are shown in Figure 2.28 (e-h). The aliased components in Figure 2.28 (b-d) are non-zero outside the passband area of $H_\ell(z)$, $[\omega_{\max}/2^{\ell}\ \ \omega_{\max}/2^{\ell-1}]$, and therefore are eliminated (Figure 2.28 (f-h)). Next, the ℓ^{th} subband is downsampled by $2^{\ell-1}$. The ROS of the downsampled signals for the four subbands are shown in Figure 2.28 (i-l) ($\bar{\mathbf{f}}_{D_\ell}$, $\ell=1,2,3,4$, see Figure 2.26). It should be noted that due to the same sub-sampling rate in space and time, different frequency octaves are mapped into the top octave and the ROS of all subband signals ($\bar{\mathbf{f}}_{D_\ell}$) are the same. Thus, the same frustum filter with passband in the top octave can be used for all subbands to pass the desired signal and reject the interferences. Thus the

passband of the frustum filter does not include the low frequencies with poor selectivity (Figure 2.24 (c)).

The frustum filter with $\theta_s = 20^o$, $\varphi_s = 45^o$, and $\alpha \approx 10^o$ was designed to pass the first PW and reject the others. Figure 2.28 (i-l) also shows the -3 dB surface of the amplitude response of this filter. After filtering the center sensor ($n_x = n_y = 0$) is selected as the output [32], and upsampled by n_ℓ (to go back to the original sampling rate). To remove all replicas of the signal spectrum generated by upsampling except for the baseband copy, a synthesis filter $G_\ell(z)$ is used. Then, to align the outputs of the subband beamformers, appropriate delays are added and the aligned signals are summed to form the output.

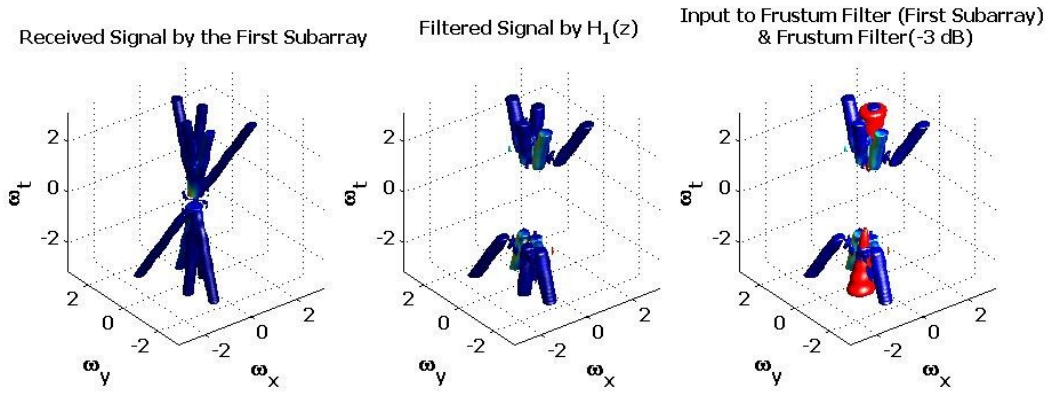

(a) (e) (i)

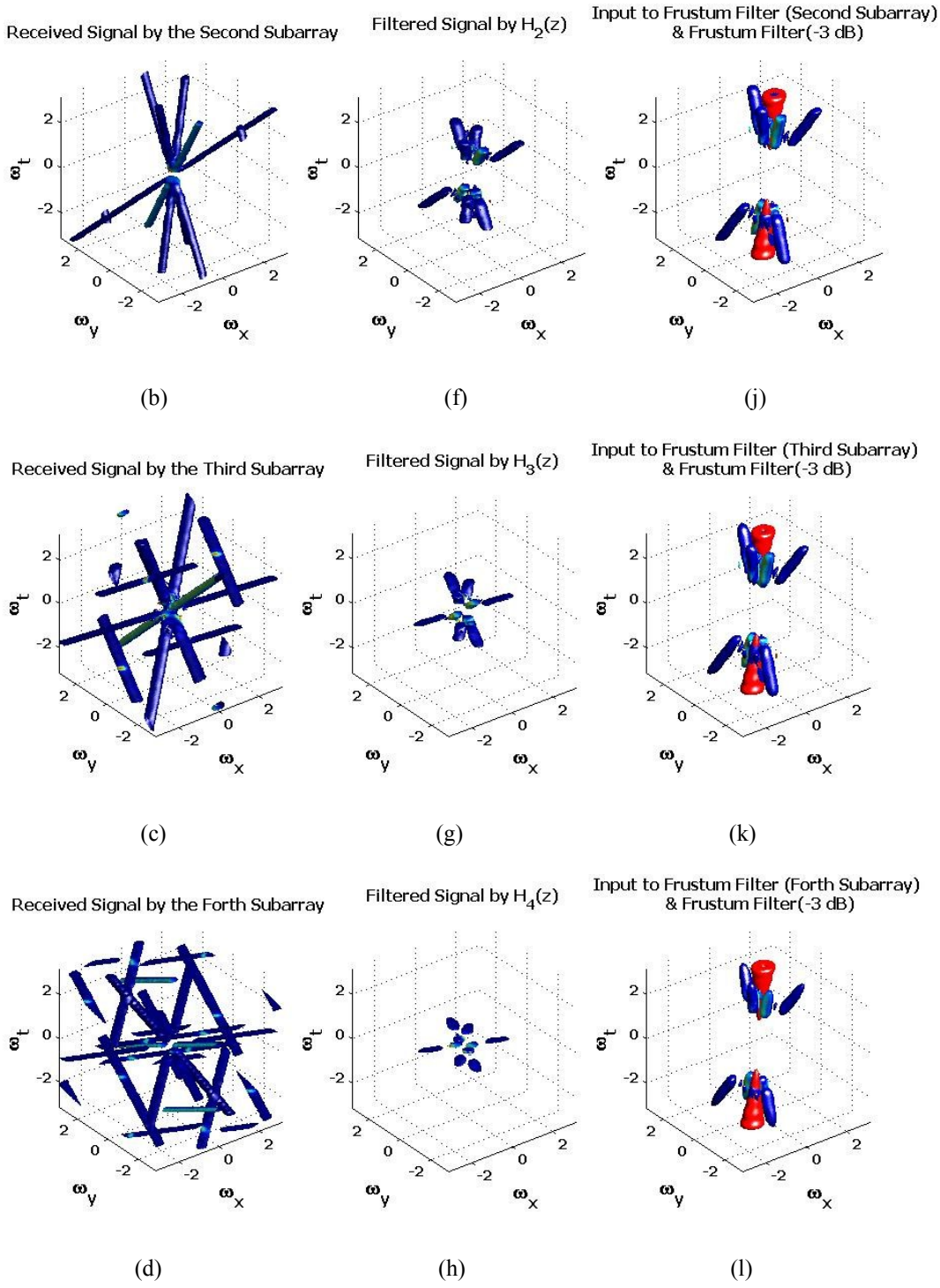

Figure 2.28. $\mathbf{f}_{D_\ell}$, $\hat{\mathbf{f}}_{D_\ell}$, $\bar{\mathbf{f}}_{D_\ell}$ (for $\ell = 1, 2, 3, 4$) and -3dB surface of hexagonal FIR frustum filter

Table 2.3. Five PWs propagating from different directions

	PW #1	PW #2	PW #3	PW #4	PW #5
θ^{o}	20	-5	-15	-35	35
φ^{o}	45	-45	90	135	75

2.10.2 Performance evaluation of NHA-FF and HA-FF

In this example the performance of the proposed beamformer (NHA-FF, Section 2.9) and the hexagonal frustum filter (HA-FF, Section 2.8) are evaluated in terms of beampattern and computational complexity. The effect of antenna coupling is being ignored here. Two different scenarios will be considered:

- The same number of sensors (721) for both NHA-FF and HA-FF are considered resulting in different aperture sizes as shown in Figure 2.29 (a) and (b).
- The same aperture size for both NHA-FF and HA-FF is considered resulting in different number of sensors as shown in Figure 2.29 (a) and (c).

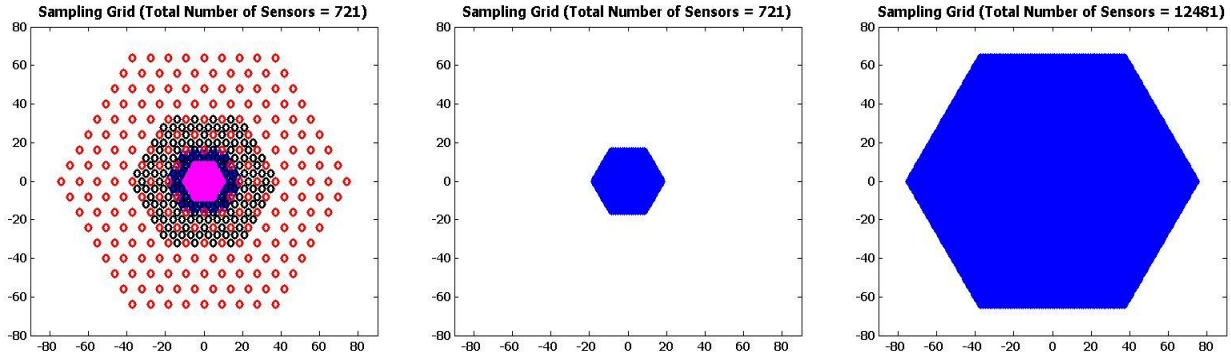

Figure 2.29. (a) NHA-FF with 721 sensors, (b) HA-FF with 721 sensors, (c) HA-FF with 12481 sensors

Evaluation of NHA-FF and HA-FF Beampatterns

All beamformers designed in this example are required to pass PWs propagating from $\theta_s = 20^o$ and $\varphi_s = 45^o$ having temporal intensity function equal to one from 0.1904 ($\omega_{\min}$) to 3.0464 ($\omega_{\max}$) and zero elsewhere. For the first scenario, the HA-FF was designed using Eq. (2.19), Eq. (2.20), and Eq. (2.21) with $N_t = 41$, $\alpha = 10^o$, $[\omega_{\min}\ \omega_{\max}]$ and $N_H = 31$ giving 721 total number of sensors. The NHA-FF has four subbands, i.e. $L = 4$. For all subbands the same frustum filter is being used. It has been designed using the same parameters as the one used for the HA-FF expect for N_H which was set to 17 for NHA-FF. This value for N_H results in the same total number of sensors (721) for both the NHA-FF and the HA-FF. In Figure 2.30 (a) and (b) the 3D beampatterns versus θ and temporal frequency for the NHA-FF and the HA-FF for the first scenario are shown. For another view, the same 2D beampatterns versus θ for both methods are shown in Figure 2.30 (d) and (e) from $\omega_{\min}$ to $\omega_{\max}$. It can be seen that for the same number of sensors, the performance of the NHA-FF is better than that of the HA-FF. This improvement achieved mainly because of the larger aperture size of the NHA-FF for low frequencies compared to that of the HA-FF (Figure 2.29 (a) and (b)).

For the second scenario, the same NHA-FF is used as in the first scenario. The HA-FF is designed with the same parameters as in the first scenario with the only difference of NH being equal to 129 leading to 12481 sensors and the same aperture as the NHA-FF. In Figure 2.30 (c), the 3D beampattern of the HA-FF versus θ and temporal frequency for the second scenario is shown. Further, the 2D beampattern versus θ from $\omega_{\min}$ to $\omega_{\max}$ for this case is shown in Figure 2.30 (f). Comparing these figures with Figure 2.30 (a) and (d), one can conclude that the

performance of the HA-FF is better than that of NHA-FF. However this comes at the cost of having almost 17.3 times greater number of sensors which increase the cost and computational complexity significantly.

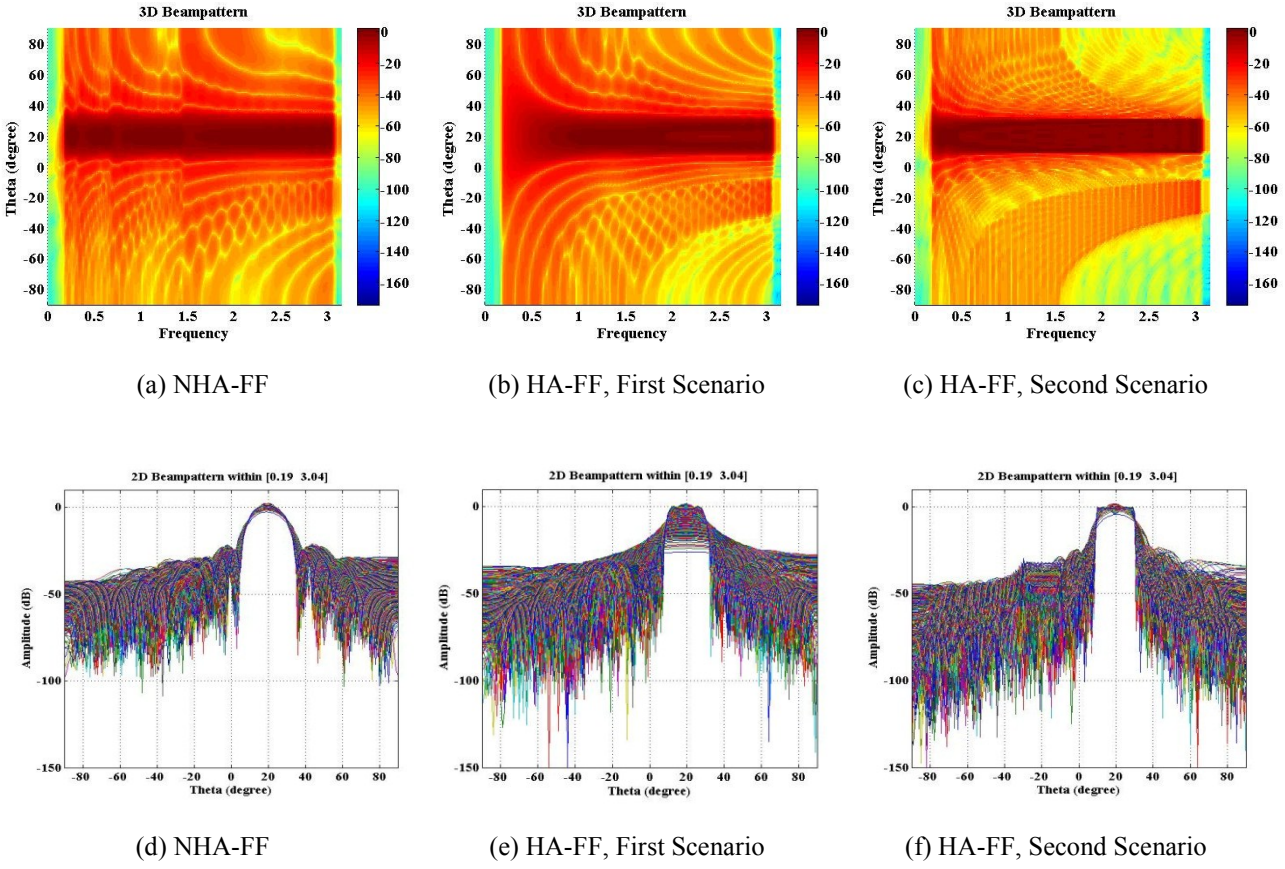

(a) NHA-FF (b) HA-FF, First Scenario (c) HA-FF, Second Scenario

(d) NHA-FF (e) HA-FF, First Scenario (f) HA-FF, Second Scenario

Figure 2.30. (a), (b), and (c) 3D beampatterns of NHA-FF and HA-FF, (d), (e), and (f) 2D beampatterns of NHA-FF and HA-FF

Evaluation of the Computational Complexity of NHA-FF and HA-FF

The computational complexity (CC), which is considered as the number of arithmetic operations (additions and multiplications) to compute N_s samples of the output for HA-FF (Section 2.8) and NHA-FF (Section 2.9), and modified NHA-FF (Section 2.9.2) is summarized in Table 2.4.

Table 2.4. Number of Arithmetic Operations for Each Method

	CC to form N_s output samples
HA-FF	$(2\hat{O}_{xy}O_t - 1)\times N_s$
NHA-FF	$[(2O_{xy}O_t - 1)A_1 + (O_{xy} + 1)(2N-1)L + (L-1)]\times N_s$
Modified NHA-FF	$[(2O_{xy}O_t - 1)A_1 + (O_{xy} + 1)(2NA_1 + A_2) + (L-1)]\times N_s$

$\hat{O}_{xy}$: Total number of sensors for HA-FF method

O_t : Temporal order of the HF-FF ($O_t = 2N_t + 1$, see Eq.(8))

O_{xy} : Number of sensors in each subarray for NHA-FF method

N : Order of analysis (synthesis) filters

L : Number of subarrays

$A_1 = \sum_{i=0}^{L-1}(0.5)^i = 2\left(1-(0.5)^L\right),\ A_2 = 2^L - 2L - 1$

The CC of HA-FF is straightforward. For NHA-FF, there are L separate frustum filters. If the sampling rate of the first subband is f_s, then the ℓ^{th} frustum filter is working with $f_s / 2^{\ell-1}$ as the sampling rate. This implies that the first term of CC of the NHA-FF is multiplied by A_1 rather than L. Given N as the length of analysis (synthesis) filters, $(2N-1)N_s$ arithmetic operations must be executed by each individual analysis (synthesis) filter to compute its output. Assuming that each subarray has O_{xy} sensors, each of which connected to an analysis filter, and each subband has one synthesis filter, follows that the filter bank for each subband entails $(O_{xy}+1)(2N-1)N_s$ arithmetic operations. Since the proposed beamformer is equipped with L subbands, the total computational cost due to the filter bank is multiplied by L (second term of CC of the NHA-FF). The final output of NHA-FF is formed as the summation of L subband outputs. Thus, $(L-1)N_s$ summations must be executed (last term of CC of the NHA-FF). For the

modified NHA-FF, the first and last terms of CC are the same as those for the NHA-FF. Due to the Nobel identity and polyphase structure, the second term would decrease significantly. The use of the Nobel identity in the ℓ^{th} subband, implies that instead of having an analysis filter with length N (Figure 2.27(a), top), there are $n_\ell = 2^{\ell-1}$ filters with length N/n_ℓ (Figure 2.27 (b)). The computation saving of the modified NHA-FF compared to NHA-FF comes from the fact that all filters in Figure 2.27 (b) are working with f_s/n_ℓ as the sampling rate rather than f_s in Figure 2.27 (a).

Table 2.4 shows that the CC of NHA-FF depends on both the frustum filter and filter bank orders, while the CC of HA-FF only depends on the frustum filter order. In Figure 2.31 (a) the CC of the modified NHA-FF and HA-FF is shown for L equal to 4, total number of sensors 721 (the first scenario), O_t equal to 81 and three different orders for N (21, 61, and 101). Also, to illustrate the improvement achieved by the modified NHA-FF, the CC of NHA-FF (Figure 2.26) is shown in Figure 2.31 (a) for $N = 101$. From Figure 2.31 (a), it can be seen that when N is large, CC of the modified NHA-FF is greater than that of HA-FF. However, the modified NHA-FF can be implemented as L separate sub-beamformers in parallel resulting in a much faster implementation than HA-FF. In Figure 2.31 (b) the CC of NHA-FF (just for N equal to 101), the modified NHA-FF, and HA-FF is shown for the second scenario (equal aperture area) with the same L, O_t, and N as before. It can be seen that in this case, even if N is large, the HA-FF requires much more computations than the other two.

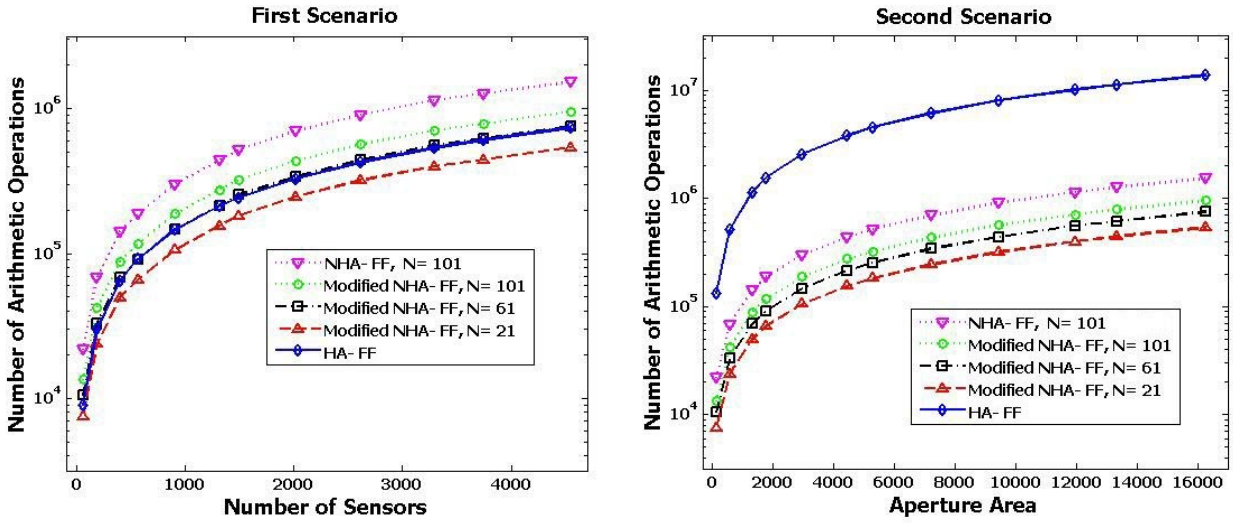

(a) (b)

Figure 2.31. CC for (a) First Scenario, (b) Second Scenario

2.11 Summary

The beamformer proposed in Section 2.5 consists of subband beamformers each one processing a special frequency octave of the received signal. Appropriate subsampling in space and time for each subarray leads to signals with the same region of support in the 2D frequency domain for all subarrays allowing the use of the same TF design for all subbands (Lemma 2.1). Through the simulations, it has been illustrated that when the number of sensors is given, the beampattern of the proposed method is almost frequency invariant, and if the aperture size is given, the proposed method can be implemented with significantly fewer sensors than ULA with a slight deterioration in performance. In summary, the advantage of using NAs is that the effective aperture for low temporal frequencies is larger than in the case of using ULA. This results in high spatial selectivity for low frequencies.

A broadband beamformer is proposed based on nested hexagonal arrays, hexagonal FIR frustum filters and, multirate techniques in Section 2.9. The nested hexagonal arrays used here consist of several hexagonal arrays in the x-y plane where the distance between elements in each subarray is two times larger than in the previous one. The use of hexagonal arrays was motivated from the fact that they are known to require a lower sensor density for alias free sampling than rectangular arrays. The proposed beamformer consists of subarray beamformers, each one using the signals obtained from one of the nested hexagonal arrays as the input. These signals are filtered and downsampled so that the ROS of the resulting 3D signals in the 3D frequency domain are the same for all subbands. The same hexagonal frustum filter design can therefore be used for all subarray beamformers to pass the desired signal and eliminate interferences. An efficient implementation of the proposed beamformer is also proposed based on eliminating redundant computations using the Nobel identity and polyphase structures. Examples in Section 2.10 illustrate that beamformers using nested hexagonal arrays have a larger effective aperture at low temporal frequencies and thus, better selectivity for low frequencies than beamformers using simple hexagonal arrays (Section 2.8). Further, for comparable selectivity the computational complexity of the hexagonal nested array beamformer is much lower that of a beamformer using a simple hexagonal array.

CHAPTER 3

A METHOD FOR FILTER BANK DESIGN USING OPTIMIZATION

3.1 Introduction

The broadband beamformer proposed in Chapter 2 requires a filter bank as shown in Figure 2.12 and Figure 2.26. One of the main requirements in filter bank design is Perfect Reconstruction (PR) which intuitively means that the signal doesn't get corrupted by the filter bank and the output is a delayed version of the input. Generally, filter banks can be categorized into two main groups: uniform filter bank in which all sampling rates, i.e. $\{n_1, n_2, ..., n_K\}$ in Figure 3.1, are equal and non-uniform filter bank in which at least one sampling rate is different from the others.

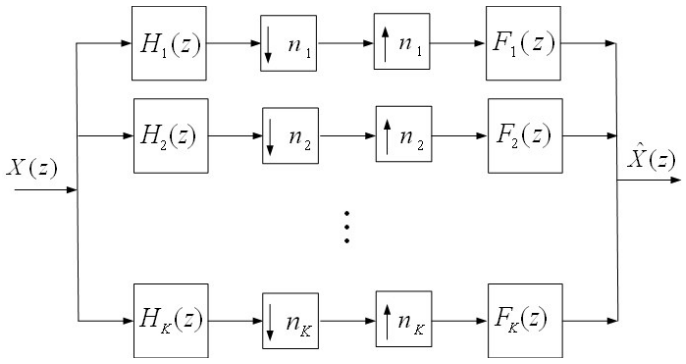

Figure 3.1. Filter Bank

A method to design filter banks using optimization is presented. The approach is based on formulating the design problem as an optimization problem with a performance index which consists of a term depending on PR conditions and a term depending on the magnitude response

of the analysis filters (MRAF). PR conditions for FIR analysis and synthesis filters are formulated as a set of linear equations using z-domain analysis and the MRAF are formulated as the square root of a quadratic function. The design objectives are to minimize the PR error and have the analysis filters satisfying some prescribed frequency specifications. The proposed method is applicable to uniform (including critically sampled and over sampled) and non-uniform filter banks (for sampling rates forming a compatible set as well as non-compatible set). Design examples illustrate the performance of the proposed method

The chapter is organized as follows: In Section 3.2 the necessary and sufficient conditions for PR are derived as a set of linear equations ($\mathbf{Ax}=\mathbf{b}$). Then, in Section 3.3 the filter bank design algorithm as an optimization problem is formulated. The performance of the proposed technique is illustrated using design examples in Section 3.4.

3.2 The Perfect Reconstruction Condition

Consider a filter bank as shown in Figure 3.1 with integer sampling rates $\{n_1, n_2, ..., n_K\}$. The output of the filter bank in the z-domain can be given by:

$$\begin{aligned}
\hat{X}(z) &= \sum_{k=1}^{K} \frac{1}{n_k} F_k(z) \sum_{\ell=0}^{n_k-1} X(z e^{-j\frac{2\pi\ell}{n_k}}) H_k(z e^{-j\frac{2\pi\ell}{n_k}}) \\
&= \sum_{k=1}^{K} \frac{1}{n_k} F_k(z) X(z) H_k(z) + \sum_{k=1}^{K} \frac{1}{n_k} F_k(z) \sum_{\ell=1}^{n_k-1} X(z e^{-j\frac{2\pi\ell}{n_k}}) H_k(z e^{-j\frac{2\pi\ell}{n_k}}) \\
&= X(z) T_0(z) + \sum_{\ell=1}^{n_k-1} X(z e^{-j\frac{2\pi\ell}{n_k}}) T_\ell(z)
\end{aligned} \tag{3.1}$$

where:

$$T_0(z) = \sum_{k=1}^{K} \frac{1}{n_k} F_k(z) H_k(z) \quad \text{and}$$
$$T_\ell(z) = \sum_{k=1}^{K} \frac{1}{n_k} F_k(z) H_k(z e^{-j\frac{2\pi\ell}{n_k}}) \quad for\ \ell = 1,\ldots,K \tag{3.2}$$

$T_0(z)$ and $T_\ell(z)$ ($\ell \neq 0$) are called overall distortion transfer function and aliasing transfer function corresponding to $X(z e^{-j2\pi\ell/n_k})$, respectively [56]. PR is achieved when $T_0(z)$ is a pure delay and $T_\ell(z)$ is zero. This leads to the following two necessary and sufficient conditions for PR:

1- Distortion Cancellation Condition:

$$\sum_{k=1}^{K} \frac{1}{n_k} F_k(z) H_k(z) = z^{-\Delta} \tag{3.3}$$

2- Aliasing Cancellation Condition:

$$\sum_{k=1}^{K} \frac{\alpha_{k,\ell}}{n_k} F_k(z) H_k(z e^{-j\frac{2\pi}{M}\ell}) = 0$$
$$for \quad \ell = 1,2,..,M-1 \tag{3.4}$$

where M is the least common multiple (LCM) between $n_1, n_2, \ldots, n_K$, and $\alpha_{k,\ell}$ (for $k = 1,2,\ldots,K$ and $\ell = 1,2,\ldots,M-1$) can be expressed as follows:

$$\alpha_{k,\ell} = \begin{cases} 1 & \text{if} \quad e^{j\frac{2\pi}{M}\ell} \in \{e^{j\frac{2\pi}{n_k}(1)}, e^{j\frac{2\pi}{n_k}(2)}, \ldots, e^{j\frac{2\pi}{n_k}(n_k-1)}\} \\ 0 & \text{otherwise} \end{cases} \tag{3.5}$$

Eq. (3.5) implies that when the aliasing term $H_k(ze^{-j\frac{2\pi}{M}\ell})$ does not appear in the k^{th} subband, $\alpha_{k,\ell}$ would be set to zero. As it is well known, the above two conditions imply that the output $\hat{X}(z)$ will be a delayed version (by Δ samples) of the input $X(z)$. When the analysis and synthesis filters ($H_k(z)$ and $F_k(z)$) are FIR filters, it is known from [54], [58], and [59] that these two necessary and sufficient conditions for PR can be formulated as a set of linear equations. A new formulation of such a set of linear equations will be shown in the following Lemma.

Lemma 3.1. The PR conditions, Eqs. (3.3) and (3.4), for FIR analysis and synthesis filters of the same length N can be formulated as (See Appendix D):

$$\mathbf{Ax} = \mathbf{b} \tag{3.6}$$

where:

$$\mathbf{A}_{M(2N-1)\times KN} = \begin{bmatrix} \beta_{1,0}\mathfrak{I}(\mathbf{h}_1) & \beta_{2,0}\mathfrak{I}(\mathbf{h}_2) & \cdots & \beta_{K,0}\mathfrak{I}(\mathbf{h}_K) \\ \beta_{1,1}\mathfrak{I}(\mathbf{h}_1 \otimes \mathbf{\Lambda}_1) & \beta_{2,1}\mathfrak{I}(\mathbf{h}_2 \otimes \mathbf{\Lambda}_1) & \cdots & \beta_{K,1}\mathfrak{I}(\mathbf{h}_K \otimes \mathbf{\Lambda}_1) \\ \beta_{1,2}\mathfrak{I}(\mathbf{h}_1 \otimes \mathbf{\Lambda}_2) & \beta_{2,2}\mathfrak{I}(\mathbf{h}_2 \otimes \mathbf{\Lambda}_2) & \cdots & \beta_{K,2}\mathfrak{I}(\mathbf{h}_K \otimes \mathbf{\Lambda}_2) \\ \vdots & \vdots & \ddots & \vdots \\ \beta_{1,M-1}\mathfrak{I}(\mathbf{h}_1 \otimes \mathbf{\Lambda}_{M-1}) & \beta_{2,M-1}\mathfrak{I}(\mathbf{h}_2 \otimes \mathbf{\Lambda}_{M-1}) & \cdots & \beta_{K,M-1}\mathfrak{I}(\mathbf{h}_K \otimes \mathbf{\Lambda}_{M-1}) \end{bmatrix} \tag{3.7}$$

with

$$\beta_{k,\ell} = \begin{cases} 1/n_k & \ell = 0 \\ \alpha_{k,\ell}/n_k & \ell \neq 0 \end{cases} \tag{3.8}$$

and the operator $\Im$ is defined as:

$$\Im([a_1\ a_2\ \ldots a_N]^T) = \begin{bmatrix} a_1 & 0 & 0 & \cdots & 0 \\ a_2 & a_1 & 0 & \cdots & 0 \\ a_3 & a_2 & a_1 & \cdots & 0 \\ \vdots & \vdots & \vdots & \ddots & \vdots \\ a_N & a_{N-1} & a_{N-2} & \cdots & a_1 \\ 0 & a_N & a_{N-1} & \cdots & a_2 \\ 0 & 0 & a_N & \cdots & a_3 \\ 0 & 0 & 0 & \ddots & \vdots \\ 0 & 0 & 0 & \cdots & a_N \end{bmatrix} \tag{3.9}$$

$\mathbf{h}_k$ $(k = 1,2,...,K)$ is a vector containing analysis filters' coefficients of k^{th} subband, i.e. $\mathbf{h}_k = [h_{k,0}, h_{k,1}, ..., h_{k,N-1}]^T$ where T is transpose operator. The operator $\otimes$ shows element-wise product, and $\mathbf{\Lambda}_i$ is defined as follows:

$$\mathbf{\Lambda}_i = [e^{j\frac{2\pi}{M}i(0)} \quad e^{j\frac{2\pi}{M}i(1)} \quad e^{j\frac{2\pi}{M}i(2)} \quad \cdots \quad e^{j\frac{2\pi}{M}i(N-1)}]^T \quad \text{for} \quad i = 1, \ldots, M-1 \tag{3.10}$$

$\mathbf{x}$ is a $KN \times 1$ vector containing synthesis filters' coefficients, i.e. $\mathbf{x} = [\mathbf{f}_1^T\ \mathbf{f}_2^T \cdots \mathbf{f}_K^T]^T$, $\mathbf{b}$ is a $M(2N-1) \times 1$ vector whose elements are all zero except the $\Delta + 1^{th}$ element which is 1.

The linear equation representing the PR conditions formulated in this lemma will be used for the filter bank design algorithm in the next section.

Remark: The PR condition presented in the above lemma is based on formulating the conditions in the z-domain while the approach used in [54] and [58] is based on the time-domain approach. Further, the PR condition presented here is formulated as one set of linear equations ($\mathbf{Ax} = \mathbf{b}$) rather than several linear equations ($\mathbf{A}_i\mathbf{x}_i = \mathbf{b}_i$) as is the case in [58]. As it will be discussed in the examples section, this can make a difference in the design of non-uniform filter banks while it has no significance for the design of uniform filter banks.

3.3 Filter Bank Design Algorithm

Filter banks are used to split a signal into a number of frequency subbands using analysis filters and then to process each subband separately. Thus the first requirement is to have analysis filters $H_k(z)$ satisfying some prescribed frequency specifications. The second condition is the requirement that the analysis and synthesis filters satisfy the PR condition.

The objective is to design a filter bank that achieves PR and MRAF satisfy some prescribed requirements. Here only the MRAF will be considered and the phase response of each individual analysis filter will be ignored to increase the degrees of freedom for a given length *N*. Each designed filter may not have a linear phase, but the PR conditions guarantee the linear phase of the whole filter bank. Before presenting the design procedure the following lemma is presented:

Lemma 3.2. The magnitude response of the k^{th} FIR analysis filter with coefficients $\mathbf{h}_k = [h_{k,0}, h_{k,1}, ..., h_{k,N-1}]^T$ at the frequency ω can be obtained as the square root of a quadratic function (See Appendix E):

$$\left|H_k(e^{j\omega})\right| = \left|\sum_{i=0}^{N-1} h_{k,i}\, e^{-j(i\omega)}\right| = \sqrt{\mathbf{h}_k^H \Re(\omega)\mathbf{h}_k} \tag{3.11}$$

where:

$$\Re(\omega) = \begin{bmatrix} 1 & \cos\omega & \cos 2\omega & \cdots & \cos(N-1)\omega \\ \cos\omega & 1 & \cos\omega & \cdots & \cos(N-2)\omega \\ \cos 2\omega & \cos\omega & 1 & \cdots & \cos(N-3)\omega \\ \vdots & \vdots & \vdots & \ddots & \vdots \\ \cos(N-1)\omega & \cos(N-2)\omega & \cos(N-3)\omega & \cdots & 1 \end{bmatrix}_{N\times N} \tag{3.12}$$

The design procedure requires finding the analysis and synthesis filters' coefficients ($\mathbf{h}_k$ and $\mathbf{f}_k$) so that the PR conditions in Eq. (3.6), Lemma 3.1, and the prescribed specifications for MRAF are satisfied. The design approach is based on minimizing the following performance index, combining PR error (e_{PR}) and magnitude response error (e_F), with respect to analysis filters' coefficients:

$$J = e_{PR} + e_F = w_{PR}\left\|\mathbf{Ax} - \mathbf{b}\right\|^2 + w_F \sum_{k=1}^{K} e_{F,k} \tag{3.13}$$

where $e_{F,K}$ is expressed using Lemma 3.2:

$$e_{F,k} = \sum_{i=1}^{\rho} \left\| \sqrt{\mathbf{h}_k^H \Re(\omega_i)\mathbf{h}_k} - \gamma_k(\omega_i) \right\|^2 \tag{3.14}$$

w_{PR} and w_F are optional weights, $\|\ \|$ is l_2-norm and $\gamma_k(\omega_i)$ is the desired magnitude response. The optimization parameters are the analysis filters' coefficients. The synthesis filters coefficients are obtained as the least square solution of Eq. (3.6). This design approach is similar to the one proposed by Nayebi et al. [54] and [58] with the differences being in the formulation

of the PR conditions and MRAF which is based on Lemmas 3.1 and 3.2. Further, in the method of [54] and [58] the length of all filters needs to be an integer multiple of M (LCM between $n_1, n_2, ..., n_K$). In the proposed method, there is no such restriction on the filter length. The proposed design algorithm is summarized below.

Given sampling rates $\{n_1, n_2, ..., n_K\}$, desired MRAF and length of filters N, Find analysis $\mathbf{h}_k$ and synthesis $\mathbf{f}_k$ filters' coefficients using the following algorithm:

Filter Bank Design Algorithm:

1- Choose ρ distinct sampling frequencies at ($\omega_1, \omega_2, ..., \omega_\rho$) and find $\Re(\omega_i)$ using Eq.(3.12) for $i = 1, 2, ..., \rho$.

2- Find initial designs for analysis filters using well-known techniques [91].

3- Form $\mathbf{A}$ using Eq.(3.7).

4- Find $\mathbf{x}$ as the least square solution of $\mathbf{Ax} = \mathbf{b}$.

5- Calculate the performance index J using Eq.(3.13).

6- If the performance index is less than a specified error, terminate the algorithm, otherwise update the analysis filters' coefficients by minimizing J, and go to step 3.

The initial designs in step 2 should be filters which almost satisfy the magnitude response specifications. The optimization in step 6 is an unconstrained nonlinear optimization problem for which the BFGS Quasi-Newton method [92] was employed.

3.4 Design Examples

The proposed approach can be applied for the design of any type of filter banks. Four examples are provided here to illustrate this:

1. Uniform filter bank with $K=2$, and sampling rates $n_1 = n_2 = 2$ (critically sampled)
2. Uniform filter bank with $K=4$, and sampling rates $n_1 = ... = n_4 = 3$ (oversampled)
3. Non-uniform filter bank with $K=3$ and a compatible sampling set : $n_1 = 2, n_2 = 4,$ and $n_3 = 4$.
4. Non-uniform filter bank with $K=5$ and a non-compatible sampling set: $n_1 = 1, n_2 = 2,$ $n_3 = 4, n_4 = 8,$ and $n_5 = 8$.

For all design examples, $\gamma_k(\omega_i)$ is defined as follows:

$$\gamma_k(\omega_i) = \begin{cases} 1 & \text{if } \omega_i \text{ is within the passband area of } H_k(e^{j\omega}) \\ 0 & \text{otherwise} \end{cases} \tag{3.15}$$

Example 1. Critically Sampled Uniform Filter Bank ($n_1 = n_2 = 2$)

When the filter bank is uniform, $\alpha_{k,\ell}$ in Eq. (3.5) is one for all k and ℓ consequently, $\beta_{k,\ell}$ in Eq. (3.7) is $1/n_k$ for all ℓ. The length of all filters is set to 36 ($N = 36$). The passband (stopband) and stopband (passband) cut-off frequencies for the first and second analysis filters

are equal to 0.4π and 0.6π respectively. The method of [54] for the design of a uniform filter bank was chosen for the comparison (due to similarities). The magnitude responses of the optimized analysis and synthesis filters are shown in Figure 3.2 (a) and (b). In Figure 3.2 (c) the aliasing error due to $H(-z)$, and distortion for both methods is presented. As it can be seen, the performance of both methods is close and very satisfactory.

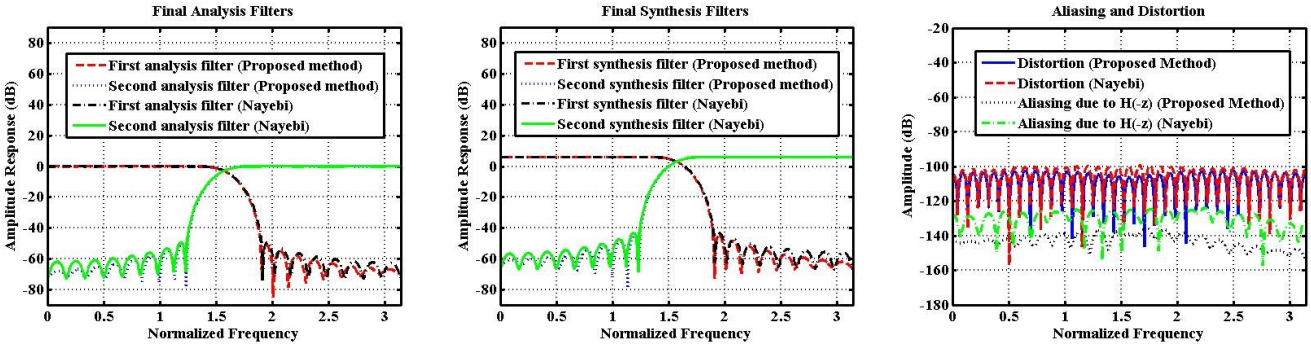

(a) Optimized Analysis Filters (b) Optimized Synthesis Filters (c) Aliasing and Distortion

Figure 3.2. Example 1 – Filter bank with {2,2} as the sampling set, designed by the proposed method and Nayebi [54]

Example 2. Oversampled Uniform Filter Bank ($n_1 = \cdots = n_4 = 3$)

The length of all filters was set to 40 ($N = 40$). The frequency specifications of analysis filters are summarized in Table 3.1. The magnitude responses of the optimized analysis filters are shown in Figure 3.3 (a). The corresponding synthesis filters have irregular magnitude responses and are shown in Figure 3.3 (b). Irregular synthesis filters are also reported in [93] for the case of oversampled uniform filter banks. Note that in many practical cases the frequency specifications of analysis filters are important and synthesis filters should only be adjusted so that the PR conditions are satisfied. Further, in Figure 3.3 (c) the aliasing error due to $H(e^{j\frac{2\pi}{3}}z)$ and $H(e^{j\frac{4\pi}{3}}z)$, and distortion are presented. As it can be seen, the error is very small.

Table 3.1. Frequency Specifications for the Second Design Example

	Type	Passband Cut-Off Frequency	Stopband Cut-Off Frequency
# 1	Lowpass	$0.15\,\pi$	$0.35\,\pi$
# 2	Bandpass	$0.35\,\pi$ and $0.4\,\pi$	$0.15\,\pi$ and $0.6\,\pi$
# 3	Bandpass	$0.6\,\pi$ and $0.65\,\pi$	$0.4\,\pi$ and $0.85\,\pi$
# 4	Highpass	$0.85\,\pi$	$0.65\,\pi$

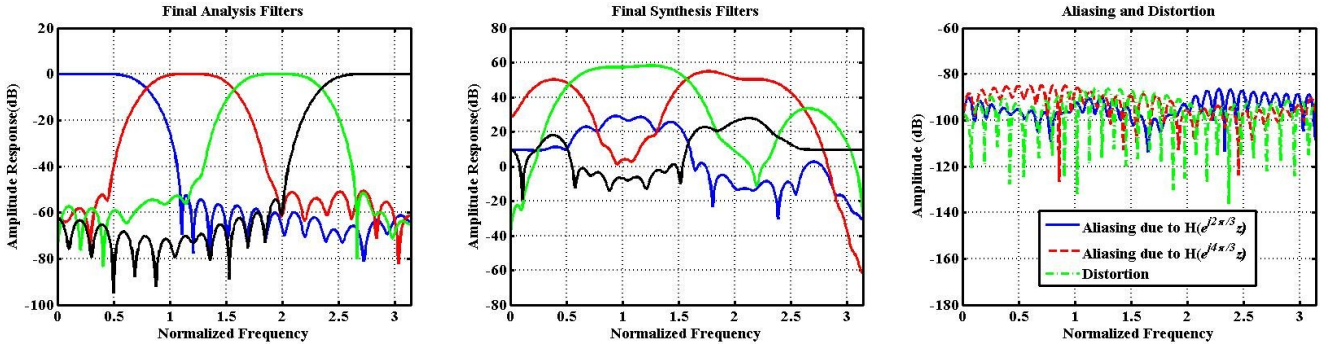

(a) Optimized Analysis Filters (b) Optimized Synthesis Filters (c) Aliasing and Distortion

Figure 3.3. Example 2 – Filter bank with {3,3,3,3} as the sampling set (over sampled)

Clearly the proposed method leads to satisfactory results for both uniform filter bank examples. For the design of such filter banks many effective techniques exist in the literature such as [48]- [54] and [93]- [96]. The purpose of including these two examples here is to show that the proposed method also works well for the uniform filter banks. The next two examples deal with the design of non-uniform filter banks which is more challenging.

Example 3. *Non-Uniform Filter Bank with a Compatible Sampling Set* ($n_1 = 2,\ n_2 = n_3 = 4$)

For this example LCM is 4, and $\mathbf{A}$ can be formed as follows:

$$\mathbf{A}=\begin{bmatrix} 0.5\,\mathfrak{I}(\mathbf{h}_1) & 0.25\,\mathfrak{I}(\mathbf{h}_2) & 0.25\,\mathfrak{I}(\mathbf{h}_2) \\ 0\,\mathfrak{I}(\mathbf{h}_1\otimes\mathbf{\Lambda}_1) & 0.25\,\mathfrak{I}(\mathbf{h}_2\otimes\mathbf{\Lambda}_1) & 0.25\,\mathfrak{I}(\mathbf{h}_3\otimes\mathbf{\Lambda}_1) \\ 0.5\,\mathfrak{I}(\mathbf{h}_1\otimes\mathbf{\Lambda}_2) & 0.25\,\mathfrak{I}(\mathbf{h}_2\otimes\mathbf{\Lambda}_2) & 0.25\,\mathfrak{I}(\mathbf{h}_3\otimes\mathbf{\Lambda}_2) \\ 0\,\mathfrak{I}(\mathbf{h}_1\otimes\mathbf{\Lambda}_3) & 0.25\,\mathfrak{I}(\mathbf{h}_2\otimes\mathbf{\Lambda}_3) & 0.25\,\mathfrak{I}(\mathbf{h}_3\otimes\mathbf{\Lambda}_3) \end{bmatrix} \tag{3.16}$$

Since the aliasing terms $H_1(ze^{-j\frac{2\pi}{4}})$ and $H_1(ze^{-j\frac{2\pi}{4}(3)})$ do not appear in the first subband ($n_1=2$), $\alpha_{1,1}$ and $\alpha_{1,3}$ were set to zero (Eq.(3.5)). The length of all filters was set to 64. In this case, the proposed method is compared with Nayebi's et al. design method [58], and the method of [60]. The filters' frequency specifications are similar to the one reported in [60], i.e. the transition bands are set to 0.25636, 0.3214, and 0.32099 (normalized frequencies). The magnitude responses of the optimized analysis and synthesis filters for the proposed and Nayebi's et al. method are shown in Figure 3.4 (a). Also, Figure 3.4 (b) presents aliasing due to $H(-z)$, $H(jz)$, and $H(-jz)$ along with the distortion for both methods. As can be seen, their performance is close and very satisfactory. For the proposed method, the maximum passband ripples of converged analysis filters are -67.31, -63.70, -75.10 dB and the minimum stopband attenuations are -59.19, -67.65, -78.36 dB. Comparing these results with Figure 1 and Figure 2 in [60], one can conclude that the proposed method results in better performance in terms of aliasing and distortion, while the method of [60] results in better frequency specifications (less maximum passband ripples and minimum stopband attenuations).

Example 4. Non-Uniform Filter Bank with a Non-Compatible Sampling Set ($n_1=1, n_2=2, n_3=4, n_4=n_5=8$)

This filter bank design is motivated by an application in broadband beamforming as discussed in Chapter 3. The filter bank in [28], was designed with the PR condition relaxed. To

implement this special filter bank, a tree structure was used in [97] which lead to degradation at the edges where difference octaves meet. In [31] an equalizer was added to the filter bank to better approximate the PR which is not the optimal solution in terms of performance and further increases the implementation cost and delay. A filter bank satisfying the specifications in Table 3.2 will be designed with the method proposed here. In this case the LCM is 8 and the matrix **A** becomes as follows:

$$\mathbf{A} = \begin{bmatrix} \Im(\mathbf{h}_1) & 0.5\,\Im(\mathbf{h}_2) & 0.25\Im(\mathbf{h}_3) & 0.125\Im(\mathbf{h}_4) & 0.125\Im(\mathbf{h}_5) \\ 0\Im(\mathbf{h}_1 \otimes \mathbf{\Lambda}_1) & 0\,\Im(\mathbf{h}_2 \otimes \mathbf{\Lambda}_1) & 0\,\Im(\mathbf{h}_3 \otimes \mathbf{\Lambda}_1) & 0.125\,\Im(\mathbf{h}_4 \otimes \mathbf{\Lambda}_1) & 0.125\,\Im(\mathbf{h}_5 \otimes \mathbf{\Lambda}_1) \\ 0\Im(\mathbf{h}_1 \otimes \mathbf{\Lambda}_2) & 0\Im(\mathbf{h}_2 \otimes \mathbf{\Lambda}_2) & 0.25\Im(\mathbf{h}_3 \otimes \mathbf{\Lambda}_2) & 0.125\,\Im(\mathbf{h}_4 \otimes \mathbf{\Lambda}_2) & 0.125\,\Im(\mathbf{h}_5 \otimes \mathbf{\Lambda}_2) \\ 0\Im(\mathbf{h}_1 \otimes \mathbf{\Lambda}_3) & 0\Im(\mathbf{h}_2 \otimes \mathbf{\Lambda}_3) & 0\,\Im(\mathbf{h}_3 \otimes \mathbf{\Lambda}_3) & 0.125\,\Im(\mathbf{h}_4 \otimes \mathbf{\Lambda}_3) & 0.125\,\Im(\mathbf{h}_5 \otimes \mathbf{\Lambda}_3) \\ 0\Im(\mathbf{h}_1 \otimes \mathbf{\Lambda}_4) & 0.5\,\Im(\mathbf{h}_2 \otimes \mathbf{\Lambda}_4) & 0.25\Im(\mathbf{h}_3 \otimes \mathbf{\Lambda}_4) & 0.125\,\Im(\mathbf{h}_4 \otimes \mathbf{\Lambda}_4) & 0.125\,\Im(\mathbf{h}_5 \otimes \mathbf{\Lambda}_4) \\ 0\Im(\mathbf{h}_1 \otimes \mathbf{\Lambda}_5) & 0\Im(\mathbf{h}_2 \otimes \mathbf{\Lambda}_5) & 0\,\Im(\mathbf{h}_3 \otimes \mathbf{\Lambda}_5) & 0.125\,\Im(\mathbf{h}_4 \otimes \mathbf{\Lambda}_5) & 0.125\,\Im(\mathbf{h}_5 \otimes \mathbf{\Lambda}_5) \\ 0\Im(\mathbf{h}_1 \otimes \mathbf{\Lambda}_6) & 0\Im(\mathbf{h}_2 \otimes \mathbf{\Lambda}_6) & 0.25\Im(\mathbf{h}_3 \otimes \mathbf{\Lambda}_6) & 0.125\,\Im(\mathbf{h}_4 \otimes \mathbf{\Lambda}_6) & 0.125\,\Im(\mathbf{h}_5 \otimes \mathbf{\Lambda}_6) \\ 0\Im(\mathbf{h}_1 \otimes \mathbf{\Lambda}_7) & 0\Im(\mathbf{h}_2 \otimes \mathbf{\Lambda}_7) & 0\Im(\mathbf{h}_3 \otimes \mathbf{\Lambda}_7) & 0.125\,\Im(\mathbf{h}_4 \otimes \mathbf{\Lambda}_7) & 0.125\,\Im(\mathbf{h}_5 \otimes \mathbf{\Lambda}_7) \end{bmatrix} \tag{3.17}$$

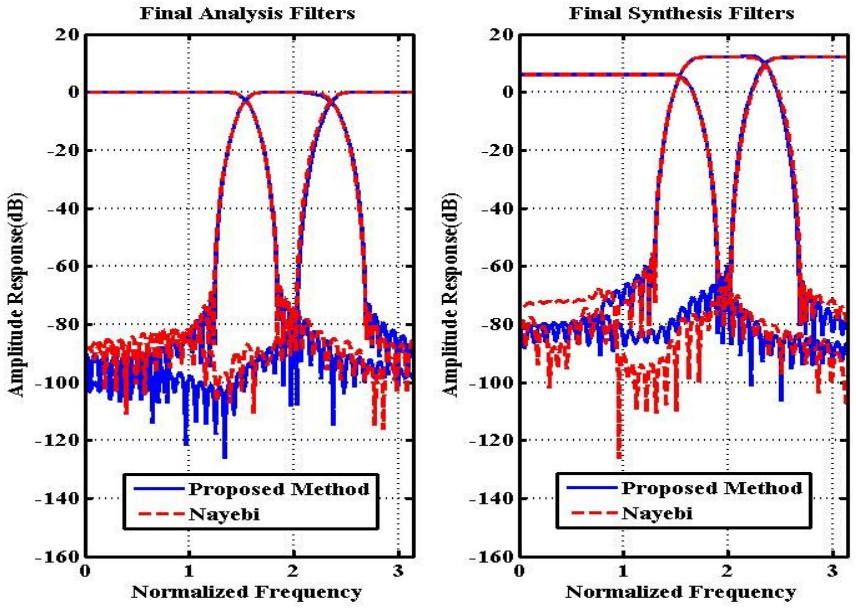

(a) Optimized Analysis and Synthesis Filters

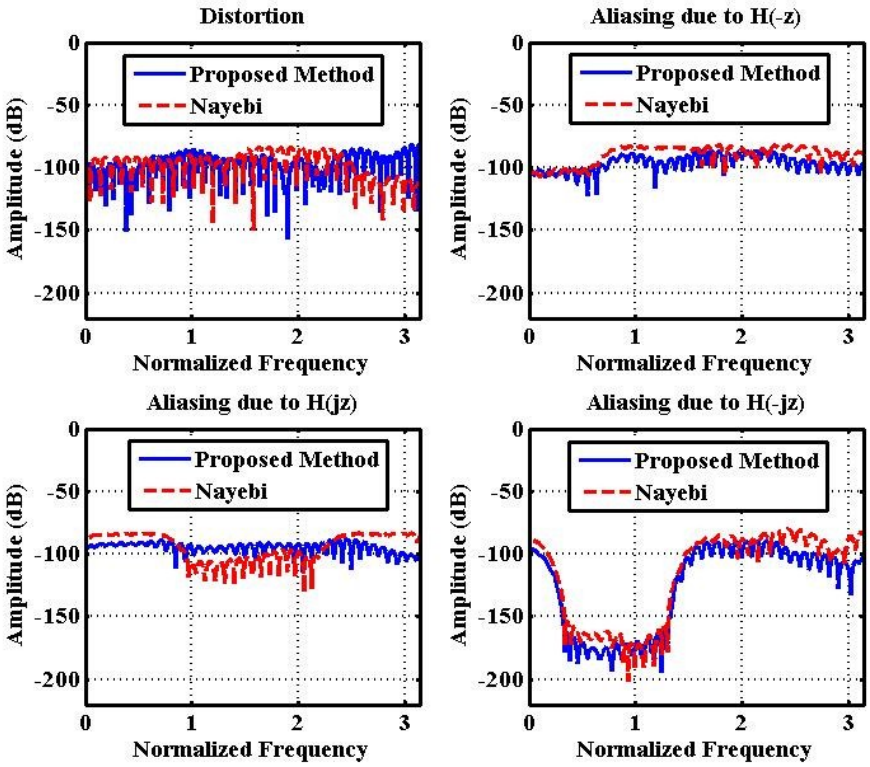

(b) Aliasing and Distortion

Figure 3.4. Example 3 – Filter bank with {2,4,4} as the sampling set, designed by the proposed method and Nayebi [58]

The length of all filters is set to 60. Figure 3.5 (a) presents distortion and aliasing components. The magnitude responses of the optimized analysis filters are shown in Figure 3.5 (b). The frequency responses of the resulting synthesis filters are irregular, but as long as (almost) PR is achieved this is not a concern for this application. It is interesting to note that for this example the method of [58] leads to 8 sets of linear equation systems which do not converge to a satisfactory solution.

Table 3.2. Frequency Specifications for the Fourth Design Example

	Type	**Passband Cut-Off Frequency**	**Stopband Cut-Off Frequency**
# 1	Highpass	0.525 π	0.475 π
# 2	Bandpass	0.275 π and 0.475 π	0.225 π and 0.525 π
# 3	Bandpass	0.15 π and 0.225 π	0.1 π and 0.275 π
# 4	Bandpass	0.0875 π and 0.1 π	0.0125 π and 0.15 π
# 5	Lowpass	0.0125 π	0.0625 π

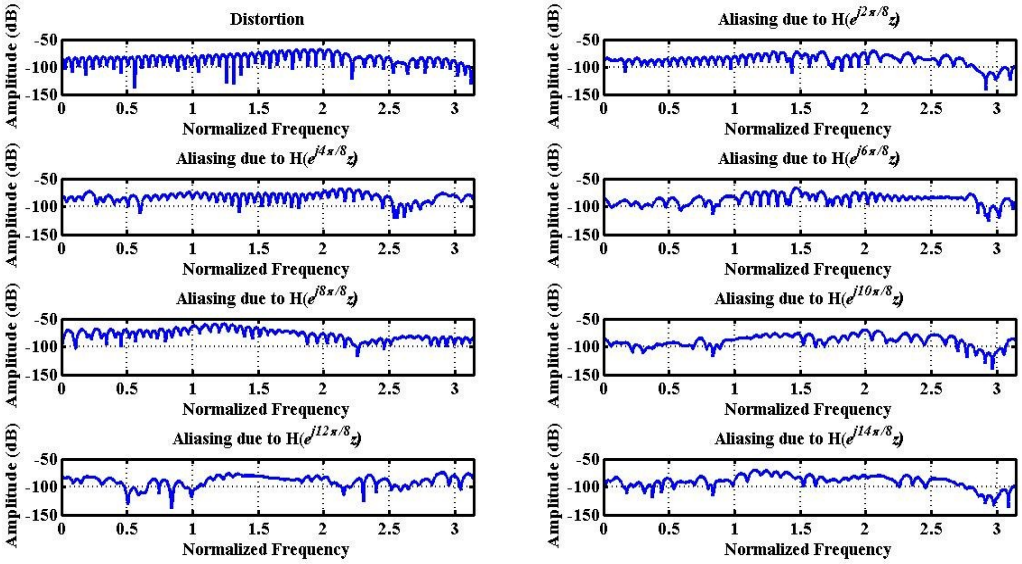

(a) Aliasing and Distortion

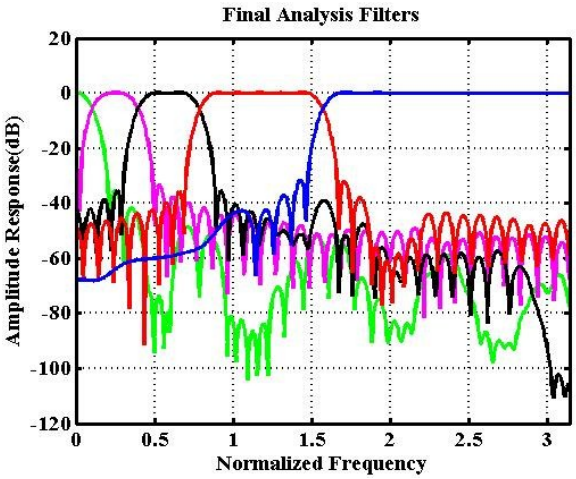

(b) Optimized Analysis Filters

Figure 3.5. Example 4 – Filter bank with {1,2,4,8,8} as the sampling set, designed by the proposed method

The above examples illustrate that the proposed method leads to satisfactory results for uniform as well as for non-uniform filter banks in both cases with a compatible sampling set as well as with a non-compatible sampling set. It is worth mentioning that for non-uniform filter banks with non-compatible sampling sets, there are cases where PR cannot be achieved due to in-band aliasing [61]. In such cases the proposed method minimizes the aliasing and distortion errors to achieve almost PR. An alternative is to use the approach in [62] and [63] where linear dual rate systems are used to obtain PR.

3.5 Summary

A method to design filter banks using optimization was presented. The approach is based on formulating the design problem as an optimization problem with a performance index which consists of a term depending on perfect reconstruction and a term depending on the magnitude specifications of the analysis filters. Perfect reconstruction for FIR analysis and synthesis filters is based on a new formulation as a set of linear equations using z-domain analysis. Further, the error in the analysis filter magnitude specifications is evaluated using a quadratic form. The design objectives are to achieve almost perfect reconstruction and have the analysis filters satisfying some prescribed frequency specifications. Results indicate that the proposed method gives results comparable with existing techniques for uniform (including critically sampled and over sampled) filter banks. For the case of non-uniform filter banks with non-compatible sampling sets the proposed method gives satisfactory results for cases where existing methods do not work.

CHAPTER 4

A MULTI-STAGE SPACE-TIME EQUALIZER FOR BLIND SOURCE SEPARATION

4.1 Introduction

In this chapter, a blind source separation approach is proposed using array signal processing for narrowband PWs. Neither the DOA nor a training sequence is assumed to be available for the receiver. The only assumption is that the transmitted signal satisfies the constant modulus property which is valid for many modulation schemes, and can be exploited by the multi-modulus algorithm. Each stage, which consists of beamformer, a DOA estimator and an equalizer, tries to jointly combat multi-user interference and the effect of the fading channel between each source and the antenna. An adaptive version of the basic structure of GSC [6], called adaptive GSC (AGSC) is presented which can adaptively track a user and strongly attenuate other users with different DOAs. The possibly time-varying DOA for each user is estimated using the phase shift between the outputs of two subarray beamformers at each stage. The estimated DOAs are used to improve multi-user interference rejection and to compute the input to the next stage. In order to significantly alleviate inter-stage error propagation and provide a fast convergence, a mean-square-error sorting algorithm is proposed which assigns detected sources to different stages according to the reconstruction error at different stages. Further, to speed up the convergence, a simple-yet-efficient DOA estimation algorithm is proposed which can provide good initial DOAs for the multi-stage STE. Simulation results

illustrate the performance of the proposed STE and show that it can be deal with changing DOAs and time variant channels.

This chapter is organized as follows: In Section 4.2, the problem description will be presented. The proposed multi-stage STE will be discussed in Section 4.3. To speed up the convergence of the proposed STE, two algorithms will be suggested in Section 4.4. Section 4.5 summarizes the implementation steps discussed in Section 4.3 and 4.4. The performance of the proposed method will be illustrated in Section 4.6 using simulations.

The mathematical notation used in this chapter is as follows: Bold letters represent matrix or vectors, and regular letters indicate a scalar value. T and H represent transpose and conjugate transpose, respectively. The index n shows the parameter values at n^{th} sample. $\mathrm{Re}\{\}$ and $\mathrm{Im}\{\}$ denotes the real and imaginary parts respectively. Also, $E\{\}$ represents the expected value.

4.2 Problem Description

Q uncorrelated and narrowband sources with the common wavelength (λ) are being transmitted to the base station by different users with distinct, possibly time-varying, DOAs through time-varying fading and noisy channels. The goal here is to separate all sources and recover the original data transmitted by each one of them in a blind manner. The only assumption is that the transmitted signals satisfy the constant modulus property. DOAs are not known and there are no pilot signals.

Consider an *M*-element uniform linear array with half wavelength space $\lambda/2$ between elements at the base station and Q users transmitting data ($s_q(n)$, for $q=1,2,...,Q$) to the base station. The users' DOAs to the antenna are denoted by $\theta_1,\theta_2,\ldots,\theta_Q$ which might be time-varying due to the user movement. The transmitted signal from each user is distorted by a fading channel which might be time-varying due to changes in the channel. After sampling, the baseband received signal at the antenna is given by:

$$\mathbf{X}_1(n)=[x_1(n) \quad x_2(n) \quad ... \quad x_M(n)]^T=\sum_{q=1}^{Q} t_q(n)\mathbf{V}_q(n)+\vartheta(n) \tag{4.1}$$

where $t_q(n)$, the signal received at the antennas from each user, is as follows:

$$\begin{aligned} &t_q(n)=\mathbf{h}_q^T(n)\ \mathbf{s}_q(n)\\ &\mathbf{s}_q(n)=[s_q(n),\ s_q(n-1),\ \ldots,\ s_q(n-(L-1))]^{\ T}\\ &\mathbf{h}_q(n)=[h_{q,1}(n),\ h_{q,2}(n),\ \ldots,\ h_{q,L}(n)]^{\ T} \end{aligned} \tag{4.2}$$

with $\mathbf{h}_q^T(n)$ representing a fading channel and L is the maximum length of all channels. Further, $\vartheta(n)$ is the white Gaussian noise and $\mathbf{V}_q(n)$ is the array manifold vector [1] given by:

$$\mathbf{V}_q(n)=[1 \quad e^{-j\pi\sin(\theta_q(n))} \quad e^{-j2\pi\sin(\theta_q(n))} \quad ... \quad e^{-j(M-1)\pi\sin(\theta_q(n))}]^T \tag{4.3}$$

In the above model, CCI and temporal ISI are considered and it is assumed that spatial ISI, which can be considered as the case when sources are correlated [98], is not present. The goal here, as mentioned before, is to recover the original data transmitted by each user and accurately estimate the DOA of all users.

4.3 The proposed Multi-Stage Space-Time Equalizer

To deal with the problem formulated in the previous section, a multi-stage STE as shown in Figure 4.1 is proposed. The STE consists of an antenna with M elements, Q stages, one for each one of the Q users, and a sorting algorithm which is based on mean square error (MSE). The structure of all stages is the same, and therefore just the first stage is shown in Figure 4.2. Each stage consists of three main parts: beamformer, DOA estimator, and equalizer including DFE and a channel estimator.

The beamformer at each stage locks on one of the users and attenuate the others. Based on the basic structure of the GSC [6], an adaptive beamforming scheme called Adaptive GSC (AGSC) is used which consists of two adaptive branches denoted as the top ($\mathbf{W_q}(n)$ in Figure 4.2) and bottom ($\mathbf{B}(n)$ and $\mathbf{W_a}(n)$ in Figure 4.2) branches. The main objective for the top branch is to capture and track one of the sources with possibly time-varying DOAs. The bottom branch consists of an adaptive blocking matrix ($\mathbf{B}(n)$) and an adaptive CCI weight canceller ($\mathbf{W_a}(n)$), and its main objective is strong CCI cancelation. The function of the blocking matrix is to adaptively eliminate the signal of the captured source from the bottom branch. Then, the CCI weight canceller tries to minimize the energy of the signal passed through the bottom branch (which is ideally pure CCI and noise) by placing nulls in the array response at the DOAs of CCIs. To recover the data transmitted by the users, the effect of fading in the channels between the detected user and the base station will be compensated using an equalizer

in each stage. The equalization scheme includes a DFE and a channel estimator and is similar to the one proposed in [69]. The channel estimator can improve the performance in terms of both ISI and CCI cancellation [69]. The beamformer and equalizer are updated in a combined manner. A joint MMA-based scheme is used to update both $\mathbf{W_q}(n)$ and the feedforward filter of the DFE ($\mathbf{W_f}(n)$) as proposed in [80]. Similarly, the CCI weight canceller and channel estimator are jointly updated using the performance index proposed in [69] leading to fast convergence.

The DOA of a user can be estimated using subarray beamformers [68]. The first subarray beamformer is receiving input from the top *M*-1 antenna elements and the second one from the *M*-1 bottom elements. The DOA of the corresponding user is a function of the phase shift between the outputs of the two subarrays beamformers. A phase tracking algorithm is implemented to estimate and track the possibly time-varying DOA of the captured signal. The estimated DOA is deployed to update the blocking matrix of AGSC and to form the input to the next stages. The input signal to the next stage will be formed by eliminating the detected user from the current input.

The MSE-based sorting algorithm assigns detected sources to different stages according to the reconstruction error (MSE) at different stages. Intuitively, the algorithm tries to keep the sources with small reconstruction error at early stages and push the sources with large error to the last stages. This arrangement significantly alleviates inter-stage error propagation and speed up the convergence. In the rest of this section the function of each part of a stage will be described.

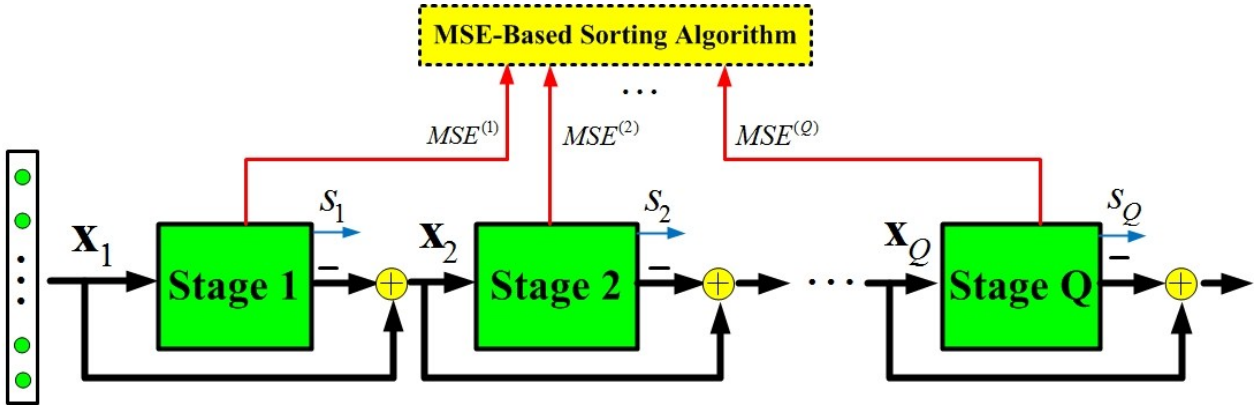

Figure 4.1. Structure of the proposed multi-stage STE

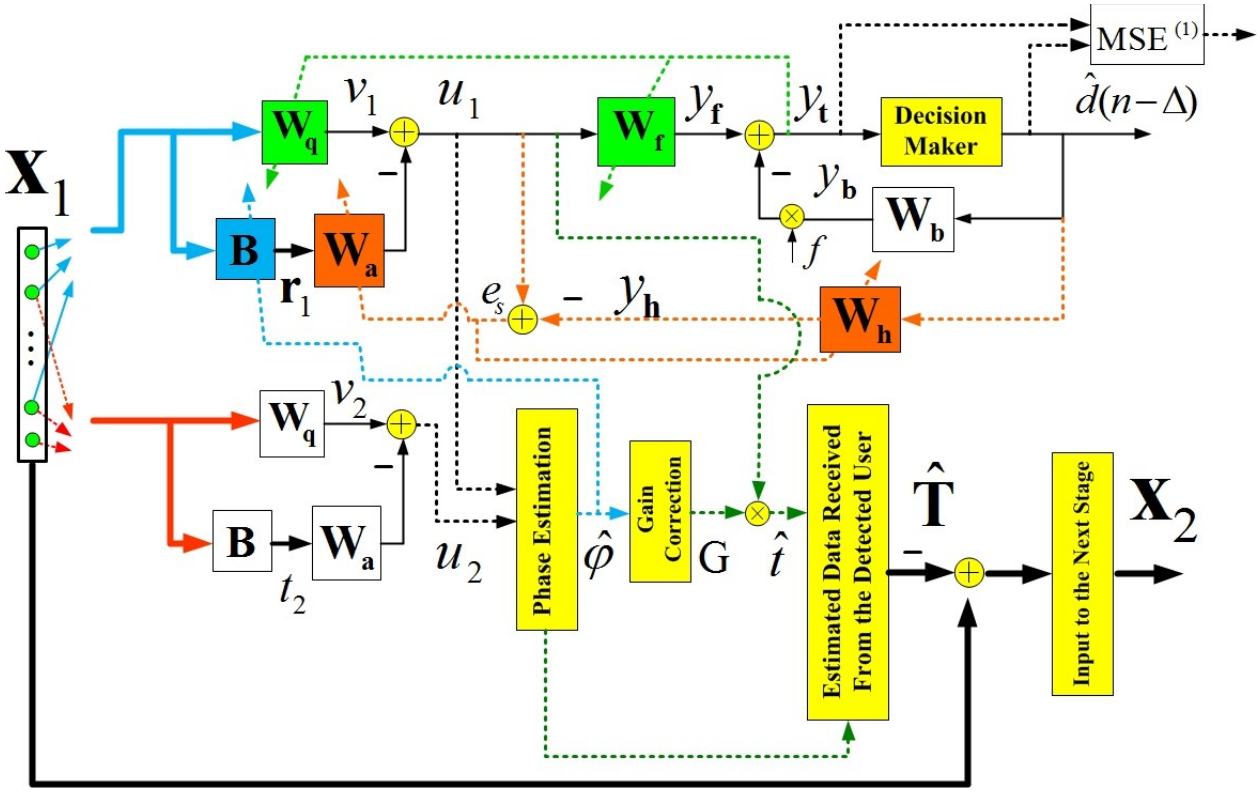

Figure 4.2. The first stage of the proposed STE in Figure 4.1

4.3.1 Beamformer: Adaptive Generalized Sidelobe Canceller

The beamformer used at each stage is based on the GSC structure. Since the DOA of the user is assumed not known a priori, or it may change due to user movement, the standard GSC cannot be used here. Instead an adaptive version of the GSC called AGSC, with all the components ($\mathbf{W_q}(n)$, $\mathbf{B}(n)$, and $\mathbf{W_a}(n)$) getting adaptively updated, is being used here.

The objective for $\mathbf{W_q}(n)$, a vector of length M-1, is to lock into one of the users, and its updating rule is based on the MMA [82]. The cost function for MMA is given by:

$$CF_{MMA} = E\left\{\left[\left(\mathrm{Re}\{y_t(n)\}\right)^L - R^L\right]^2 + \left[\left(\mathrm{Im}\{y_t(n)\}\right)^L - R^L\right]^2\right\} \tag{4.4}$$

where R^L is constant determined by the available statistics of modulation scheme. As was proposed in [82], $L = 2$ provides a good compromise between performance and implementation complexity. Taking advantage of the stochastic gradient algorithm [92] and MMA, the updating equation for $\mathbf{W_q}(n)$ is given by ($\mu_\mathbf{q}$ is the learning step size):

$$\mathbf{W_q}(n+1) = \mathbf{W_q}(n) - \mu_\mathbf{q}\, \widetilde{\mathbf{X}}_1(n)\, e^*_{MMA}(n) \tag{4.5}$$

where

$$\widetilde{\mathbf{X}}_1(n) = [x_1(n),\ x_2(n),\ \ldots,\ x_{M-1}(n)]^T$$

$$e_{MMA}(n) = (\mathrm{Re}\{y_t(n)\})^3 + i(\mathrm{Im}\{y_t(n)\})^3 - R^2\, y_t(n)$$

The role of the $(M\text{-}1)\times(M\text{-}2)$ matrix $\mathbf{B}(n)$ can be intuitively described as blocking the signal from the desired user in the lower branch of the beamformer (desired user at each stage means the user which has been detected by $\mathbf{W_q}(n)$). The updating of $\mathbf{B}(n)$ is based on the estimated phase difference between the outputs of two subarray beamformers $\hat{\varphi}(n)$ which will be discussed in the DOA estimation section (4.3.2). Given the phase difference $\hat{\varphi}(n)$, $\mathbf{B}(n)$ can be updated by first forming the following $(M-1)\times 1$ vector:

$$\widetilde{\mathbf{V}}(n) = [1 \quad e^{-j\hat{\varphi}(n)} \quad \ldots \quad e^{-j(M-2)\hat{\varphi}(n)}]^T \tag{4.6}$$

Then, using singular value decomposition (SVD), $\widetilde{\mathbf{V}}(n)$ can be expressed as:

$$\widetilde{\mathbf{V}}_k(n) = \hat{U}\,\hat{S}\,\hat{V}^H \tag{4.7}$$

where $\hat{U}$ and $\hat{V}$ are unitary matrices, and $\hat{S}$ is a diagonal matrix. $\mathbf{B}(n)$ can be formed by deleting the first column of the $(M\text{-}1)\times(M\text{-}1)$ matrix $\hat{U}$.

In conventional GSCs, the effect of $\mathbf{W_a}(n)$ is to increase CCI and noise cancellation, and it is usually implemented using the least-mean-square (LMS) approach. LMS-based GSC is simple but converges very slowly. This is due to the fact that the conventional GSC algorithm uses $u_1(n)$ (see Figure 4.2) as the error which includes the desired signal. In such a case, the error has large amplitude and to guarantee the algorithm's stability, the learning step size must be very small which makes the convergence very slow. According to [69], using $e_s(n)$ (see Figure 4.2) rather than $u_1(n)$ can speed up the convergence. This stems from the fact that at steady state

$e_s(n)$ does not include the desired signal and therefore has smaller value compared to $u_1(n)$. Thus, the learning step size for the updating algorithm can be larger which makes the convergence faster. Accordingly, in order to update the $(M\text{-}2)\times 1$ vector $\mathbf{W_a}(n)$, the following cost function is minimized [69]:

$$\begin{aligned} CF_{\mathbf{W_a}} &= E\{|\, e_s(n)\,|^2\} \\ e_s(n) &= u_1(n-\Delta-1) - \mathbf{W_h}(n)^H \widetilde{\mathbf{D}}_1(n) \end{aligned} \tag{4.8}$$

where

$$\widetilde{\mathbf{D}}_1(n) = [\hat{d}_1(n-\Delta-1),\ \hat{d}_1(n-\Delta-2),\ \ldots,\ \hat{d}_1(n-\Delta-\ell_2)]^T$$

and ℓ_2 is the length of $\mathbf{W_h}(n)$. Using the LMS algorithm, the updating equation for $\mathbf{W_a}(n)$ is given by:

$$\begin{aligned} \mathbf{W_a}(n+1) &= \mathbf{W_a}(n) + \mu_{\mathbf{a}}\, \mathbf{r}(n)\, e_s^*(n) \\ \mathbf{r}(n) &= \mathbf{B}(n)^H \widetilde{\mathbf{X}}_1(n) \end{aligned} \tag{4.9}$$

where $\mu_{\mathbf{a}}$ is the step size and $\widetilde{\mathbf{X}}_1(n)$ is given by Eq.(4.5).

4.3.2 DOA Estimation

The approach used here is based on the method proposed in [68] for DOA estimation in the presence of pilot signals. Although no pilot signals are available here, the basic idea of the approach in [68] is to use the phase difference between the output signals of two subarray beamformers. Given an array of *M* elements, the first subarray is formed using the top *M* -1 elements while the second subarray is formed using the bottom *M* -1 ones. The signals from

these two subarrays are fed to two identical beamformers. It was shown in [68] that the phase difference $\hat{\varphi}$ between the output signals of the two beamformers is a function of DOA $\hat{\theta}$ given by:

$$\hat{\theta}(n) = \arcsin(\hat{\varphi}(n)/\pi) \tag{4.10}$$

In the proposed STE, the input signals ($M \times 1$ vector) at each stage are used to form the two subarrays with M -1 elements each feeding into two subarray beamformers which have the same coefficient values, $\mathbf{W_q}(n), \mathbf{B}(n)$, and $\mathbf{W_a}(n)$ as shown in Figure 4.2. Thus, when the top beamformer locks into one of the users, the bottom beamformer also locks into the same user. Using the outputs of these two subarray beamformers, the DOA of a detected user $\hat{\theta}_q(n)$ can be estimated as a function of the phase difference $\hat{\varphi}(n)$ between $u_1(n)$ and $u_2(n)$ in Figure 4.2.

In order to estimate and track the phase difference between $u_1(n)$ and $u_2(n)$, the second order phase tracking loop algorithm [81] is used (μ_φ is learning step size, and τ is a positive constant):

$$\begin{aligned}
&\hat{u}_1(n) = u_2(n)\, e^{j\hat{\varphi}(n)} \\
&e_\varphi(n) = \mathrm{Im}\{\, \hat{u}_1(n)[\hat{u}_1(n) - u_1(n)]^* \,\} \\
&\hat{\varphi}(n+1) = \hat{\varphi}(n) + \mu_\varphi[e_\varphi(n) + \tau \sum_{i=1}^{n} e_\varphi(i)]
\end{aligned} \tag{4.11}$$

The estimated phase difference $\hat{\varphi}(n)$ will be used for two things, first to update $\mathbf{B}(n)$ and second to form the input for the next stage. Updating $\mathbf{B}(n)$ has been discussed in Eq. (4.6) and (4.7). The preparation of the signal for the next stage will be discussed in Section 4.3.4.

4.3.3 Equalizer

The equalization scheme used in the proposed SET is similar to [69] and includes a DFE with $\mathbf{W_f}(n)$ and $\mathbf{W_b}(n)$ as the feedforward and feedback FIR filters respectively and a channel estimator $\mathbf{W_h}(n)$. As discussed in [69], the addition of the channel estimator can improve the performance of the structure in terms of stronger CCI attenuation and more effective ISI compensation. In the scheme used here, $\mathbf{W_f}(n)$ and $\mathbf{W_h}(n)$ are getting updated. The signal $y_t(n)$ (see Figure 4.2) and accordingly $e_{MMA}(n)$ in Eq.(4.5), can be used to update $\mathbf{W_f}(n)$. As was proposed in [80] $\mathbf{W_f}(n)$ and $\mathbf{W_q}(n)$ can be updated jointly. Further, $\mathbf{W_h}(n)$ and $\mathbf{W_a}(n)$ can also be jointly updated using $e_s(n)$ defined in Eq.(4.8), as proposed in [69]. The updating equations are given by:

$$\mathbf{W_f}(n+1) = \mathbf{W_f}(n) - \mu_{\mathbf{f}}\, \widetilde{\mathbf{U}}_1(n) e^*_{MMA}(n) \tag{4.12}$$

where

$$\widetilde{\mathbf{U}}_1(n) = [u_1(n),\ u_1(n-1),\ \ldots, u_1(n-(\ell_1-1))]^T$$

and

$$\mathbf{W_h}(n+1) = \mathbf{W_h}(n) + \mu_{\mathbf{h}}\, \widetilde{\mathbf{D}}_1(n) e^*_s(n) \tag{4.13}$$

where $\widetilde{\mathbf{D}}_1(n)$ has been defined in Eq.(4.8). $\mu_{\mathbf{f}}$ and $\mu_{\mathbf{h}}$ are learning step sizes, and ℓ_1 is the length of $\mathbf{W_f}(n)$.

The postcursor response of the channel convolved with $\mathbf{W_f}(n)$ would be cancelled by $\mathbf{W_b}(n)$ which is the basic principle of the decision feedback equalizer [69]. Thus, $\mathbf{W_b}(n)$ can be set to:

$$\mathbf{W_b}(n) = \text{post}\{\mathbf{W}_f(n) \otimes \mathbf{W}_h(n)\} \tag{4.14}$$

where $\text{post}\{\ \}$ denotes the postcursor-taking operation, and $\otimes$ shows convolution. The decision maker maps its input to the nearest alphabet in terms of Euclidean distance. Also, *f(n)* in Figure 4.2 is a weighting factor defined as follows (ε is a small constant):

$$f(n) = 1 - \mathrm{e}^{\varepsilon n} \tag{4.15}$$

4.3.4 Preparing the signal for the next stage

The input to the second stage is $\mathbf{X}_2(n)$ can be obtained as follows. First the estimated phase $\hat{\varphi}(n)$ will be used to compensate for any gain mismatch of the AGSC at the corresponding DOA. The gain of the AGSC at $\hat{\varphi}(n)$ is obtained using:

$$\Omega = \sum_{m=0}^{M-2} e^{-jm\hat{\varphi}(n)} w_m^* \tag{4.16}$$

where

$$\mathbf{W} = [w_0 \quad w_1 \quad \ldots \quad w_{M-3} \quad w_{M-2}]^T = \mathbf{W_q}(n) - \mathbf{B}(n)\mathbf{W_a}(n)$$

Then, in order to normalize the beampattern to unity at $\hat{\varphi}(n)$, $u_1(n)$ is multiplied by $G = 1/\Omega$. The resulting signal $\hat{t}(n) = G\, u_1(n)$ in Figure 4.2 is an approximation of the signal transmitted by the detected user at the first stage and corrupted by the corresponding channel and noise (i.e. $t_q(n)$ in Eq.(4.1) plus noise). In order to form the input for the second stage, the received data from the q^{th} user will be subtracted from the antenna input $\mathbf{X}_1(n)$. To this end, $\hat{t}(n)$ will be multiplied by the estimated array manifold vector formed by $\hat{\varphi}(n)$ as follows:

$$\hat{\mathbf{V}}(n) = [1 \quad e^{-j\hat{\varphi}(n)} \quad \ldots \quad e^{-j(M-1)\hat{\varphi}(n)}]^T \tag{4.17}$$

The input for the second stage then becomes:

$$\begin{aligned} &\mathbf{X}_2(n) = \mathbf{X}_1(n) - \hat{\mathbf{T}}(n) \\ &\text{where} \quad \hat{\mathbf{T}}(n) = \hat{t}_q(n)\, \hat{\mathbf{V}}_q(n) \end{aligned} \tag{4.18}$$

In general, the input to the $(q+1)^{th}$ stage is $\mathbf{X}_{q+1}(n) = \mathbf{X}_q(n) - \hat{\mathbf{T}}(n)$ (see Figure 4.1), obtained in the same way as described in Eq.(4.16)-(4.18).

4.3.5 Stage Switching Scheme

A problem with multistage methods, [74]- [78] and [80], is that the residual error from the q^{th} stage ($q = 1,2,...,Q$) will propagate to the next one due to the fact that each stage is fed from the previous one. This drawback results in slow convergence and more errors for the last stages. To alleviate this problem, the mean square error (MSE) value at each iteration will be used to reassign users to the stages. Since the true transmitted data is not available, the MSE (see Figure 4.2) can be estimated using [81]:

$$MSE^{(q)}(n+1) = \lambda MSE^{(q)}(n) + (1-\lambda)\left|\hat{d}(n-\Delta) - y_t(n)\right|^2 \tag{4.19}$$

where λ is constant forgetting factor and Δ is decision delay. If :

$$MSE^{(q+1)}(n+1) < \beta MSE^{(q)}(n+1) \qquad \text{where} \quad 0 < \beta \le 1 \tag{4.20}$$

then all the parameters of the $(q+1)^{th}$ stage will be replaced by the parameters of the q^{th} stage. This is equivalent with switching the users detected by stages $q+1$ and q.

4.4 Convergence Acceleration Algorithms for the proposed STE

To speed up the convergence of the proposed multi-stage STE, two algorithms are suggested in this section. The first algorithm estimates initial phase shifts corresponding to DOAs for all stages. The second algorithm updates the learning-step sizes to provide a good comprise between convergence speed and stability.

4.4.1 The phase shift Initialization

For the initialization of the STE, the initial phase shift ($\hat{\varphi}(0)$) could be set equal to zero or one could use any of the well-known DOA estimation algorithms to obtain an initial estimate of the DOA. However, algorithms such as MUSIC [65] or ESPRIT [66] require many computations and algorithms like MP [67] which entails less computations requires at least $2Q$ antenna elements (Q is the number of user). To speed up convergence without many computations, a simple approach is proposed here which can provide good initial estimate for $\hat{\varphi}(0)$ very fast.

Consider $\mathbf{X}_1(n)$ in Eq. (4.1) and assume that there is no noise or the noise power is very small. By applying N-point discrete Fourier Transform (DFT) to $\mathbf{X}_1(n)$, i.e. DFT in the spatial dimension and zero-padding by adding $N-M$ zeros, we get:

$$\begin{aligned} X_1(k) &= \sum_{i=0}^{N-1} x_i(n) e^{-j\frac{2\pi}{N}ik} \\ &= \sum_{i=0}^{N-1} \left(\sum_{q=1}^{Q} t_q(n) e^{-j\varphi_q i} \right) e^{-j\frac{2\pi}{N}ik}, \\ &= \sum_{q=1}^{Q} t_q(n) \left(\sum_{i=1}^{N-1} e^{-j(\varphi_q + \frac{2\pi}{N}k)i} \right), \qquad \text{for } 0 \le k \le N-1 \end{aligned} \tag{4.21}$$

It can be easily shown that Eq.(4.21) can be expressed as:

$$X_1(k) = \sum_{q=1}^{Q} t_q(n) e^{-j\left(\varphi_q + \frac{2\pi k}{N}\right)\left(\frac{N-1}{2}\right)} \frac{\sin\left(\frac{N\varphi_q}{2} + \pi k\right)}{\sin\left(\frac{\varphi_q}{2} + \frac{\pi k}{N}\right)}, \qquad \text{for } 0 \le k \le N-1 \tag{4.22}$$

where $X_1(k)$ is the DFT of the input signal (in the spatial dimension) for the n^{th} snapshot. The Q largest peaks of $X_1(k)$ would occur at $k = -N\varphi_q / 2\pi$ ($q = 1,2,...,Q$) or equivalently at:

$$\theta_q = \arcsin\left(-\frac{2k}{N}\right) \tag{4.23}$$

Thus, by finding k at the maxima, an initial estimate of the DOAs can be obtained. In the presence of noise this estimate may not be accurate if M (the number of sensors) is not large compared to Q (the number of users). However, in such a case the accuracy can be improved by

averaging the peaks of the DFTs, $X_1(k)$, obtained for a sequence of J snapshots. This will be illustrated with simulations in section 4.6.

4.4.2 Choosing appropriate learning step sizes

In order to choose an appropriate value for the step sizes $\mu_{\mathbf{q}}$, $\mu_{\mathbf{f}}$, $\mu_{\mathbf{h}}$ and $\mu_{\mathbf{a}}$, a trade-off between convergence speed and stability should be considered. In the updating equations, Eq.(4.5), (4.9) and (4.12) , $\widetilde{\mathbf{X}}_1(n)$, $\mathbf{r}(n)$, and $\widetilde{\mathbf{U}}_1(n)$ are obtained from the STE input. Therefore, at the presence of several users their amplitude may be quite large. In this case to guarantee convergence, $\mu_{\mathbf{q}}$, $\mu_{\mathbf{f}}$, and $\mu_{\mathbf{a}}$ should be set to small values. From Figure 4.2 it can be seen that the $\mathbf{W}_{\mathbf{h}}(n)$ is fed from the output of the decision making equalizer, $\widetilde{\mathbf{D}}_1(n)$ in Eq.(4.8), which has a considerably smaller amplitude than $\widetilde{\mathbf{X}}_1(n)$, $\mathbf{r}(n)$, and $\widetilde{\mathbf{U}}_1(n)$, especially at the presence of several users. As a consequence, $\mu_{\mathbf{h}}$ can be set to a larger value compared to $\mu_{\mathbf{q}}$, $\mu_{\mathbf{f}}$, and $\mu_{\mathbf{a}}$.

To speed up the convergence of the proposed STE, the step sizes are adjusted based on the following algorithm. When the MSE at a stage converges to a satisfactory small value, this indicates that both errors $e_{MMA}(n)$ and $e_s(n)$ are small at this stage and also in the previous stages since all stages are sorted from minimum to maximum MSE. It can therefore be concluded that the signals of the detected users are (almost) excluded from the input to the next stages. Consequently, the input amplitudes for the next stages are expected to have smaller amplitudes than the inputs to the earlier stages. Since the earlier stages have already converged and the amplitudes to the next stages are small, the magnitudes of $\mu_{\mathbf{q}}$, $\mu_{\mathbf{f}}$, and $\mu_{\mathbf{a}}$ for all stages can be increased. This is implemented using the following algorithm:

---

if $\sum_{k=1}^{Q-1} MSE^{(k)} < (Q-1)\,\xi$

Multiply the initial values of $\mu_{\mathbf{q}}, \mu_{\mathbf{f}}$, and $\mu_{\mathbf{a}}$ with $\gamma_{\text{Q-1}}$

elseif $\sum_{k=1}^{Q-2} MSE^{(k)} < (Q-2)\,\xi$

Multiply the initial values of $\mu_{\mathbf{q}}, \mu_{\mathbf{f}}$, and $\mu_{\mathbf{a}}$ with $\gamma_{\text{Q-2}}$

$\vdots$

elseif $MSE^{(1)} < \xi$

Multiply the initial values of $\mu_{\mathbf{q}}, \mu_{\mathbf{f}}$, and $\mu_{\mathbf{a}}$ with γ_1

else

Keep the initial values of $\mu_{\mathbf{q}}, \mu_{\mathbf{f}}$, and $\mu_{\mathbf{a}}$

The constant ξ is an appropriate threshold depending on the modulation scheme [81]. Also, γ_{i} are constants arranged in this order $\gamma_{\text{Q-1}} > \gamma_{\text{Q-2}} > \ldots > \gamma_1$.

4.5 Implementation of the proposed STE

The multi-stage STE algorithm can be summarized as follows:

For all stages:

Initialization Mode:

Initialize the phase shift $\hat{\varphi}(0)$ using the algorithm described in section 4.4.1. Based on $\hat{\varphi}(0)$ initialize $\mathbf{W_q}(0)$ using Eq.(4.6). Set $\mathbf{W_a}(0)$ and $\mathbf{W_h}(0)$ to all-zero vectors, and $\mathbf{W_f}(n)$ to an all zero-vector except the first element which is set to one. The initial $MSE^{(q)}(0)$ is set to one for $q = 1,2,...,Q$. Set n to zero and go to the operating mode.

Operating Mode:

1- Using $\hat{\varphi}(n)$, form $\mathbf{B}(n)$ using the method described in section 4.3.1.

2- Form $\mathbf{W_q}(n) - \mathbf{B}(n)\mathbf{W_a}(n)$, and normalize the beampattern to unity at $\hat{\varphi}(n)$ using Eq. (4.16).

3- Using $\hat{\varphi}(n)$, form the input for all stages using Eqs. (4.17) and (4.18).

4- Using Eq.(4.14), find $\mathbf{W_b}(n)$. Set the length of $\mathbf{W_b}(n)$ to $\ell_1 + \ell_2 - 2 - \Delta$ (ℓ_1 and ℓ_2 are the lengths of $\mathbf{W_f}(n)$ and $\mathbf{W_h}(n)$, and Δ is the decision delay in Figure 4.2.

5- Find $\mathbf{W_q}(n+1)$ and $\mathbf{W_a}(n+1)$ using Eq. (4.5) and (4.9) , and also $\mathbf{W_f}(n+1)$ and $\mathbf{W_h}(n+1)$ using Eq. (4.12) and (4.13).

6- Estimate the new phase difference ($\hat{\varphi}(n+1)$) using Eq. (4.11).

7- Measure $MSE^{(q)}(n+1)$ using Eq. (4.19), and sort the stages based on the rule described in Eq. (4.20) so that the stage with lowest MSE is first and the one with the largest is last.

8- Update the learning step size $\mu_{\mathbf{q}}, \mu_{\mathbf{f}}$, and $\mu_{\mathbf{a}}$ using the algorithm described in section 4.4.2.

9- Increase n by one and go back to step 1.

4.6 Simulation Results

In this section, four simulations are presented to illustrate the performance of the proposed STE:

- The first simulation shows the performance of the DOA initialization method discussed in section 4.4.1.
- The second simulation demonstrates the effectiveness of the stage-switching scheme.
- In the third simulation the robustness and reliability of the proposed STE is evaluated for 250 independent simulations with random generated signals and noise.
- The fourth simulation illustrates the algorithm ability to track moving users in the presence of time varying channels.

In Table 4.1 the parameters used in the simulations are given. In all simulations, the modulation scheme used is 4-QAM, and the data transmitted from each user is generated randomly. Further, for the first three simulations four users are considered with the DOAs, $\theta_1 = 15^o$, $\theta_2 = -30^o$, $\theta_3 = -60^o$, and $\theta_4 = 45^o$. The channels in these three simulations are fixed and given by:

$$\mathbf{h}_1 = [0.407 \quad 0.815 \quad 0.407],$$
$$\mathbf{h}_2 = [0.8 + 0.6j \quad 0.1 \quad 0.4 + 0.6j],$$
$$\mathbf{h}_3 = 1 \text{ (fading-free) and}$$
$$\mathbf{h}_4 = [0.6 \quad 1 \quad 0.8]$$

The zeros of $\mathbf{h}_1$, $\mathbf{h}_2$, and $\mathbf{h}_4$ are shown in Figure 4.3. As it can be seen, $\mathbf{h}_1$ and $\mathbf{h}_4$ are non-minimum phase channels and quite challenging to be equalized since they have zeros close to the unit circle [64].

Table 4.1. Simulations Parameters

Parameter	**Second & Third Simulation**	**Fourth Simulation**
N_s : Number of samples	15000	25000
M : Number of sensors	6	5
SNR: Signal to Noise Ratio (dB)	20	20
ℓ_1 : Length of $\mathbf{W_f}(n)$	7	7
ℓ_2 : Length of $\mathbf{W_h}(n)$	5	5
ℓ_3 : Length of $\mathbf{W_b}(n)$	9	9
Δ : Decision delay	1	1
$\mu_{\mathbf{q}}$: Learning step size in Eq. (4.5)	0.00002	0.0001
$\mu_{\mathbf{a}}$: Learning step size in Eq. (4.9)	0.00002	0.0001
μ_{φ} : Learning step size in Eq. (4.11)	0.001	0.001
$\mu_{\mathbf{f}}$: Learning step size in Eq. (4.12)	0.00002	0.0001
$\mu_{\mathbf{h}}$: Learning step size in Eq. (4.13)	0.01	0.01
τ : Positive constant in Eq. (4.11)	0.001	0.001
ε : Constant in Eq. (4.15)	0.01	0.01
β : Constant in Eq. (4.20)	0.25	0.25
N : Number of points in section 4.4.1	512	512
J : Number of snapshots in section 4.4.1	20	20
ξ : Constant in section 4.4.2	0.2	0.2
γ_1 : Constant in section 4.4.2	3	2
γ_2 : Constant in section 4.4.2	6	3
γ_3 : Constant in section 4.4.2	9	--

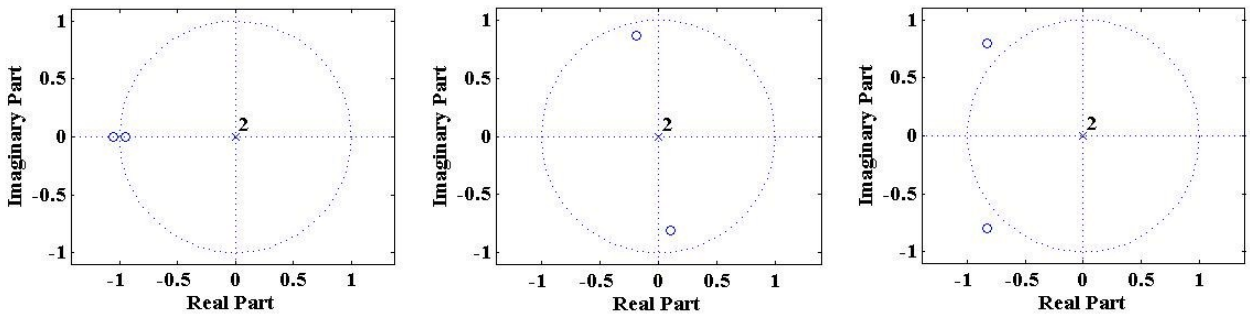

(a) $\mathbf{h}_1$ (b) $\mathbf{h}_2$ (c) $\mathbf{h}_4$

Figure 4.3. The zeros location for different channel

***First Simulation*:** In this simulation, the performance of the DOA estimation algorithm described in section 4.4.1 will be evaluated for different number of sensors (M) and SNR. To this end, for a fixed M and SNR, the DOAs are estimated for 1000 independent simulations. For all cases, 512-point DFT is considered ($N = 512$). The results are shown in Figure 4.4 for one snapshot ($J = 1$). Red triangles indicate the real DOA in this Figure. It can be seen that the estimation accuracy gets better as M increases. Interestingly, the estimated DOA is accurate even in the presence of severe noise provided that M is large enough. The accuracy of the estimated DOA for small M can be increased, as mentioned in section 4.4.1, by finding the peaks of the average of $X_1(k)$ for a sequence of J snapshots. To illustrate the effect of averaging, the results for two different SNRs, $M = 6$, and $J = 20$ are shown in Figure 4.5.

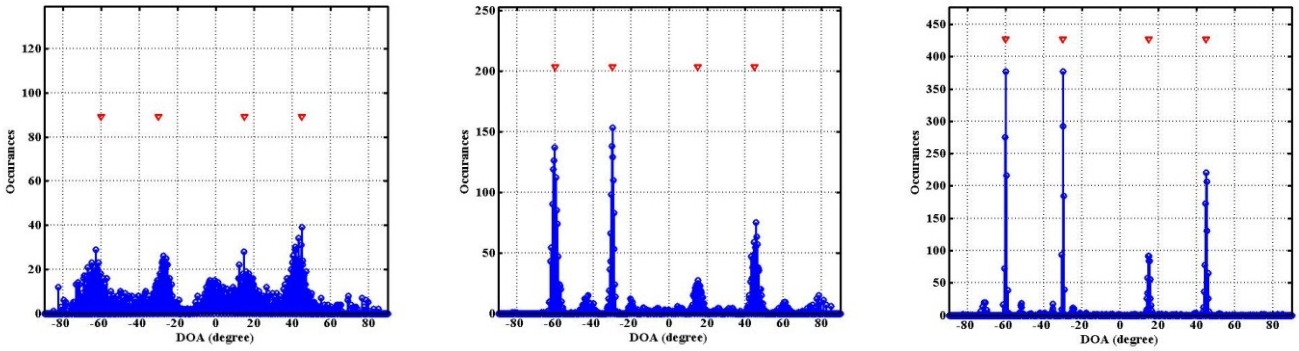

SNR=0 dB, and $M = 6$ SNR=0 dB, and $M = 18$ SNR=0 dB, and $M = 36$

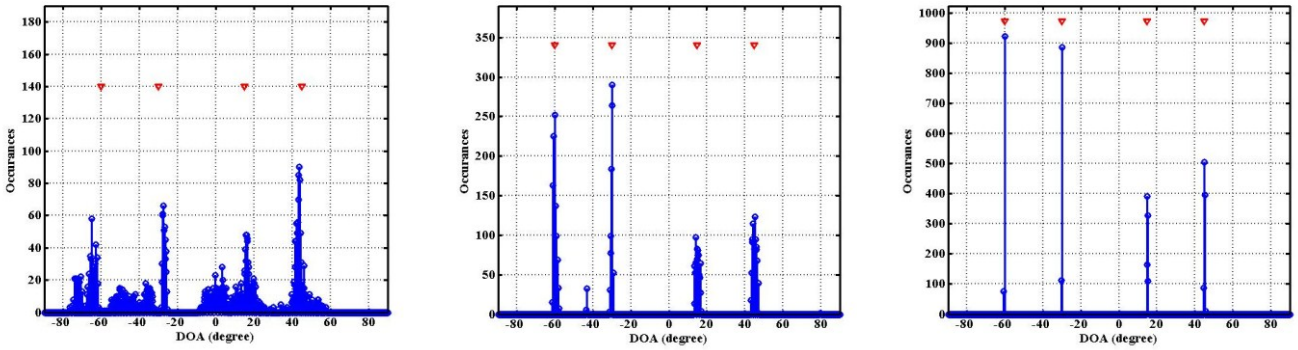

SNR=20 dB, and $M = 6$ SNR=20 dB, and $M = 18$ SNR=20 dB, and $M = 36$

Figure 4.4. First simulation, DOAs estimation for different SNRs and M

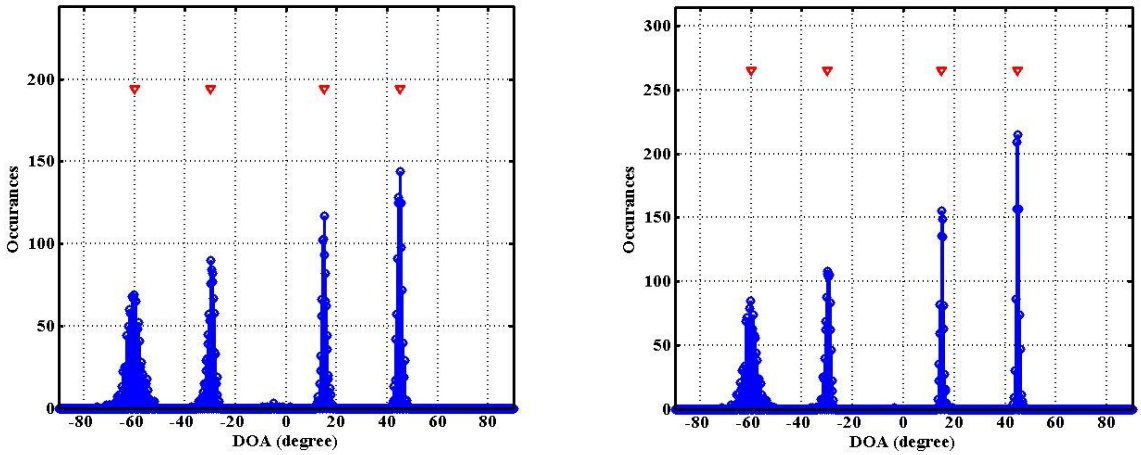

SNR= 0 dB, $M = 6$, and $J = 20$ SNR= 20 dB, $M = 6$, and $J = 20$

Figure 4.5. First simulation, DOAs are estimated by averaging over a sequence of 20 snapshots

***Second Simulation*:** In this simulation, the effectiveness of the stage-switching scheme will be illustrated and it will be shown that the proposed STE is robust to mismatch between the initial and real DOAs. For the system considered here, the easiest channel to be equalized is $\mathbf{h}_3$ ($\theta_3 = -60^o$) which is fading-free and the second easiest channel is $\mathbf{h}_2$ ($\theta_2 = -30^o$) which is minimum phase. Further, the zeros of $\mathbf{h}_1$ ($\theta_3 = 15^o$) are closer to the unit circle than the zeros of $\mathbf{h}_4$ ($\theta_3 = 45^o$) which implies that fading is deeper for $\mathbf{h}_1$ [64] and thus equalizing $\mathbf{h}_1$ is more challenging than $\mathbf{h}_4$. So, the expected behavior of the proposed STE after convergence is to lock on the users according to the following order: the third user at the first stage, the second user at the second stage, the fourth user at the third stage, and the first user at the final stage. Let's now initialize the STE as follows: stage 1 with the first user at 10^o as the DOA, stage 2 with the fourth user at 50^o DOA, stage 3 with the second user at -35^o DOA, stage 4 with the third user at -65^o DOA. This initialization implies 5^o initial DOA mismatch for all users and further, assigns the users to the stages with an opposite order than the one expected based on the discussion above. The first user being the most challenging to be equalized is expected to produce a significant residual error at the beginning which will be propagating to the other stages. The level of residual error at each stage is an indication of the difficulty of equalizing the channel for the user detected by this stage. Thus the initialization chosen here represents one of the worst possible initializations. The function of the switching scheme in the proposed STE is to place the stage with the most MSE last and thus lead to a small residual error for all stages at convergence. To illustrate this, the MSE of all stages as defined in Eq.(4.19) is plotted in Figure 4.6 (a) and (b) for the following two cases: when all stages are fixed and no switching is allowed and when the stages are switched based on the rule defined by Eq. (4.20). Clearly, the

switching scheme will lead to faster converge and the final MSE is considerably lower than in the case where there is no switching. The estimated DOAs for these two cases are shown in Figure 4.6 (c) and (d). As it can be seen, the estimation accuracy is better when switching is used. To provide a view of switching in time as well as the order of switching, the estimated DOAs for different stages at the switching moments along with the initial and last DOA estimations are shown in Table 4.2. Colors in this table represent different users and are also indicating the level of difficulty for equalizing each user from green (the easiest user) to red (the most difficult user). Clearly, after convergence, the order of the users detected by each stage is from the easiest to the most difficult, consistent with the earlier discussion.

In order to clarify the improvement of using the AGSC proposed instead of the beamformer used in [80] (consisting of only updating $\mathbf{W_q}(n)$), the final beampatterns normalized with $G = 1/\Omega$ (Figure 4.2 and Eq.(4.16)) for these two cases are shown in Figure 4.7. It can be seen that the AGSC of the first stage tries to pass data propagating from -60^o and reject other users. That's why the beampattern of the first beamformer has three deep nulls at -30^o, 15^o, and 45^o. For the second stage, since one of the users at -60^o is excluded from the second stage input (Eq.(4.18), see Figure 4.1), the beampattern has just two deep nulls corresponding to the two remaining users at 15^o and 45^o. Due to the same reason, the third beampattern has just one deep null at 15^o. Clearly the use of AGSC leads to deep nulls and to strong CCI attenuation for the proposed STE.

Table 4.2. Second simulation, the Estimated DOAs (in degrees) at n^{th} Sample.

Entries with the same color correspond to the same user

n	0	885	886	887	889	980	981	982	2276	2277	15000
Stage # 1	10	15.20	15.16	15.34	-59.30	-60.91	-60.68	-60.57	-59.59	-59.69	-59.88
Stage # 2	50	46.35	46.39	-59.21	15.11	14.52	14.54	-29.72	-30.07	-30.04	-29.93
Stage # 3	-35	-30.63	-59.24	46.47	46.42	45.65	-29.63	14.80	14.83	45.68	44.98
Stage # 4	-65	-59.19	-30.33	-30.35	-30.27	-29.63	45.80	45.85	45.72	14.84	15.02

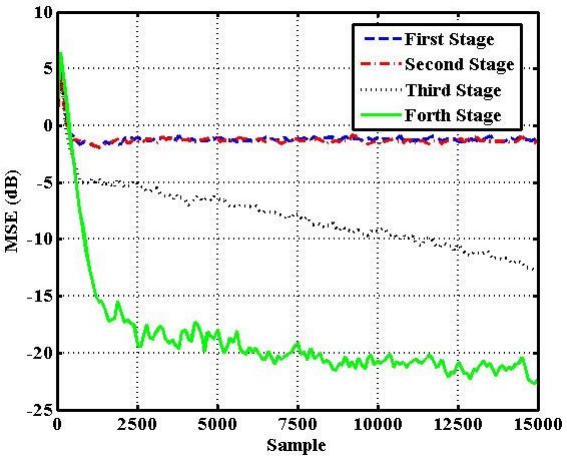

(a) MSE when no switching is allowed

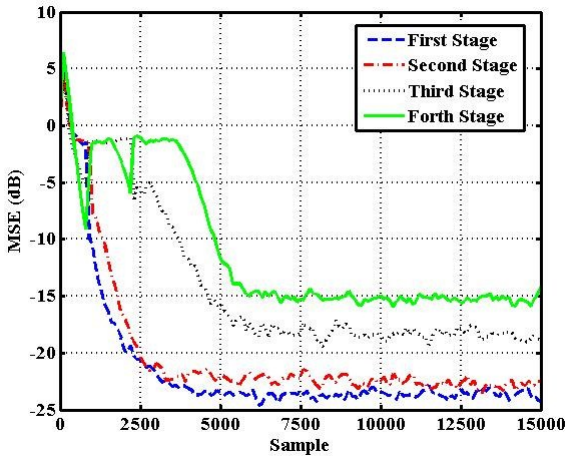

(b) MSE when stage-switching scheme is considered

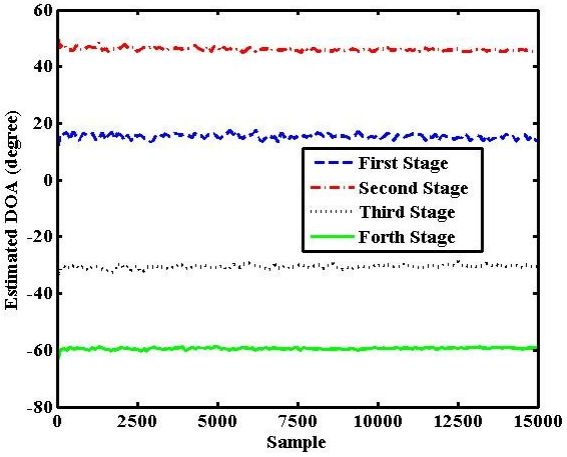

(c) Estimated DOAs when no switching is allowed

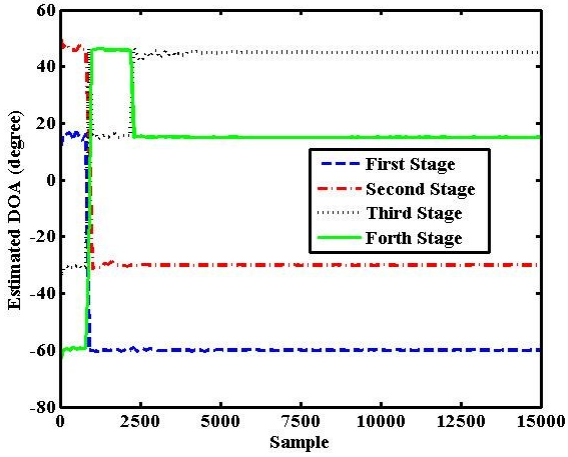

(d) Estimated DOAs when stage-switching scheme is considered

Figure 4.6. Second simulation, MSE and estimated DOAs for two cases: when all stages are fixed and no switching is allowed and when the stages are switched based on the rule defined in Eq. (4.20).

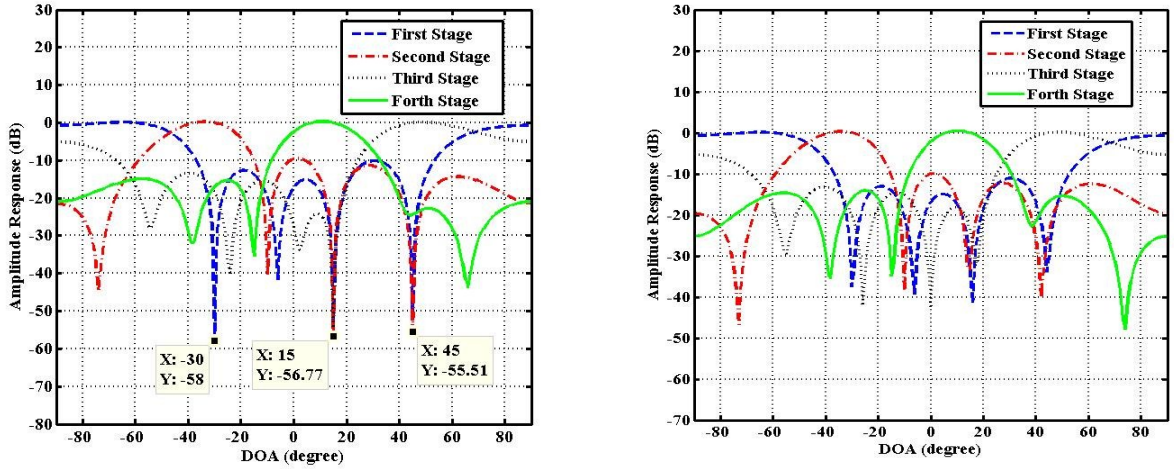

(a) (b)

Figure 4.7. Second simulation, the normalized beampattern for (a) $\mathbf{W}_q(n) - \mathbf{B}(n)\mathbf{W}_a(n)$, and (b) $\mathbf{W}_q(n)$

***Third Simulation*:** In the third simulation a similar scenario as in the second simulation is considered. The only difference is that the initialization of the DOA is done using the method proposed in section 4.4.1, and the simulation is repeated 250 times with randomly generated signals and noise. The averaged MSE (dB) over 250 independent simulations is shown in Figure 4.8. The initial DOAs along with the final estimated DOAs are shown in Figure 4.9 (a)-(b). Red triangulars show the real DOAs. Both Figure 4.8 and Figure 4.9 illustrate the good performance of the proposed STE in terms of low MSEs and estimated DOAs.

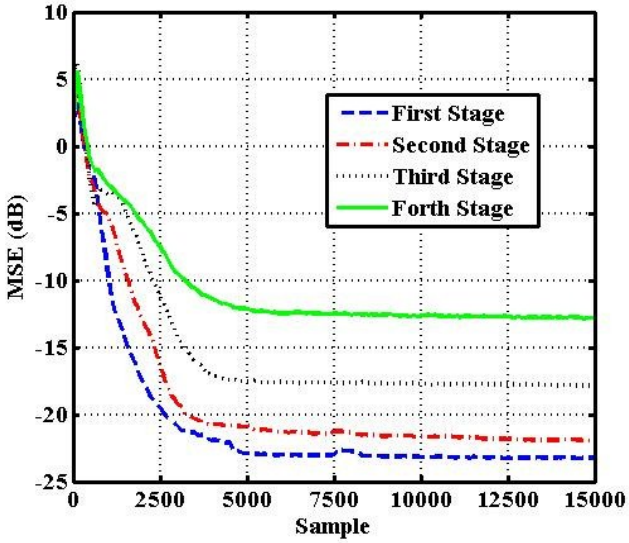

Figure 4.8. Third simulation, the averaged MSE over 250 simulations

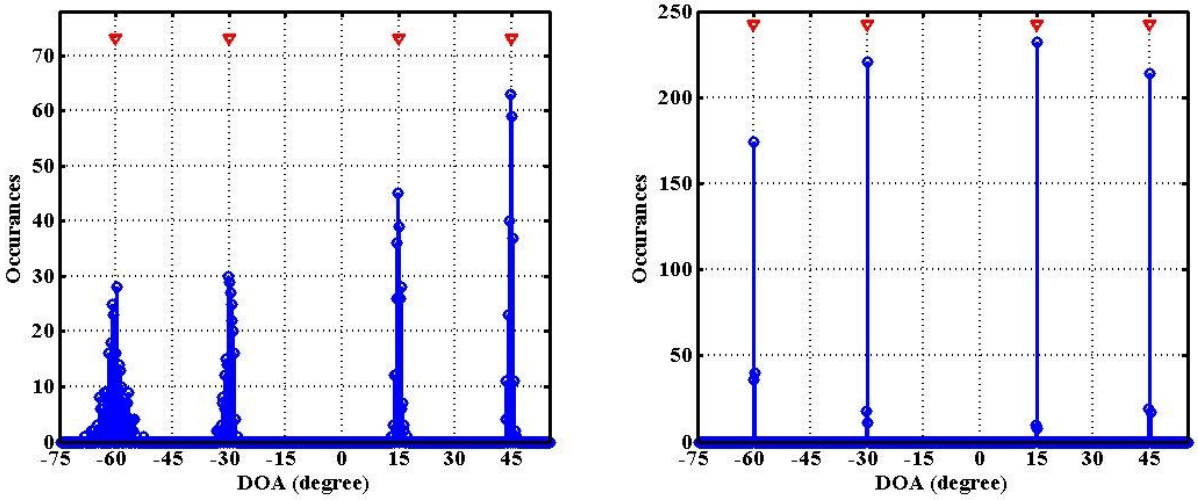

(a) initial DOA (b) final DOA

Figure 4.9. Third simulation, the estimated DOAs

***Fourth simulation*:** In this simulation, the performance of the proposed STE in the case of users with varying DOA and time-varying channels will be illustrated. Consider the case of three users with initial DOAs from $\theta_1 = -35^o$, $\theta_2 = 0^o$, and $\theta_3 = 45^o$. The initial channel for the first user is $\mathbf{h}_3 = [0.407 \quad 0.815 \quad 0.407]$ (shown in Figure 4.3 (a)), and the two other channels are fading free. From the 3000^{th} sample to the 5000^{th} sample all DOAs are changing very fast in a linear fashion as shown in Figure 4.10 (a). As it can be seen around the 4000^{th} sample the first and second users' DOA overlap which makes the scenario very challenging. Further, at the 3000^{th} sample a time-varying zero at $0.8\exp(j2\pi/3) + 0.4\exp(j2\pi[n-3000]/10000)$ will be added to the second channel $\mathbf{h}_2$, as in [81], and the fading-free $\mathbf{h}_1$ will be replaced by $[1 \quad 0.8 \quad 0.6]$. For the whole time, $\mathbf{h}_3$, a channel with deep fading, remains the same. At the 5000^{th} sample, all DOAs and channels get fixed and remain unchanged. The zero locations for $\mathbf{h}_2$ at the 3000^{th} and 5000^{th} samples are shown in Figure 4.10 (b) which show that the channel is changing form minimum phase to non-minimum phase. The zeros of $\mathbf{h}_1$ after the 5000^{th} sample are shown in Figure 4.10 (c) indicating a minimum phase channel. The MSE averaged over 250 simulations is shown in Figure 4.11 (a) which shows a very good performance. Further, the final beampattern (normalized with G, Eq. (4.16)) for all three stages is shown in Figure 4.11 (b). It can be seen that the beampattern at each stage has a unity gain at the DOA of the detected user (shown by arrows) and deep nulls in the direction of the other users. This indicates a good performance in CCI cancellation for the proposed STE. Finally, the estimated DOAs averaged over 250 independent simulations are shown in Figure 4.12. The dotted green lines show the real DOAs. As it can be seen the final estimated DOA is accurate which demonstrates the ability of STE to track moving users in the presence of time-varying channels.

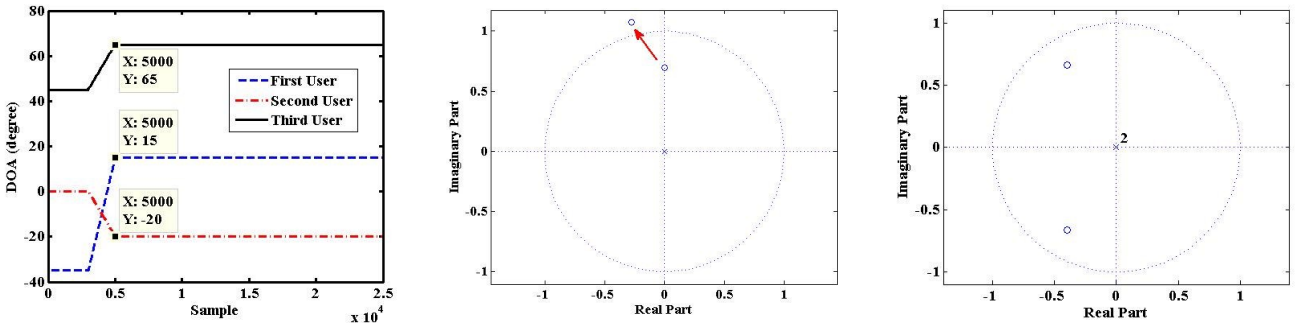

(a) (b) (c)

Figure 4.10. Fourth simulation, (a) time-varying DOAs for the three users, (b) the moving zero of $\mathbf{h}_2$, and (c) $\mathbf{h}_1$ after the 5000 th sample

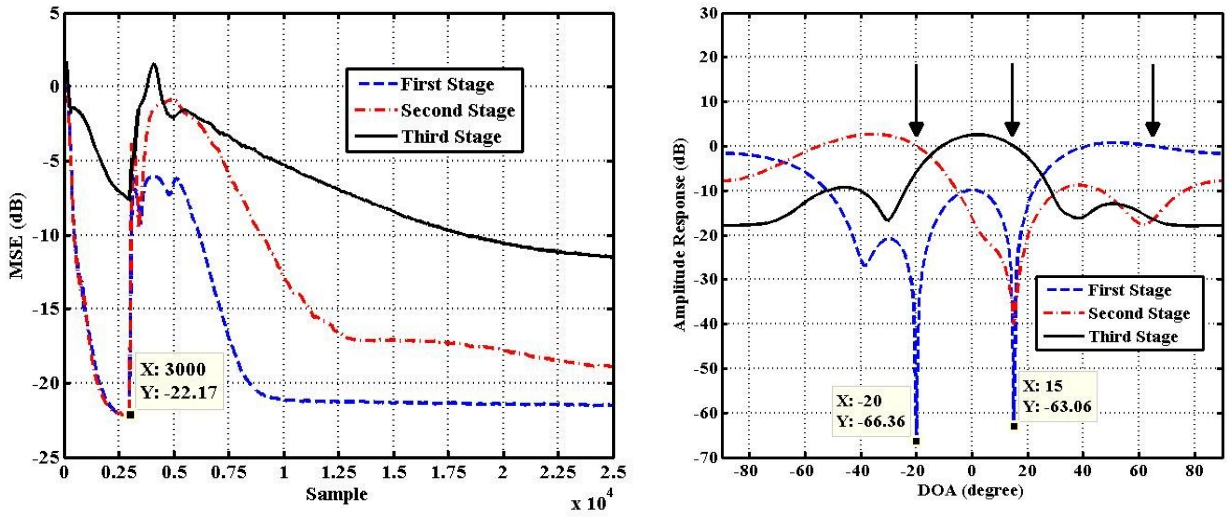

(a) (b)

Figure 4.11. Fourth simulation, (a) averaged MSE, and (b) the normalized beampattern

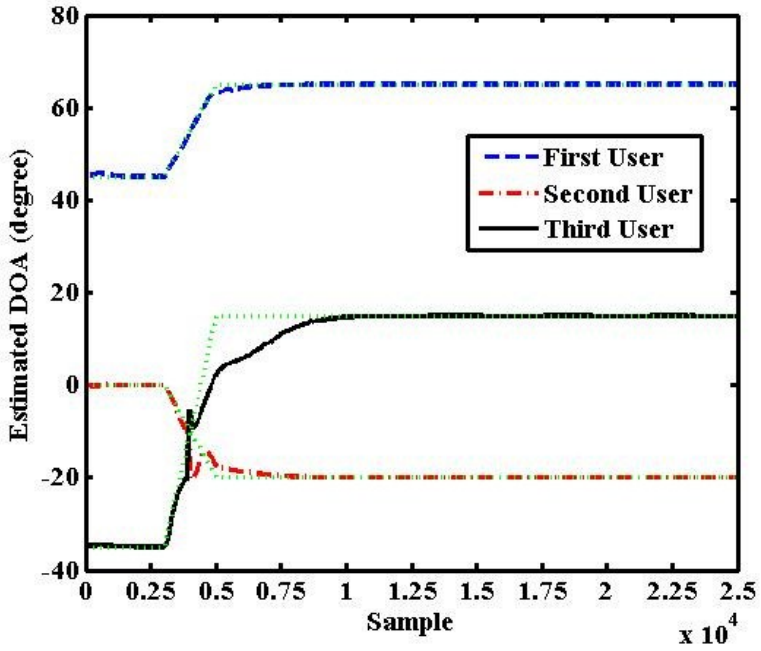

Figure 4.12. Fourth simulation, the average of estimated DOAs

4.7 Summary

In this chapter, a new multi-stage STE is proposed for BSS. Each stage is equipped with an adaptive version of the GSC, called AGSC, DOA estimator, and an equalizer. The beamformer and equalizer are jointly being updated to combat both CCI and ISI effectively. Taking advantage of subarray beamformers, the DOA, possibly time-varying, of the captured signal is estimated and tracked. The estimated DOA is being used by the blocking matrix of AGSC to provide strong CCI cancellation. Further, the estimated DOAs will be used to form the input to the next stages. In order to significantly alleviate inter-stage error propagation, a sorting

algorithm is used which assigns detected sources to different stages from minimum MSE to the maximum. Further, to speed up the convergence, a simple-yet-efficient DOA estimation algorithm is proposed which can provide good initial DOAs for the multi-stage STE. Simulation results demonstrate the good performance of the proposed STE and show that it can effectively deal with changing DOAs and time variant channels.

CHAPTER 5

CONCLUSIONS AND FUTURE WORK

5.1 Conclusions

The main focus of this dissertation has been the application of array signal processing for broadband beamforming and blind source separation. In Chapter 2, a broadband beamformer has been proposed using nested arrays, multirate systems, and FIR M-D filters. This beamformer needs a special filter bank with non-compatible sampling set which is challenging to be designed. A general design approach has been presented in Chapter 3 which is applicable to both uniform and non-uniform filter banks. Chapter 4 is dedicated to array signal processing for narrowband signals. In this chapter, a multi-stage STE for blind source separation has been proposed.

5.1.1 Broadband Beamforming Using Multi-Dimensional Filers, Nested Arrays, and Multi-Rate Techniques

Our attention in Chapter 2 was mainly focused on the combination of nested arrays, multirate techniques, and M-D filters. First, the basic idea of using M-D filters as the fixed broadband beamformers was presented for the case when the antenna was a ULA and beamformer was TF. It has been shown that the beamformer's behavior is frequency-dependent due to finite aperture effect. In other words, the selectivity at high frequencies is better than at low frequencies. Then, in order to achieve a frequency-invariant beampattern, a ULA was replaced with 1D nested arrays composed of several ULAs with increasing distance. The

advantage of using nested arrays is that the effective aperture for low temporal frequencies is larger than in the case of using ULA. This results in high spatial selectivity for low frequencies. Next, in order to jointly cover zenith and azimuth angles, 1D antenna was replaced with a 2D antenna, and a broadband beamformer has been proposed using nested hexagonal arrays, multirate techniques, and frustum filters. The use of hexagonal arrays was motivated from the fact that they are known to require a lower sensor density for alias free sampling than rectangular arrays. Finally, an efficient implementation of the proposed beamformer has also been presented based on eliminating redundant computations using the Nobel identity and polyphase structures.

The nested arrays arrangement corresponds to subsampling in the spatial domain followed by subsampling in temporal domain. Appropriate subsampling in space and time for each subarray leads to signals with the same ROS in the frequency domain for all subarrays allowing the use of the same M-D filter design for all subbands. Through the simulations, it has been illustrated that when the number of sensors is given, the beampattern of the proposed method is almost frequency invariant, and if the aperture size is given, the proposed method can be implemented with significantly fewer sensors (and accordingly less computation) than uniform arrays with only a slight deterioration in performance.

5.1.2 A Method for Filter Bank Design Using Optimization

A method to design filter banks using optimization has been presented in Chapter 3. The approach is based on formulating the design problem as an optimization problem with a performance index which consists of a term depending on perfect reconstruction and a term depending on the magnitude specifications for the analysis filters. Perfect reconstruction for FIR

analysis and synthesis filters is formulated as a set of linear equations using z-domain analysis. The design objectives are to minimize the perfect reconstruction error and have the analysis filters satisfying some prescribed frequency specifications. This approach not only can design the filter bank needed in Chapter 2, but also is applicable to uniform (including critically sampled and over sampled) and non-uniform filter banks (for sampling rates forming a compatible set as well as non-compatible set). Design examples illustrate the performance of the proposed method.

5.1.3 A Multi-Stage Space-Time Equalizer for Blind Source Separation

In Chapter 4, a new multi-stage STE has been proposed for BSS. Each stage is equipped with a beamformer, DOA estimator, and an equalizer. An adaptive version of GSC, called AGSC has been presented which can adaptively track a user and strongly attenuate other users with different DOAs. The beamformer and equalizer are jointly being updated (STE concept) to combat both CCI and ISI effectively. Using subarray beamformers, the DOA, possibly time-varying, of the captured signal is estimated and tracked. The estimated DOA is used by the AGSC to provide strong CCI cancellation, Further, the estimated DOAs is used to form the input to the next stages. In order to significantly alleviate inter-stage error propagation, a mean-square-error sorting algorithm is used which assigns detected sources to different stages according to the reconstruction error at different stages. Further, to speed up the convergence, a simple-yet-efficient DOA estimation algorithm is proposed which can provide good initial DOAs for the multi-stage STE. Simulation results have illustrated the good performance of the proposed STE and shown that it can effectively deal with changing DOAs and time variant channels.

5.2 Future Work

In what follows, three research topics are discussed as a continuation of the work presented in this dissertation.

5.2.1 A Fast DOA Estimation Technique

One of the main research areas in array processing is DOA estimation. A simple method to estimate DOAs is by means of beamforming in which a fixed beamformer is designed for different directions and then based on the power output, DOAs can be estimated. Obviously, the method involves an exhaustive search which is not efficient. For the case of narrow band signal, two well-known DOA estimation approaches are MUSIC and ESPRIT. Due to subspace estimation and eigen decomposition, they entail high computational complexity. Therefore, they cannot be used where the fast DOA estimation is needed. In contrast, DOA estimation techniques using MP are fast, but the DOA estimation capacity (maximum number of users which can be detected) is less than that of MUSIC and ESPIRIT.

The DOA estimation technique proposed in section 4.4.1 is interesting due to its simplicity and fast implementation. Our preliminary results demonstrate that the proposed method is very fast and entails significantly less computation than MUSIC and ESPRIT. Also, the method shows better capacity than MP. In this regard, it is worthwhile to comprehensively analyze this DOA estimation technique with respect to:

1- Driving the capacity for a given number of sensor
2- Evaluating the performance against number of snapshots and FFT size
3- Evaluating selectivity (the ability to estimate different DOAs for spatially close PWs) and noise sensitivity

5.2.2 A Multi-Stage Space-Time Equalizer at the presence of both temporal and spatial ISI

In Chapter 4, it was deemed that only CCI and temporal ISI are available. It would be interesting to extend the proposed method to the case when spatial ISI due to multipath is available as well. Since spatial ISI can be interpreted as the case when sources are correlated, one feasible extension is to modify the proposed structure according to [78] in order to cover both temporal and spatial ISI. Together with the current work, the proposed extension will form a blind multi-stage STE which has enough potential to be implemented in the wireless communication systems.

5.2.3 Broadband Beamformer

The possibility to use the wideband beamformers developed in Chapter 2 in applications where the signals are broadband PWs could be investigated. This may be done in areas such as audio signal processing or in processing of radio astronomy signals. Currently, in radio astronomy, broadband signals are processed using several narrowband channels. The possibility to employ the proposed beamformers in these areas would be interesting.

BIBLIOGRAPHY

[1] H. Van Trees, Optimum Array Processing (Detection, Estimation, and Modulation Theory, Part IV), Wiley, 2002.

[2] D. Udgeon and R. Mersereau, Multidimensional Digital Signal Processing, Prentice-Hall, 1983.

[3] W. Liu and S. Weiss, Wideband Beamforming: Concepts and Techniques, Wiley, 2010.

[4] O. L. Frost, "An algorithm for linearly constrained adaptive array processing," *Proceedings of the IEEE,* vol. 60, no. 8, pp. 926- 935, 1972.

[5] S. Haykin, Adaptive Filter Theory, Englewood Cliffs: Prentice-Hall, 1996.

[6] S. Applebaum and D. Chapman, "Adaptive arrays with main beam constraints," *IEEE Transactions on Antennas and Propagation,* vol. 24, no. 5, pp. 650- 662, 1976.

[7] J. Capon, "High-resolution Frequency-wavenumber Spectrum Analysis," *Proceedings of the IEEE,* p. 1408–1418, 1969.

[8] K. Ahmed and R. Evans, "An adaptive array processor with robustness and broadband capabilities," *IEEE Transactions on Antennas and Propagation,* p. 944–950, 1984.

[9] K. Buckley, "Spatial/Spectral Filtering with Linearly Constrained Minimum Variance Beamformers," *IEEE Transactions on Acoustics, Speech and Signal Processing,* p. 249–266, 1987.

[10] B. Veen, "Minimum variance beamforming with soft response constraints," *IEEE Transactions on Signal Processing,* p. 1964–1972, 1991.

[11] M. Brandstein and D. Ward, Microphone Arrays: Signal Processing Techniques and Applications, Berlin, Germany: Springer-Verlag, 2001.

[12] K. Slavakis and I. Yamada, "Robust wideband beamforming by the hybrid steepest descent method," *IEEE Transactions on Signal Processing,* p. 4511–4522, 2007.

[13] M. Rubsamen and A. Gershman, "Robust presteered broadband beamforming based on worst-case performance Optimization," in *Proceedings of the IEEEWorkshop on Sensor Array and Multichannel Signal Processing*, Darmstadt, Germany, 2008.

[14] J. Li and P. Stoica, Robust Adaptive Beamforming, Hoboken, NJ, USA: John Wiley & Sons, 2005.

[15] A. El-Keyi, T. Kirubarajan and A. Gershman, "Wideband robust beamforming based on worst-case

performance Optimization," in *Proceedings of the IEEE Workshop on Statistical Signal Processing*, Bordeaux, France, 2005.

[16] S. Nordebo, I. Claesson and S. Nordholm, "Weighted chebyshev approximation for the design of broadband beamformers using quadratic programming," *IEEE Signal Processing Letters,* p. 103–105, 1994.

[17] A. Bjorck, "Numerical Methods for Least Squares Problems," *Society for Industrial and Applied Mathematics (SIAM),* 1996..

[18] T. Chen, "Unified eigenfilter approach: with applications to spectral/spatial filtering," in *Proceedings of the IEEE International Symposium on Circuits and Systems*, Chicago, IL, USA, 1993.

[19] S. Doclo and M. Moonen, "Design of broadband beamformers robust against gain and phase errors in the microphone array characteristics," *IEEE Transactions on Signal Processing,* p. 2511–2526, 2003.

[20] T. Gunaratne and L. Bruton, "Beamforming of Broad-Band Bandpass Plane Waves Using Polyphase 2-D FIR Trapezoidal Filters," *IEEE Transactions on Circuits and Systems I,,* vol. 55, no. 3, pp. 838-850, 2008.

[21] K. Nishikawa, T. Yamamoto, K. Oto and T. Kanamori, "Wideband beamforming using fan filter," in *IEEE Int. Symp. Circuits Syst.*, 1992.

[22] L. Bruton, "Three-dimensional cone filter banks," *IEEE Transactions on Circuits and Systems I: Fundamental Theory and Applications,* vol. 50, no. 2, pp. 208- 216, 2003.

[23] T. Gunaratne and L. Bruton, "Broadband beamforming of dense aperture array (DAA) and focal plane array (FPA) signals using 3D spatio-temporal filters for applications in aperture synthesis radio astronomy," *Multidimensional Systems and Signal Processing Journal, Springer,* vol. 22, 2011.

[24] W. Liu and S. Weiss, "Design of frequency-invariant beamformers employing multi-dimensional fourier transforms," in *Proceedings of the Fourth International Workshop on Multidimensional Systems* , Wuppertal, Germany, 2005.

[25] W. Liu, S. Weiss, J. McWhirter and I. Proudler, "Frequency invariant beamforming for two-dimensional and three-dimensional arrays," *Signal Processing,* p. 2535–2543, 2007..

[26] W. Liu and S. Weiss, "Design of frequency invarint beamformers for broadband arrays," *IEEE Transactions on Signal Processing,* p. 855–860, 2008.

[27] T. Chou, "Frequency-independent beamformer with low response error," in *International Conference on Acoustics, Speech, and Signal Processing (ICASSP)*, 1995.

[28] Y. R. Zheng, R. A. Goubran and M. El-Tanany, "A broadband adaptive beamformer using nested arrays and multirate techniques," in *Proc. IEEE DSP Workshop*, 2000.

[29] P. Pal and P. Vaidyanathan, "Beamforming Using Passive Nested Arrays of Sensors," in *IEEE International Symposium on Circuits and Systems (ISCAS)*, New York, 2010.

[30] P. Pal and P. P. Vaidyanathan, "Nested arrays: a novel approach to array processing with enhanced degrees of freedom," *IEEE Transaction on Signal Processing,* p. 4167–4181, 2010.

[31] I. Moazzen and P. Agathoklis, "Broadband Beamforming Using 2D Trapezoidal Filters and Nested Arrays," in *IEEE Pacific Rim Conference on Communications, Computers and Signal Processing*, Victoria, CA, 2011.

[32] I. Moazzen and P. Agathoklis, "Broadband beamfoming using Nested Planar Arrays and 3D FIR frustum filters," in *IEEE International Symposium on Circuits and Systems (ISCAS),* , 2012 .

[33] J. Haan, N. Grbic and I. Claesson, "Design and evaluation of nonuniform dft filter banks in subband microphone arrays," in *Proceedings of the IEEE International Conference on Acoustics, Speech and Signal Processing*, Orlando, FL, USA, 2002.

[34] W. Liu and R. Langley, "Adaptive wideband beamforming with combined spatial/temporal subband decomposition," in *Proceedings of the Progress in Electromagnetics Research Symposium*, Beijing, China, 2007.

[35] S. Weiss and I. Proudler, "Comparing efficient broadband beamforming architectures and their performance trade-offs," in *Proceedings of the International Conference on Digital Signal Processing*, Hellas, Greece, 2002.

[36] W. Liu and R. Langley, "An adaptive wideband beamforming structure with combined subband decomposition," *IEEE Transactions on Antennas and Propagation,* p. 913–920, 2009.

[37] S. Weiss, R. Stewart, M. Schabert, I. Proudler and M. Hoffman, "An efficient scheme for broadband adaptive beamforming," in *Proceedings of the Asilomar Conference on Signals, Systems and Computers*, Monterey, CA, USA, 1999.

[38] W. Liu and S. Weiss, "Frequency invariant beamforming in subbands," in *Proceedings of the Asilomar Conference on Signals, Systems and Computers*, Pacific Grove, CA, USA, 2004.

[39] Y. Zhao, W. Liu and R. Langley, "Design of frequency invariant beamformers in subbands," in *Proceedings of the IEEE Workshop on Statistical Signal Processing*, Cardiff, UK, 2009.

[40] I. Moazzen and P. Agathoklis, "Analysis of a Broadband Beamformer based on Trapezoidal Filters and Nested Arrays," in *IEEE 4th Latin American Symposium on Circuits and Systems*, Peru, 2013.

[41] P. Vaidyanathan, Y. Lin, S. Akkarakaran and S. Phoong, "Discrete multitone modulation with principal component filter banks," *IEEE Transactions on Circuits and Systems I: Fundamental Theory and Applications,* vol. 49, no. 10, pp. 1397- 1412, 2002.

[42] A. Biem, S. Katagiri, E. McDermott and B. Juang, "An application of discriminative feature extraction to filter-bank-based speech recognition," *IEEE Transactions on Speech and Audio Processing,* vol. 9, no. 2, pp. 96-110, 2001.

[43] T. Nguyen and S. Oraintara, "Multiresolution direction filterbanks: theory, design, and applications," *IEEE Transactions on Signal Processing,* vol. 53, no. 10, pp. 3895 - 3905, 2005 .

[44] T. Tran, R. de Queiroz and T. Nguyen, "Linear-phase perfect reconstruction filter bank: lattice structure, design, and application in image coding," *IEEE Transactions on Signal Processing,* vol. 48, no. 1, pp. 133 - 147, 2000.

[45] T. Tran and T. Nguyen, "On M-channel linear phase FIR filter banks and application in image compression," *IEEE Transactions on Signal Processing,* vol. 45, no. 9, pp. 2175 - 2187, 1997.

[46] P. Vaidyanathan, "Multirate digital filters, filter banks, polyphase networks, and applications: a tutorial," in *Proceedings of the IEEE*, 1990.

[47] P. Vaidyanathan, Multirate Systems and Filter Banks, Englewood Cliffs, NJ, USA: Prentice-Hall, 1993.

[48] T. Nguyen, "Near-perfect-reconstruction pseudo-QMF banks," *IEEE Transactions on Signal Processing,* vol. 42, no. 1, pp. 65-76, 1994.

[49] P. Heller, T. Karp and T. Nguyen, "A general formulation of modulated filter banks," *IEEE Transactions on Signal Processing,* vol. 47, no. 4, pp. 986 - 1002 , 1999.

[50] P. Saghizadeh and A. Willson, "A new approach to the design of critically sampled M-channel uniform-band perfect-reconstruction linear-phase FIR filter banks," *IEEE Transactions on Signal Processing,* vol. 46, no. 6, pp. 1544 - 1557, 1998 .

[51] W. Lu, H. Xu and A. Antoniou, "A new method for the design of FIR quadrature mirror-image filter

banks," *IEEE Transactions on Circuits and Systems II: Analog and Digital Signal Processing,* vol. 45, no. 7, pp. 922 - 926, 1998.

[52] R. Bregovic and T. Saramaki, "A general-purpose optimization approach for designing two-channel FIR filterbanks," *IEEE Transactions on Signal Processing,* vol. 51, no. 7, pp. 1783 - 1791, 2003.

[53] C. Goh and Y. Lim, "Novel approach for the design of two channel perfect reconstruction linear phase FIR filter banks," *IEEE Transactions on Circuits and Systems II: Analog and Digital Signal Processing,* vol. 45, no. 8, pp. 1141 - 1146, 1998 .

[54] K. Nayebi, T. I. Barnwell and M. Smith, "Time-domain filter bank analysis: a new design theory," *IEEE Transactions on Signal Processing,* vol. 40, no. 6, pp. 1412-1429, 1992.

[55] P.-Q. Hoang and P. Vaidyanathan, "Non-uniform multirate filter banks: theory and design," in *IEEE International Symposium on Circuits and Systems*, 1989.

[56] J. Li, T. Nguyen and S. Tantaratana, "A simple design method for near-perfect-reconstruction nonuniform filter banks," *IEEE Transactions on Signal Processing,* vol. 45, no. 8, pp. 2105-2109, 1997 .

[57] W. Zhong, G. Shi, X. Xie and X. Chen, "Design of Linear-Phase Nonuniform Filter Banks With Partial Cosine Modulation," *IEEE Transactions on Signal Processing,* vol. 58, no. 6, pp. 3390-3395, 2010.

[58] K. Nayebi, T. I. Barnwell and M. Smith, "Nonuniform filter banks: a reconstruction and design theory," *IEEE Transactions on Signal Processing,* vol. 41, no. 3, pp. 1114-1127, 1993.

[59] C.-F. Ho, B. Ling, Y. Liu, P. Tam and K. Teo, "Optimal design of nonuniform FIR transmultiplexer using semi-infinite programming," *IEEE Transactions on Signal Processing,* vol. 53, no. 7, pp. 2598- 2603, 2005.

[60] C.-F. Ho, B. Ling, Y. Liu, P. Tam and K. Teo, "Efficient Algorithm for Solving Semi-Infinite Programming Problems and Their Applications to Nonuniform Filter Bank Designs," *IEEE Transactions on Signal Processing,* vol. 54, no. 11, pp. 4223-4232, 2006.

[61] K. Nayebi and T. Barnwell, "Reconstruction From Incompatible Nonuniform Band Filter Bank," in *IEEE International Symposium on Circuits and Systems*, 1993.

[62] T. Chen, L. Qiu and E. Bai, "General multirate building structures with application to nonuniform filter banks," *IEEE Transactions on Circuits and Systems II: Analog and Digital Signal Processing,*

vol. 45, no. 8, pp. 948-958, 1998.

[63] C. Ho, B. Ling and P. Tam, "Representations of Linear Dual-Rate System Via Single SISO LTI Filter, Conventional Sampler and Block Sampler," *IEEE Transactions on Circuits and Systems II: Express Briefs,* vol. 55, no. 2, pp. 168-172, 2008.

[64] J. Prokis and M. Salehi, Digital Communications, New York: McGrew-Hill, 2008.

[65] R. Schmidt, "Multiple emitter location and signal parameter estimation," *IEEE Transactions on Antennas and Propagation,* vol. 34, no. 3, pp. 276- 280, 1986.

[66] R. Roy and T. Kailath, "ESPRIT-estimation of signal parameters via rotational invariance techniques," *IEEE Transactions on Acoustics, Speech and Signal Processing,* vol. 37, no. 7, pp. 984-995, 1989.

[67] T. Sarkar and O. Pereira, "Using the matrix pencil method to estimate the parameters of a sum of complex exponentials," *IEEE Antennas and Propagation Magazine,* vol. 37, no. 1, pp. 48-55, 1995.

[68] N. Wang, P. Agathoklis and A. Antoniou, "A new DOA estimation technique based on subarray beamforming," *IEEE Transactions on Signal Processing,* vol. 54, no. 9, pp. 3279-3290, 2006.

[69] Y. Lee and W. Wu, "Adaptive Decision Feedback Space–Time Equalization With Generalized Sidelobe Cancellation," *IEEE Transactions on Vehicular Technology,* vol. 57, no. 5, pp. 2894-2906, 2008.

[70] A. Paulraj and B. C. Ng, "Space-time modems for wireless personal communications," *IEEE Personal Communications,* vol. 5, no. 1, pp. 36-48, 1998.

[71] J. Liang, J. Chen and A. Paulraj, "A two-stage hybrid approach for CCI/ISI reduction with space-time processing," *IEEE Communications Letters,* vol. 1, no. 6, pp. 163-165, 1997.

[72] M. Leou, C. Yeh and H. Li, "A novel hybrid of adaptive array and equalizer for mobile communications," *IEEE Transactions on Vehicular Technology,* vol. 49, no. 1, pp. 1-10, 2000.

[73] K. Hayashi and S. Hara, "A new spatio-temporal equalization method based on estimated channel response," *IEEE Transactions on Vehicular Technology,* vol. 50, no. 5, pp. 1250-1259, 2001.

[74] J. Shynk and R. Gooch, "The constant modulus array for cochannel signal copy and direction finding," *IEEE Transactions on Signal Processing,* vol. 44, no. 3, pp. 652-660, 1996.

[75] J. Shynk, A. Keerthi and A. Mathur, "Steady-state analysis of the multistage constant modulus array," *IEEE Transactions on Signal Processing,* vol. 44, no. 4, pp. 948-962, 1996.

[76] A. Mathur, A. Keerthi and J. Shyok, "A variable step-size CM array algorithm for fast fading channels," *IEEE Transactions on Signal Processing,* vol. 45, no. 4, pp. 1083-1087, 1997.

[77] Y. Chen, T. Le-Ngoc, B. Champagne and C. Xu, "Recursive least squares constant modulus algorithm for blind adaptive array," *IEEE Transactions on Signal Processing,* vol. 52, no. 5, pp. 1452- 1456, 2004.

[78] V. Venkataraman and J. Shynk, "A Multistage Hybrid Constant Modulus Array With Constrained Adaptation for Correlated Sources," *IEEE Transactions on Signal Processing,* vol. 55, no. 6, pp. 2509-2519, 2007.

[79] D. Godard, "Self-Recovering Equalization and Carrier Tracking in Two-Dimensional Data Communication Systems," *IEEE Transactions on Communications,* vol. 28, no. 11, pp. 1867- 1875, 1980.

[80] I. Moazzen and P. Agathoklis, "An Approach for Joint Blind Space-Time Equalization and DOA Estimation," in *IEEE International Symposium on Circuits and Systems* , China, 2013.

[81] J. Labat, O. Macchi and C. Laot, "Adaptive decision feedback equalization: can you skip the training period?," *IEEE Transactions on Communications,* vol. 46, no. 7, pp. 921-930, 1998.

[82] J. Yang, J. Werner and G. Dumont, "The multimodulus blind equalization and its generalized algorithms," *IEEE Journal on Selected Areas in Communications,* vol. 20, no. 5, pp. 997-1015, 2002.

[83] Y. Xiang, N. Gu and K. Wong, "Adaptive blind source separation using constant modulus criterion and signal mutual information," in *IEEE International Conference on Industrial Technology*, 2005.

[84] F. Harris, Multirate Signal Processing for Communication Systems, Prentice Hall, 2004.

[85] S. Stanimirovic, "Single-Dish Radio Astronomy: Techniques and Applications," in *Stanimirovic, S. (Editor); , Single-Dish Radio Astronomy: Techniques and Applications. Proceedings of the Naic-Nrao Summer School Held at National Astronomy and Ionosphere Center, Arecibo Observatory, arecib, Astronomical Society of the Pacific*, 2002.

[86] Y. Wang, J. Ostermann and Y. Zhang, Video processing and communications, Prentice Hall, 2001.

[87] R. Mersereau, "The processing of hexagonally sampled two-dimensional signals," *Proceedings of the IEEE,* vol. 67, no. 6, pp. 930- 949, 1979.

[88] J. Coleman, "Three-phase sample timing on a wideband triangular array of 4/3 the usual density reduces the Nyquist rate for far-field signals by two thirds," in *Conference on Signals, Systems and*

Computers, 2004.

[89] P. J. Davis and P. Rabinowitz, Methods of numerical integration, 2007.

[90] J. Ehrhardt, "Hexagonal fast Fourier transform with rectangular output," *IEEE Transactions on Signal Processing,* vol. 41, no. 3, pp. 1469-1472, 1993.

[91] A. Antoniou, Digital Signal Processing: Signals Systems and Filters, New York, NY: McGraw-Hill, 2005.

[92] A. Antoniou and W. Lu, Practical Optimization: Algorithms and Engineering Applications, Springer, 2010.

[93] M. Mansour, "A design procedure for oversampled nonuniform filter banks with perfect-reconstruction," in *IEEE International Conference on Acoustics, Speech and Signal Processing (ICASSP)*, 2011.

[94] Z. Cvetkovic and M. Vetterli, "Oversampled filter banks," *IEEE Transactions on Signal Processing,* vol. 46, no. 5, pp. 1245-1255, 1998.

[95] J. Kliewer and A. Mertins, "Oversampled cosine-modulated filter banks with arbitrary system delay," *IEEE Transactions on Signal Processing,* vol. 46, no. 4, pp. 941-955, 1998.

[96] Q. Liu, B. Champagne and K. Dominic, "Simple design of oversampled uniform DFT filter banks with applications to subband acoustic echo cancellation," *Signal Processing,* vol. 80, no. 5, pp. 831-847, 2000.

[97] Y. Zheng, R. Goubran and M. El-Tanany, "Experimental evaluation of a nested microphone array with adaptive noise cancellers," *IEEE Transactions on Instrumentation and Measurement,* vol. 53, no. 3, pp. 777- 786, 2004.

[98] V. Venkataraman and J. Shynk, "A Multistage Hybrid Constant Modulus Array With Constrained Adaptation for Correlated Sources," *IEEE Transactions on Signal Processing,* vol. 55, no. 6, pp. 2509-2519, 2007.

[99] M. Absar and S. George, "On the search for compatible numbers in the design of maximally decimated perfect reconstruction non-uniform filter bank," in *IEEE Workshop on Signal Processing Systems*, 2001.

APPENDIX A

The passband area of TF in the 2D frequency domain is defined in Eq.(2.7). Using the inverse Fourier transform, the space-time impulse response of the TF can be obtained as follows.

Table A.1. The closed form of the designed trapezoidal filter

If $n_z = 0, n_t = 0$, then $h(n_z, n_t) = \dfrac{3\alpha^{-1}(\tan(\Phi+\varepsilon) - \tan(\Phi-\varepsilon))}{16}$
If $n_z = 0, n_t \neq 0$, then $h(n_z, n_t) =$ $\dfrac{\alpha^{-1}(\tan(\Phi+\varepsilon) - \tan(\Phi-\varepsilon))}{4\pi^2}[\dfrac{W_2 \sin(W_2 n_t)}{n_t} - \dfrac{W_1 \sin(W_1 n_t)}{n_t} + \dfrac{1}{n_t^2}(\cos(W_2 n_t) - \cos(W_1 n_t))]$
If $n_z \neq 0, \alpha^{-1}\tan(\Phi+\varepsilon)n_z + n_t = 0, \alpha^{-1}\tan(\Phi-\varepsilon)n_z + n_t = 0$, then $h(n_z, n_t) = 0$
If $n_z \neq 0, \alpha^{-1}\tan(\Phi+\varepsilon)n_z + n_t = 0, \alpha^{-1}\tan(\Phi-\varepsilon)n_z + n_t \neq 0$,   then $h(n_z, n_t) = 2b_2(\cos(q_3) - \cos(q_4))$
If $n_z \neq 0, \alpha^{-1}\tan(\Phi+\varepsilon)n_z + n_t \neq 0, \alpha^{-1}\tan(\Phi-\varepsilon)n_z + n_t = 0$, then $h(n_z, n_t) = 2b_1(\cos(q_2) - \cos(q_1))$
otherwise, $h(n_z, n_t) = 2b_1(\cos(q_2) - \cos(q_1)) - 2b_2(\cos(q_4) - \cos(q_3))$
where $q_1 = (\alpha^{-1}\tan(\Phi+\varepsilon)n_z + n_t)W_1, q_2 = (\alpha^{-1}\tan(\Phi+\varepsilon)n_z + n_t)W_2,$ $q_3 = (\alpha^{-1}\tan(\Phi-\varepsilon)n_z + n_t)W_1, q_4 = (\alpha^{-1}\tan(\Phi-\varepsilon)n_z + n_t)W_2$ $b_1 = -\dfrac{1}{4\pi^2 n_z(\alpha^{-1}\tan(\Phi+\varepsilon)n_z + n_t)}, b_2 = -\dfrac{1}{4\pi^2 n_z(\alpha^{-1}\tan(\Phi-\varepsilon)n_z + n_t)}$ $W_1 = \alpha\beta_2\pi \quad and \quad W_2 = \alpha\beta_1\pi$

APPENDIX B

Proof of Lemma 2.1 (Eq. (2.9)):

The continuous signal $f(t+c^{-1}\cos(\theta)z)$ (Eq. (2.4)) is spatially sampled by the ℓ^{th} subarray in which the distance between elements is $2^{\ell-1}d$ (d is distance between elements for the first subarray), and then temporally sampled by T_s. Replacing $\mathbf{F}(f_z, f_{ct})$ into Eq.(2.6), changing d by $2^{\ell-1}d$, and using the properties of delta function, within the Nyquist box, i.e. $|\omega_z, \omega_t| \le \pi$, we get:

$$\mathbf{F}_D^{\ell}(e^{j\omega_z}, e^{j\omega_t}) = \frac{1}{dT_s}\delta\left(\frac{\omega_z}{2\pi d} - 2^{\ell-1}\cos(\theta)\frac{\omega_t}{2\pi cT_s}\right)F\left(\frac{\omega_t}{2\pi T_s}\right) + \mathbf{F}_{aliasing} \quad \text{(B.1)}$$

The last term appears as a result of aliasing. Since the ℓ^{th} subarray is processing the ℓ^{th} octave, $f_u/2^{\ell} < |f_t| < f_u/2^{\ell-1}$ (i.e. $\alpha\pi/2^{\ell} < |\omega_t| < \alpha\pi/2^{\ell-1}$), $H_{\ell}(z)$ an FIR filter which has the gain of unity within $\alpha\pi/2^{\ell} < |\omega_t| < \alpha\pi/2^{\ell-1}$ and its constant group delay is N_H, is deployed at each sensor of the ℓ^{th} subband to extract the ℓ^{th} octave. Since the second term of the right-hand side of Eq. (B.1) is non-zero outside this range, it would disappear after filtering. The spectrum becomes:

$$\hat{\mathbf{F}}_D^{\ell}(e^{j\omega_z}, e^{j\omega_t}) =$$
$$\frac{1}{dT_s}\delta\left(\frac{\omega_z}{2\pi d} - 2^{\ell-1}\cos(\theta)\frac{\omega_t}{2\pi cT_s}\right)F\left(\frac{\omega_t}{2\pi T_s}\right)e^{-\omega_t N_H}\prod(2^{\ell-1}\omega_t) \tag{B.2}$$

where $\prod(2^{\ell-1}\omega_t)$ is 1 within $\alpha\pi/2^{\ell} \le |\omega_t| \le \alpha\pi/(2^{\ell-1})$, and zero elsewhere. Then, the filtered signal is temporally downsampled by $2^{\ell-1}$ leading directly to Eq. (2.9).

APPENDIX C

Proof of Lemma 2.2:

The TF has passband area which encloses the ROS of $\overline{\mathbf{F}}_D^{\ell}$, Eq.(2.9), as close as possible. According to [20], within the passband area the frequency response of TF can be approximated by:

$$\mathbf{H}_{TF}(e^{j\omega_z}, e^{j\omega_t}) \approx 1 e^{-j\omega_t N_{TF}} \tag{C.1}$$

and zero outside the passband area (N_{TF} is the group delay of TF). The output of the TF is:

$$\breve{\mathbf{f}}_D^{\ell}(n_z, n_t) = \frac{1}{(2\pi)^2} \iint_{\omega_t, \omega_z} \overline{\mathbf{F}}_D^{\ell}(e^{j\omega_z}, e^{j\omega_t}) \mathbf{H}_{TF}(e^{j\omega_z}, e^{j\omega_t}) e^{j(\omega_z n_z + \omega_t n_t)} d\omega_z d\omega_t \tag{C.2}$$

Then, the center sensor is chosen as the output (n_z =0) [20]. By replacing Eq.(2.9) and (C.1) into Eq.(C.2) we obtain:

$$\begin{aligned} \breve{f}_D^{\ell}(0, n_t) = & \\ & \frac{1}{2\pi} \int_{\omega_t = -\alpha\pi}^{-\frac{\alpha\pi}{2}} \zeta(\omega_t) \frac{1}{2^{\ell-1} T_s} F\left(\frac{\omega_t}{2\pi T_s 2^{\ell-1}}\right) e^{j\omega_t (n_t - \frac{1}{2^{\ell-1}} N_H - N_{TF})} d\omega_t \\ & + \frac{1}{2\pi} \int_{\omega_t = \frac{\alpha\pi}{2}}^{\alpha\pi} \zeta(\omega_t) \frac{1}{2^{\ell-1} T_s} F\left(\frac{\omega_t}{2\pi T_s 2^{\ell-1}}\right) e^{j\omega_t (n_t - \frac{1}{2^{\ell-1}} N_H - N_{TF})} d\omega_t \end{aligned} \tag{C.3}$$

where

$$\zeta(\omega_t) = \int_{\omega_z=-\pi}^{\pi} \delta(\frac{\omega_z}{2\pi d} - \cos(\theta)\frac{\omega_t}{2\pi c T_s}) d(\frac{\omega_z}{2\pi d}) \tag{C.4}$$

Clearly $\zeta(\omega_t)$=1. It can be inferred that the 1DFT of $\breve{f}_D^{\ell}$ is:

$$\breve{f}_D^{\ell}(t) \overset{FT}{\Leftrightarrow} \frac{1}{2^{\ell-1}T_s} F(\frac{\omega_t}{2\pi T_s 2^{\ell-1}}) e^{-j\omega_t(\frac{1}{2^{\ell-1}}N_H + N_{TF})} \prod(\omega_t) \tag{C.5}$$

Next, the signal is upsampled by the rate of $2^{\ell-1}$:

$$\widetilde{f}_D^{\ell}(t) \overset{FT}{\Leftrightarrow} \frac{1}{2^{\ell-1}T_s} F(\frac{\omega_t}{2\pi T_s}) e^{-j\omega_t(N_H + 2^{\ell-1}N_{TF})} \prod(2^{\ell-1}\omega_t) \tag{C.6}$$

After upsampling, a synthesis filter $G_\ell(z)$ is required to remove all replicas of the signal spectrum except for the baseband copy. $G_\ell(z)$ is an FIR filter, with a constant group delay of N_G and the similar frequency specifications to $H_\ell(z)$ (just the amplitude is $2^{\ell-1}$ times greater to compensate the attenuation by $2^{\ell-1}$ due to downsampling). After filtering, we get:

$$\widetilde{y}_\ell(t) \overset{FT}{\Leftrightarrow} \frac{1}{T_s} F(\frac{\omega_t}{2\pi T_s}) e^{-j\omega_t(N_H + N_G + 2^{\ell-1}N_{TF})} \prod(2^{\ell-1}\omega_t) \tag{C.7}$$

$$\widetilde{y}_{\ell}(n_t) = \frac{1}{2\pi}\left[\int_{\omega_t=-\frac{\alpha\pi}{2^{\ell-1}}}^{-\frac{\alpha\pi}{2^{\ell}}} \frac{1}{T_s} F\left(\frac{\omega_t}{2\pi T_s}\right) e^{j\omega_t[n_t-(N_H+N_G+2^{\ell-1}N_{TF})]} d\omega_t + \int_{\omega_t=\frac{\alpha\pi}{2^{\ell}}}^{\frac{\alpha\pi}{2^{\ell-1}}} \frac{1}{T_s} F\left(\frac{\omega_t}{2\pi T_s}\right) e^{j\omega_t[n_t-(N_H+N_G+2^{\ell-1}N_{TF})]} d\omega_t\right] \quad \text{(C.8)}$$

By replacing $f_t = \omega_t / 2\pi T_s$ in Eq.(C.8), it can be concluded that $\widetilde{y}_{\ell}(n_t)$ is a shifted version of the PW received at the origin, i.e. $f(t)$, which just includes the information within the ℓ^{th} octave. The shift value is equal to $2^{\ell-1}N_{TF} + N_H + N_G$.

APPENDIX D

Proof of Lemma 3.1 (Eq.(3.6)):

Eqs.(3.3) and (3.4) can be expressed in a matrix form:

$$\mathbf{A}(z)\mathbf{B}(z) = \mathbf{c}(z) \tag{D.1}$$

where:

$$\mathbf{A}(z) = \begin{bmatrix} \beta_{1,0}H_1(z) & \beta_{2,0}H_2(z) & \cdots & \beta_{K,0}H_K(z) \\ \beta_{1,1}H_1(ze^{-j\frac{2\pi}{M}}) & \beta_{2,1}H_2(ze^{-j\frac{2\pi}{M}}) & \cdots & \beta_{K,1}H_K(ze^{-j\frac{2\pi}{M}}) \\ \beta_{1,2}H_1(ze^{-j\frac{2\pi}{M}(2)}) & \beta_{2,2}H_2(ze^{-j\frac{2\pi}{M}(2)}) & \cdots & \beta_{K,2}H_K(ze^{-j\frac{2\pi}{M}(2)}) \\ \vdots & \vdots & \ddots & \vdots \\ \beta_{1,M-1}H_1(ze^{-j\frac{2\pi}{M}(M-1)}) & \beta_{2,M-1}H_2(ze^{-j\frac{2\pi}{M}(M-1)}) & \cdots & \beta_{K,M-1}H_K(ze^{-j\frac{2\pi}{M}(M-1)}) \end{bmatrix} \tag{D.2}$$

$$\mathbf{B}(z) = \begin{bmatrix} F_1(z) \\ F_2(z) \\ F_3(z) \\ \vdots \\ F_K(z) \end{bmatrix}, \quad \mathbf{c}(z) = \begin{bmatrix} z^{-\Delta} \\ 0 \\ 0 \\ 0 \\ 0 \end{bmatrix}$$

The $\widetilde{\mathbf{Z}}$ operator will be defined as:

$$\widetilde{\mathbf{Z}}_{M\times MN}=\begin{bmatrix}\mathbf{p} & \mathbf{0}^T & \mathbf{0}^T & \cdots & \mathbf{0}^T\\ \mathbf{0}^T & \mathbf{p} & \mathbf{0}^T & \cdots & \mathbf{0}^T\\ \mathbf{0}^T & \mathbf{0}^T & \mathbf{p} & \cdots & \mathbf{0}^T\\ \cdots & \cdots & \cdots & \ddots & \mathbf{0}^T\\ \mathbf{0}^T & \mathbf{0}^T & \mathbf{0}^T & \cdots & \mathbf{p}\end{bmatrix} \tag{D.3}$$

where $\mathbf{p}_{1\times N}=[1, z^{-1},..., z^{-(N-1)}]$ and $\mathbf{0}_{N\times 1}=[0 \quad 0 \quad \cdots \quad 0]^T$. Using $\widetilde{\mathbf{Z}}$ operator, Eq.(D.1) can be written as follows ($\mathbf{0}$ is $\mathbf{0}_{N\times 1}$, unless otherwise stated):

$$\widetilde{\mathbf{Z}}(\mathbf{HF})\widetilde{\mathbf{Z}}^T\mathbf{e}=\widetilde{\mathbf{Z}}(\mathbf{U})\widetilde{\mathbf{Z}}^T\mathbf{e} \tag{D.4}$$

where $\mathbf{e}_{M\times 1}=[1 \quad 1 \quad \cdots \quad 1]^T$ and:

$$\mathbf{H}_{MN\times K}=\begin{bmatrix}\beta_{1,0}\mathbf{h}_1 & \beta_{2,0}\mathbf{h}_2 & \cdots & \beta_{K,0}\mathbf{h}_K\\ \beta_{1,1}\mathbf{h}_1\otimes\mathbf{\Lambda}_1 & \beta_{2,1}\mathbf{h}_2\otimes\mathbf{\Lambda}_1 & \cdots & \beta_{K,1}\mathbf{h}_K\otimes\mathbf{\Lambda}_1\\ \beta_{1,2}\mathbf{h}_1\otimes\mathbf{\Lambda}_2 & \beta_{2,2}\mathbf{h}_2\otimes\mathbf{\Lambda}_2 & \cdots & \beta_{K,2}\mathbf{h}_K\otimes\mathbf{\Lambda}_2\\ \vdots & \vdots & \ddots & \vdots\\ \beta_{1,M-1}\mathbf{h}_1\otimes\mathbf{\Lambda}_{M-1} & \beta_{2,M-1}\mathbf{h}_2\otimes\mathbf{\Lambda}_{M-1} & \cdots & \beta_{K,M-1}\mathbf{h}_K\otimes\mathbf{\Lambda}_{M-1}\end{bmatrix} \tag{D.5}$$

$$\mathbf{F}_{K\times MN}=\begin{bmatrix}\mathbf{f}_1^T & \mathbf{0}^T & \mathbf{0}^T & \cdots & \mathbf{0}^T\\ \mathbf{0}^T & \mathbf{f}_2^T & \mathbf{0}^T & \cdots & \mathbf{0}^T\\ \mathbf{0}^T & \mathbf{0}^T & \mathbf{f}_3^T & \cdots & \mathbf{0}^T\\ \vdots & \vdots & \vdots & \ddots & \mathbf{0}^T\\ \mathbf{0}^T & \mathbf{0}^T & \mathbf{0}^T & \cdots & \mathbf{f}_K^T\end{bmatrix}$$

$\mathbf{U}$ is a $MN \times MN$ matrix whose elements are all zero except the one located on the first column and $\Delta+1^{th}$ row which is equal to 1. From Eq. (D.4):

$$\widetilde{\mathbf{Z}}(\mathbf{HF}-\mathbf{U})\widetilde{\mathbf{Z}}^T\mathbf{e}=\mathbf{0}_{M\times 1} \tag{D.6}$$

Then, we can get:

$$\begin{aligned}&\widetilde{\mathbf{Z}}\mathbf{G}\,\mathbf{z}^T=\mathbf{0}_{M\times 1}\\ &\text{where}\\ &\mathbf{z}_{1\times MN}=\mathbf{e}^T\widetilde{\mathbf{Z}}=[\mathbf{p},\mathbf{p},...,\mathbf{p}] \quad \text{and}\\ &\mathbf{G}_{MN\times MN}=\mathbf{HF}-\mathbf{U}\end{aligned} \tag{D.7}$$

Because of the structure of $\mathbf{z}$ and $\widetilde{\mathbf{Z}}$, Eq.(D.7) can be simplified more. In order to do that, matrix $\mathbf{G}$ needs be split into $1\times N$ vectors as follows:

$$\mathbf{G}=\begin{bmatrix}\mathbf{g}_1^{(1)} & \mathbf{g}_2^{(1)} & \cdots & \mathbf{g}_M^{(1)}\\ \mathbf{g}_1^{(2)} & \mathbf{g}_2^{(2)} & \cdots & \mathbf{g}_M^{(2)}\\ \vdots & \vdots & \ddots & \vdots\\ \mathbf{g}_1^{(MN)} & \mathbf{g}_2^{(MN)} & \cdots & \mathbf{g}_M^{(MN)}\end{bmatrix} \tag{D.8}$$

$[\mathbf{g}_j^{(i)}]_{1\times N}$ corresponds to the elements of matrix $\mathbf{G}$ located on the i^{th} row ($i=1,2,...,MN$) and $(j-1)N+1^{th}$ to jN^{th} columns ($j=1,2,...,M$). Eq.(D.7) can be replaced by:

$$\widetilde{\mathbf{Z}}\hat{\mathbf{G}}\mathbf{p}^T=0 \tag{D.9}$$

where:

$$\hat{\mathbf{G}}_{MN\times N}=\begin{bmatrix}\hat{\mathbf{g}}^{(1)}\\ \hat{\mathbf{g}}^{(2)}\\ \vdots\\ \hat{\mathbf{g}}^{(MN)}\end{bmatrix} \tag{D.10}$$

$$\hat{\mathbf{g}}^{(i)}=\mathbf{g}_1^{(i)}+\mathbf{g}_2^{(i)}+\cdots+\mathbf{g}_M^{(i)} \quad \text{for} \quad i=1,2,..,MN$$

Then, $\hat{\mathbf{G}}$ can be split into $N\times N$ sub-matrixes:

$$\hat{\mathbf{G}}_{MN\times N}=\begin{bmatrix}\boldsymbol{\psi}_1\\ \boldsymbol{\psi}_2\\ \vdots\\ \boldsymbol{\psi}_M\end{bmatrix} \tag{D.11}$$

where

$$[\boldsymbol{\psi}_i]_{N\times N}=\begin{bmatrix}\hat{\mathbf{g}}^{((i-1)N+1)}\\ \hat{\mathbf{g}}^{((i-1)N+2)}\\ \vdots\\ \hat{\mathbf{g}}^{(iN)}\end{bmatrix} \quad \text{for} \quad i=1,2,...,M$$

It can be shown that Eq.(D.9) means that the summation of all elements in every single off-diagonal of $\boldsymbol{\psi}_i$ ($i=1,2,...,M$), shown as follows, is equal to zero.

$$\boldsymbol{\psi}_i = \begin{bmatrix} \psi_{1,1} & \psi_{1,2} & \psi_{1,3} & \cdots & \psi_{1,N} \\ \psi_{2,1} & \psi_{2,2} & \psi_{2,3} & \cdots & \psi_{2,N} \\ \psi_{3,1} & \psi_{3,2} & \psi_{3,3} & \cdots & \psi_{3,N} \\ \vdots & \vdots & \vdots & \ddots & \vdots \\ \psi_{N,1} & \psi_{N,2} & \psi_{N,3} & \cdots & \psi_{N,N} \end{bmatrix} \tag{D.12}$$

Finally, Eq. (D.12) can be easily formulated as a set of linear equations as shown in Eq.(3.6).

APPENDIX E

Proof of Lemma 3.2 (Eq.(3.11)):

Using Euler equation, the magnitude response of the k^{th} analysis filter can be written as:

$$\left|H_k(e^{j\omega})\right| = \sqrt{\left(\sum_{i=0}^{N-1} h_{k,i}\cos(i\omega)\right)^2 + \left(\sum_{i=0}^{N-1} h_{k,i}\sin(i\omega)\right)^2} \tag{E.1}$$

Then Eq. (E.1) can be formulated as:

$$\left|H_k(e^{j\omega})\right| = \sqrt{\mathbf{h}_k^H \boldsymbol{\zeta}_{\cos}(\omega)\boldsymbol{\zeta}_{\cos}^H(\omega)\mathbf{h}_k + \mathbf{h}_k^H \boldsymbol{\zeta}_{\sin}(\omega)\boldsymbol{\zeta}_{\sin}^H(\omega)\mathbf{h}_k} \tag{E.2}$$

where:

$$\boldsymbol{\zeta}_{\cos}(\omega) = \begin{bmatrix} 1 & \cos\omega & \cos 2\omega & \dots & \cos(N-1)\omega \end{bmatrix}^T$$

$$\boldsymbol{\zeta}_{\sin}(\omega) = \begin{bmatrix} 1 & \sin\omega & \sin 2\omega & \dots & \sin(N-1)\omega \end{bmatrix}^T$$

Considering $\mathfrak{R}_{\cos}(\omega) = \boldsymbol{\zeta}_{\cos}(\omega)\boldsymbol{\zeta}_{\cos}^H(\omega)$ and $\mathfrak{R}_{\sin}(\omega) = \boldsymbol{\zeta}_{\sin}(\omega)\boldsymbol{\zeta}_{\sin}^H(\omega)$, we get:

$$\left|H_k(e^{j\omega})\right| = \sqrt{\mathbf{h}_k^H \mathfrak{R}_{\cos}(\omega)\mathbf{h}_k + \mathbf{h}_k^H \mathfrak{R}_{\sin}(\omega)\mathbf{h}_k} \tag{E.3}$$

Finally, by introducing $\mathfrak{R}(\omega) = \mathfrak{R}_{\cos}(\omega) + \mathfrak{R}_{\sin}(\omega)$, and this property $\cos(a+b) = \cos(a)\cos(b) - \sin(a)\sin(b)$, Eq.(3.11) can be obtained.

APPENDIX F

RELATED PUBLICATIONS

Journal:

- **Moazzen, I.,** Agathoklis, P.**, "**A Multi-Stage Space-Time Equalizer for Blind Source Separation", *IEEE Transactions on Vehicular Technology*, 2013 (submitted).
- **Moazzen, I.,** Agathoklis, P.**, "**Efficient Implantation of Broadband Beamformers Using Nested Hexagonal Arrays and Frustum Filters**",** *IEEE Transactions on Signal Processing*, 2012 (first revision).
- **Moazzen, I.,** Agathoklis, P., "A General Approach for Filter Bank Design Using Optimization", *IET Journal on Signal Processing*, 2012 (first revision).

Conference:

- **Moazzen, I.,** Agathoklis, P.**,** "An Approach for Joint Blind Space-Time Equalization and DOA Estimation" *IEEE International Symposium on Circuits and Systems (ISCAS)*, China, 2013.
- **Moazzen, I.**, Agathoklis, P., "Analysis of a Broadband Beamformer based on Trapezoidal Filters and Nested Arrays", *4th IEEE Latin American Symposium on Circuits and Systems*, Peru, 2013.
- **Moazzen, I.,** Agathoklis, P., "Broadband Beamforming Using Nested Planar Arrays and FIR Frustum Filters", *IEEE International Symposium on Circuits and Systems (ISCAS)*, South Korea, 2012.
- **Moazzen, I.**, Agathoklis, P., "Broadband Beamforming Using 2D Trapezoidal Filters and Nested Arrays", *2011 IEEE Pacific Rim Conference on Communications, Computers and Signal Processing*, Victoria, Canada, August 24-27.

MATLAB TOOLBOXES (*Submitted on Mathwork website and available for free*)

- **Dig_Filter Toolbox**[1] which can design all types of one-dimensional digital filters using closed-form methods or optimization techniques, developed by Moazzen, I., Agathoklis, P., Antoniou, A., 2010.
- **PR_Nguyen Toolbox**[2] which can design a uniform filter bank using Nguyen perfect reconstruction technique, developed by Moazzen, I., 2012.
- **Filter_Design_2D_McClellan Toolbox**[3] which can design two-dimensional digital filters using McClellan transformation, developed by Moazzen, I., 2012.
- **Filter_Bank_Design Toolbox**[4] which can design all uniform and non-uniform filter banks using optimization techniques, developed by Moazzen, I. and Agathoklis, P., 2013.

[1] - *http://www.mathworks.com/matlabcentral/fileexchange/30321*
[2] - *http://www.mathworks.com/matlabcentral/fileexchange/35053*
[3] - *http://www.mathworks.com/matlabcentral/fileexchange/35051*
[4] - *http://www.mathworks.com/matlabcentral/fileexchange/40128*